A study of the formation of surfactant templated mesoporous silica and titania thin films at the air-liquid interface

Fernandez Martin, Cristina

Award date:
2006

Awarding institution:
University of Bath

A Study of the Formation of Surfactant Templated Mesoporous Silica and Titania Thin Films at the Air-Liquid Interface.

A thesis submitted to the University of Bath for the degree of Doctor of Philosophy in March 2006

by

Cristina Fernández Martín

Physical group. Department of Chemistry.
University of Bath

UNIVERSITY OF BATH

ProQuest LLC
789 East Eisenhower Parkway
P.O. Box 1346
Ann Arbor, MI 48106-1346

Declaration

I hereby declare that the work presented in this thesis was done by the candidate, and all references to ideas and work of other researchers have been specifically acknowledged. I hereby certify that the work embodied in this thesis has not been submitted in any form for another degree or diploma at any other university.

Signature: Cristina F.

Cristina Fernández Martín

Date: 22/03/06

"La ciencia, a pesar de sus progresos increíbles, no puede ni podrá nunca explicarlo todo. Cada vez ganará nuevas zonas a lo que hoy parece inexplicable. Pero las rayas fronterizas del saber, por muy lejos que se eleven, tendrán siempre delante un infinito mundo misterioso."

Gregorio Marañón.

(Science, in spite of its incredible progress, neither can nor ever will be able to explain everything. Every time it will find new areas that today seem inexplicable. But the boundaries of knowledge, though they get farther away, will always present an infinitely mysterious world.)

Gregorio Marañón,

Spanish doctor and writer.

Acknowledgements

I would like to thank my supervisor, Dr. Karen J. Edler, for her consistent support and advice. Thank you for your willing support to improve my knowledge and writing.

I express my gratitude to the University of Bath for financial support as well as to the European Synchrotron Radiation Facility (ESRF) and ISIS facilities (at CLRC's Rutherford Appleton Laboratory) for providing funds to enhance and enrich my work.

Also I would like to tank Dr. Steve J Roser for his pleasant company and enthusiasm, both during the synchrotron experiments and at the everyday workplace. Thanks are also extended to my colleague and friend, Dr. Benjamin O'Driscoll who provide help whenever requested and who made those days on the synchrotron more pleasant.

A very special thanks to Margarida Vareiro for not only being my flatmate but also my best friend during these three years. Also to David Van Mele for his help, care and friendship.

Grateful acknowledgment is extended to Prof. Javier Garcia Guinea for his encouragement and support for improving my professional life doing a PhD in UK. Thank you for giving me the opportunity of taking part in some of your works.

I am grateful to all my friends from Bath for their continued moral support and friendship over the last three years and for all those great lunches, dinners, and parties. These include (being almost impossible to mention all of them): Margarida, Dave, Kam, Ben, Jorge, Luisa, Lorena, Eduardo, Narad, Killian, Rocco, Amilcar, Ramon...

Also a very special thanks to my friends Jose, Gemma, Susana, Kike, Carola, Ignacio, Maria, Tanja and Torsten who gave me the spirit, advice, encouragement and support, both past and present, demonstrating that the distance and time are not barriers for friendship.

The most important acknowledgement I can make at this time is to my family, Martin, Marta y Raquel to whom I honoured-dedicate this thesis. Without your love and support I would have never had enough motivation, courage and strength to pursue my career in science.

Last but not least, to Jacques Barik who has made me happy since the first time I met him and who has given me strength, motivation and love necessary to complete this work and to see a promising shared future.

Agradecimientos

Quisiera agradecer a mi directora de tesis, Dr. Karen J. Edler, por su incondicional ayuda a mejorar mis conocimientos y escritura durante mi PhD. También quisiera agradecer al Dr. Steve J. Roser por su compañía transmitiendo gran entusiasmo, durante los experimentos del sincrotrón así como en el lugar de trabajo diario.

Expreso mi gratitud a The University of Bath por la ayuda financiera y también al European Synchrotron Radiation Facility (ESRF) y a ISIS facilities (en el CLRC's Rutherford Appleton Laboratory) por proporcionar fondos para mejorar y enriquecer mi trabajo.

De manera especial agradezco a mi colega y amigo, el Dr. Benjamin O'Driscoll quien me ha proporcionado ayuda siempre cuando ha sido necesaria y quien ha hecho más agradables esos días en el sincrotrón. También a Margarida Vareiro por haber sido, no solo mi compañera de piso sino también una gran amiga durante estos duros años lejos de nuestros países y familias. Quisiera sumar este especial agradecimiento a David Van Mele por su gran apoyo y amistad.

Mi mas sincero agradecimiento para el Profesor de Investigación del CSIC Javier García Guinea, quien me ha dado estimulo y apoyo para lograr doctorarme en Reino Unido. Gracias por darme la oportunidad de participar en algunos de tus trabajos.

Gracias muy especiales a todos mis amigos de Bath por su continua ayuda moral y amistad durante estos tres años y por esas fantásticas noches de cenas y fiestas. Entre ellos se encuentran: Margarida, Dave, Kam, Ben, Jorge, Luisa, Lorena, Eduardo, Sonia, Laura, Paqui, Walter, Narad, Killian, Rocco, Amilcar, Ramon....

Y por supuesto gracias de todo corazón a mis fieles amigos Jose, Gemma, Susana, Kike, Carola, Ignacio, Maria, Tanja y Torsten que me han dado buenos consejos, estímulo y ayuda, tanto en el pasado como en este presente, demostrando que la distancia y el tiempo no son barreras para la amistad.

El reconocimiento más importante que puedo hacer en estas alturas es a mi familia, Martín, Marta y Raquel a quien dedico con gran orgullo mi tesis. Sin su amor, ayuda y comprensión nunca habría tenido bastante motivación, valor y fuerza para lograr este, mi sueño.

En último lugar, pero no por ello menos importante a Jacques Barik quien me ha hecho feliz desde que le conocí, en marzo del 2005 y quien me ha dado fuerza, motivación y amor necesario para terminar este trabajo y para ver un futuro prometedor a su lado.

Abstract

This thesis covers the study of the formation of surfactant templated mesoporous silica and titania thin films growing at the air-water interface based on their synthesis and characterization.

Surfactant-templated mesoporous thin films are considered of great interest due to their applications as molecular sieve membranes, catalysis supports, in biomedicine, and in optoelectronic devices. The understanding of formation mechanisms in self-assembling systems is a wide field still under development.

A variety of surfactants acting as the structure-directing agents, such as cationic, anionic or non-ionic, have been used in the synthesis of mesoporous silica and titania thin films. They are able to self-assemble in acidic aqueous media into aggregates with different micellar shapes such as spherical, elliptical or cylindrical according to a great number of different parameters. The inorganic sources, being in this case tetramethyloxysilane (TMOS) as silica precursor and titanium (IV) tetrabutoxide ($Ti(OBu^n)_4$) as titania precursor, polymerize around the micellar assembly to form an inorganic mesoporous inorganic network.

X-ray reflectivity, grazing incident X-ray diffraction (GIXD) and Brewster angle microscopy (BAM) are used as surface characterisation techniques. They enable *in situ* time-resolved measurements of the thin film mesostructure development and the consequent formation mechanism as well as characterization of the final film structure at the air-liquid interface. On the other hand, the *in situ* evolution of the micelles in the bulk solution is studied by small angle neutron scattering (SANS), which contains all the information about the shape, size and interactions of the scattering bodies in the sample solution.

Publications

- C. Fernandez-Martin, K. J. Edler, S. J. Roser, Humidity and Temperature effects on CTAB-templated mesophase silicate films at the air-liquid interface. *Langmuir*, Vol 20, pp. 10679-10684, 2004.

- C. Fernandez-Martin, K. J. Edler, S. J. Roser, Evolution of non-ionic surfactant templated silicate films at the air-liquid interface. (*in preparation*)

- K. J. Edler, T. Brennan, C. Fernandez-Martin, S. J. Roser, Formation of mesophase surfactant-templated silica thin films from acidic solutions. *Studies in Surface Science and Catalysis*, Vol 154, pp. 373-379, 2004.

- S. A. Holt, K. J. Edler, C. Fernandez-Martin, Formation of surfactant-silica mesophase films at a silica interface. *Progress in Colloid & Polymer Science*, Vol 128, pp. 169-174, 2004.

- B. M. D. O'Driscoll, E. Milsom, C. Fernandez-Martin, L. White, S. J. Roser and K. J. Edler*, Thin Films of Polyethylenimines and Alkyltrimethylammonium Bromides. *Macromolecules*, Vol 38, pp. 8785-8794, 2005.

- B. M. D. O'Driscoll, C. Fernandez-Martin, Roland D. Wilson, S. J. Roser and K. J. Edler*, The Effect of Micellar Composition on the Formation of Surfactant-Templated Polymer Films. *Journal of Physical Chemistry B*, Vol 110, pp. 5330-5336, 2005.

Abbreviations

$(EO)_x(PO)_y(EO)_x$: Poly(oxyethylene)-poly(oxypropylene)-poly(oxyethylene).

26-TNS: 2-*p*-toluidinyl napthalene-6-sulphonate (a hydrophobic dye).

APS: Advance Photon Source (Illinois, USA).

BAM: Brewster angle microscopy.

Brij 56®: Polyoxyethylene 10 cetyl ether.

Brij 76®: Polyoxyethylene 10 stearyl ether.

C-153: coumarin-153 (a fluorescent probe).

$C_{16}EO_8$: Octaethylene glycol monohexadecyl ether.

CMC: Critical micelle concentration.

CTAB: Cetyl trimethylammonium bromide.

CTACl: Cetyl trimethylammonium chloride.

CVD: Chemical Vapour Deposition.

E.I.S.A.: Evaporation-Induced Self-Assembly.

EO: Oxyethylene chain.

ESRF: European Synchrotron Radiation Facility (Grenoble, France).

FSM-16: 2D hexagonal phase mesoporous materials.

FWHM: Full width half-maximum.

GISAXS: Grazing incident small angle X-ray scattering.

GIXD: Grazing incident X-ray diffraction.

HFR: High-Flux Reactor.

HS: Hard sphere.

ID: Insertion device.

ILL: Institute Max von Laue - Paul Langevin (Grenoble, France).

ISIS: Spallation neutron source (Oxford, UK).

LA: Laurylamine.

LCT: Liquid crystal templating.

M41S: Family of periodic mesoporous silicates from alkaline synthesis.

- **MCM**: Mobil Catalytic Material.
- **MCM-41**: Hexagonal phase (*p6mm*).
- **MCM-48**: Cubic phase (*Ia3d*).
- **MCM-50**: Lamellar phase.

MeOH: Methanol.

MSA: Hayter Penfold mean spherical approximation.

MSU-X: (Michigan State University) A mesoporous silica materials family.

PEI: Polyethylene imine.

Pluronic F127®: $(EO)_{106}(PO)_{70}(EO)_{106}$.

Pluronic P123®: $(EO)_{20}(PO)_{70}(EO)_{20}$.

PS-b-PMMA: Polystyrene-b-poly(methyl methacrylate).

PVD: Physical Vapour Deposition.

RH: Relative humidity.

SALS or **LS**: Light scattering.

SANS: Small angle neutron scattering.

SAXS: Small angle X-ray scattering.

SBA: (Santa Barbara Amorphous) A mesoporous silica materials family.

- **SBA-1**: Cubic phase (*Pm3n*).
- **SBA-11**: Cubic phase ($Pm\bar{3}m$).
- **SBA-12**: 3D hexagonal phase ($P6_3/mmc$).
- **SBA-15**: 2D hexagonal phase (*p6mm*).
- **SBA-16**: Centred-cubic phase ($Im\bar{3}m$).
- **SBA-2**: 3D hexagonal phase ($P6_3/mmc$).
- **SBA-3**: Hexagonal phase (*p6m*).

SDS: Sodium dodecyl sulphate.

SEM: Scanning electro microscopy.

TBOT or **TBT** or **Ti(OBu)$_4$**: Titanium tetrabutoxide.

TEA: Triethanolamine.

TEM: Transmission electro microscopy.

TEOS: Tetraetholxysilane.

Ti-TMS1: Mesoporous titania materials with hexagonal structure.

TM: transition metal.

TMOS: Tetramethoxysilane.

TS-1 and **TS-2**: titanium-silicate 1 and 2 zeolites.

UTD-1: Zeotype (University of Texas at Dallas, number 1).

XRD: X-ray diffraction.

Table of Contents

Chapter 1 Introduction

1.1 Ordered Porous Materials

The synthesis of porous materials is an important academic and industrial issue due to their wide potential applications in catalysis and separation.[1]

Porous materials are classified according to the pore size, by IUPAC convention, as:

- Microporous: pore size < 2 nm
- Mesoporous: 2 nm < pore size < 50nm
- Macroporous: pore size > 50nm

1.1.1 Zeolites

Zeolites are crystalline aluminosilicate and silicate microporous materials with features that make them suitable as catalysts for oil refining, petrochemistry, and organic synthesis. These features are based on their pore size uniformity, high surface area, absorption capacity, and the ability to tailor the chemistry of the zeolites channels to suit the application.[2] Microporous zeotypes, zeolites-like molecular sieves that fulfil the above-mentioned requirements, reach the widest channel aperture with a more than 12 tetrahedral atom ring.[1, 2] The zeotype UTD-1 (University of Texas at Dallas, number 1), the first extra-large pore with 14-membered ring and 7.5 × 10 Å pore dimension, was discovered by Freyhardt *et al.*[3] However these materials have a restricted pore size range, which limit their use with larger organic molecules. Ordered mesoporous materials have therefore been developed to provide larger pore sizes than can be obtained in zeolites.

Apart from silicate and aluminosilicate zeolites, transition metal-substituted zeolite materials have also been reported, in particular and more concerned with this research, titanium-substitutions. The incorporation of titanium into the framework of high-silica zeolites has expanded the application of these materials. The first Ti-containing zeolites were the titanium-silicate 1 and 2 (TS-1[4, 5] and TS-2[6]) used as a catalyst for a selective oxidation of organic compounds by H_2O_2.[7] However due to their limitation in pore size, larger-pore-sized Ti-β-zeolites[5, 8, 9] were synthesized with a 12 Si tetrahedral cavity in contrast with 10 Si tetrahedral cavity of TS-1. Ti-β-zeolites have

been used as catalyst in epoxidation reactions[10] or as photocatalysts for selective oxidations.[11]

1.1.2 Amorphous Porous Materials (Gels)

Porous gels, with silica gels being the ones most studied by the gel research community, are prepared via the sol-gel process from metal alkoxide precursors. Sol-gel processing controls the pore size (covering the range 2-50 nm), thickness and shape obtaining different type of materials such as monoliths, powders, fibers and films. The final material phase depends upon the structures that exist at the gel point which can collapse or cause distortion during the final stages of drying. In the sol-gel process the molecular or colloidal silicate species are dispersed in a solvent and then condense forming a gel. Due to subsequent reactions such as polymerisation, gelation, aging, and drying, structures of polymers, gels, and dried gels (either aerogels or xerogels) may be obtained (see Figure 1.1). Aerogels are prepared by supercritical drying of wet gels and are characterized by having a very low density (~ 0.003 g cm^{-3}), and high porosity (98%) and surface areas (> 1000 m^2 g^{-1}). On the other hand xerogels are air-dried gels with lower surface area (500-900 m^2 g^{-1}) and higher density than aerogels.

The silica walls in these gel materials are amorphous similar to those of mesoporous materials. However unlike mesoporous materials, porous gels show a lack of pore uniformity and no long-range order preventing large molecules from easily diffusing inside.[12-14]

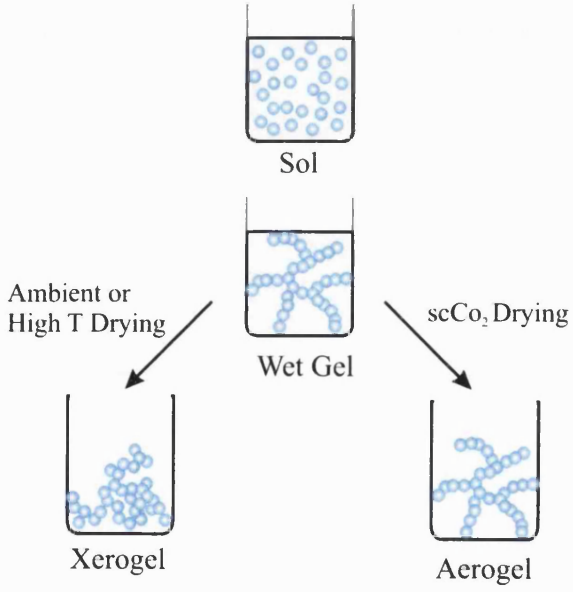

Figure1.1. Schematic of the sol-gel process to form xerogels and aerogels.

1.1.3 Mesoporous Materials

Unlike crystalline zeolites, ordered mesoporous materials usually have amorphous walls but have larger pore sizes, allowing larger molecules to diffuse inside. These materials are synthesized using surfactant micelles as structure-directing templates, which are encapsulated by an inorganic framework.[12]

1.1.3.1 Mesoporous Molecular Sieves

In 1992, researchers at Mobil R&D Corporation published the concept of surfactant-templated inorganic materials with the preparation of a new family of periodic mesoporous silicates from alkaline synthesis generically called M41S. These materials can be synthesised with up to 10 nm channel size forming the *p6mm* hexagonal phase (MCM-41), the *Ia3d* cubic phase (MCM-48), and the lamellar phase (MCM-50) (see Figure 1.2).[15, 16] The most common member of the family, MCM-41, as well as the rest of the M41S materials are prepared using a liquid crystal templating mechanism where surfactants micelles act as templates.

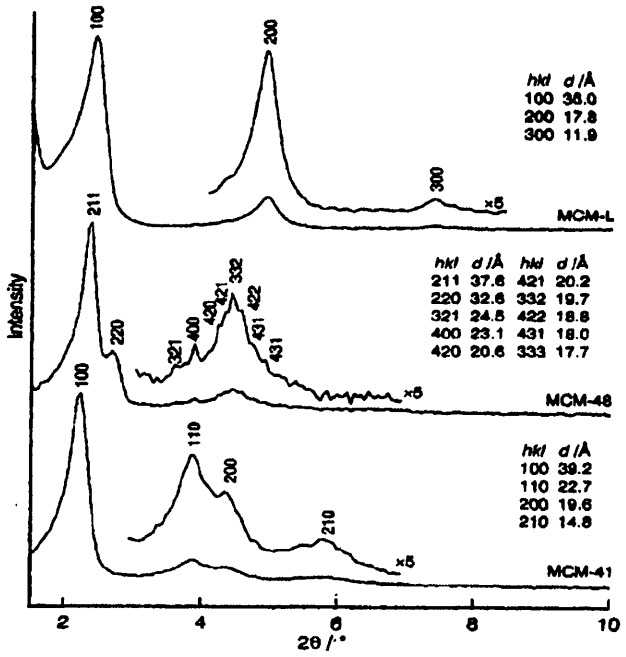

Figure1.2. Powder X-ray diffraction patterns of MCM-41 (hexagonal), MCM-48 (cubic), and MCM-50 (lamellar) materials.[15]

Beck *et al*[15] proposed an alkaline-catalysed liquid crystal templating (LCT) mechanism in which the structure is defined by the organization of the surfactant molecules into liquid crystals which serve as a templates for the formation of the MCM-41. Thus, the surfactant molecules organize forming randomly ordered rod-like organic micelles. Subsequently the mechanism, which is described in the pathway 1 in Figure 1.3 starts with the formation of the micellar rod followed by the packing of a hexagonal array of rods. Afterwards the silica precursor is incorporated in the reaction encasing the hexagonal array of rods. Alternatively, another mechanism pathway is proposed through route 2 in which the randomly ordered rod-like micelles interact with the silica which cover the micellar rod surface before they organize to form the hexagonal packing, characteristic of MCM-41. The second mechanism seems more likely since the concentration of surfactant used is too low to form a hexagonal phase when no silica is present, making the first pathway unlikely. Davis *et al*[17] carried out in situ ^{14}N NMR studies based on the MCM-41 synthesis which agreed with the second mechanism pathway proposed by Beck *et al*.

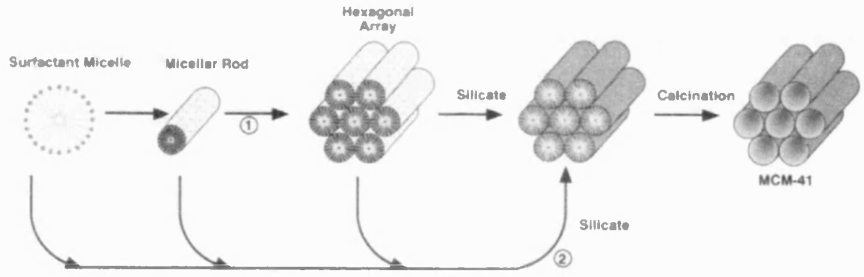

Figure1.3. Mobil group formation pathways of MCM-41.[15]

In 1993, Inagaki *et al* contributed with the synthesis of a new 2D hexagonal phase mesoporous materials called FSM-16 obtained from an ion exchange reaction of polysilicate kanemite with alkyltrimethylammonium ions. This forms through the folding together of sheets of kanemite around the surfactant micelles.[18] One of the most important contributions for the mechanism of surfactant templated mesoporous silicates formation was made by Stucky *et al*.[19-23] They suggest a model, which applies to cationic and anionic surfactants and inorganic precursors under variable pH conditions to produce 3D biphasic arrays. This model, named the cooperative templating model, involves (i) the formation of an interface between the inorganic and organic phases, (ii)

organization of the organic array, and (iii) interactions between the inorganic units bringing about polymerisation and condensation (see Figure 1.4).

The Stucky group synthesized a series of materials by changing the pH of the media and the type of surfactant. Therefore SBA-1 (*Pm3n* cubic phase), SBA-2 (3D hexagonal $P6_3/mmc$), SBA-3 (hexagonal *p6m*) were synthesized in acidic and basic media using anionic and cationic surfactants with different head groups,[19-21, 24] whereas SBA-11 (cubic $Pm\bar{3}m$) and SBA-12 (3D hexagonal $P6_3/mmc$) were obtained using non-ionic surfactants in acidic media.[25] Using triblock-copolymer-templated materials a larger pore system was achieved also under acidic media such as SBA-15 (2D hexagonal *p6mm*) and SBA-16 (cubic cage structure $Im\bar{3}m$).[25, 26]

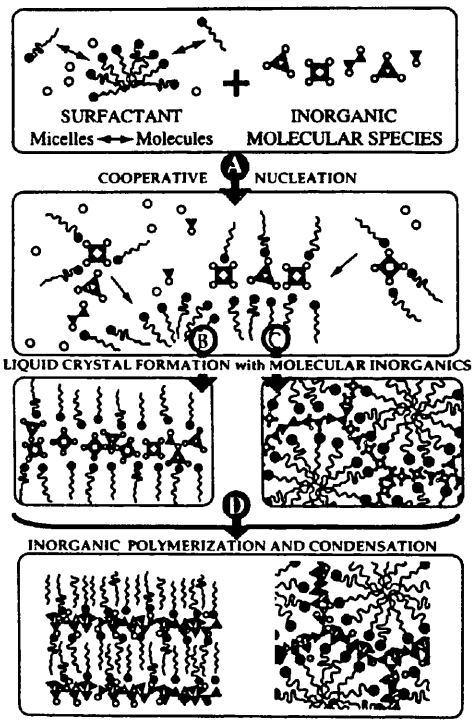

Figure1.4. Cooperative templating model for biphase materials synthesis.[21]

Syntheses of Ti-Si-M41S mesoporous molecular sieves have been also carried out to obtain the MCM-41 and MCM-48 structures by titanium incorporation in silica MCM-41[27, 28] and MCM-48[29, 30] or by mixed SiO_2 and TiO_2 formation during synthesis.[8, 10] The first successful preparation of Ti-MCM-41 was published in 1994,[28] in which the Ti was introduced in the pre-formed MCM-41 walls. Although titania incorporation chokes the pore channels and decreases the surface area of mesoporous

silica, the high reactivity of Ti (IV) towards hydrolysis and condensation makes Ti or Ti-Si mesoporous molecular sieves interesting for catalysis. A schematic of reactions to form the Ti-MCM-41 is shown in Figure 1.5, where the titania source was titanium alkoxide ($Ti(OR^n)_4$ (R = Bu^n)[31], unlike the Ti-MCM-41 synthesized by Corma *et al*[28] in which R = Et. These Ti-M41S materials present advantages in the field of selective oxidation of large molecules when compared to Ti-β-zeolites.[28, 32]

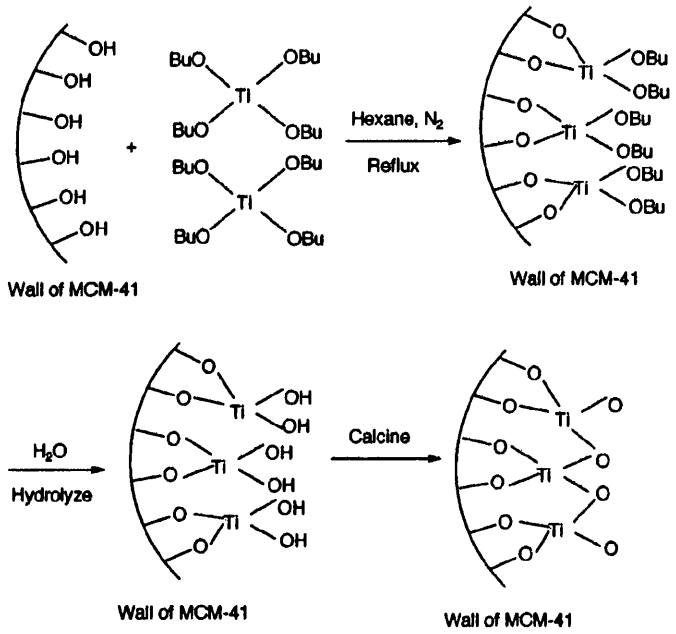

Figure1.5. Schematic of the interaction between the MCM-41 and titanium tetrabutoxide (TBOT).[31]

The synthesis of mesoporous TiO_2 was firstly reported by Antonelli *et al.*[33] This mesoporous material was synthesised via a sol-gel route with phosphate surfactants and titanium alkoxides. The addition of acetylacetonate slowed down the titania condensation providing better interaction of the inorganic species with the surfactant head groups. A pure mesoporous titania was not achieved since part of the phosphorus still remained after calcination. In 1999 Antonelli reported the first synthesis of amine surfactant- templated mesoporous titania materials free of phosphorus.[34]

1.1.3.2 *Larger Scale Structure*

Early investigations in the synthesis of surfactant-templated silicates produced powders with no well-defined structures. However materials with well-ordered morphologies have been obtained such as single crystals, monoliths and films. Some examples of single crystals synthesized under acidic conditions are SBA-1[35], SBA-6[35], SBA-16[35, 36], and non-ionic block copolymer cubic mesoporous single crystals[37]. In addition rhombic dodecahedral[38] and cubic[39] morphology single crystal of MCM-48, have also been obtained at high pH. Crack-free monoliths have been synthesised by slow solvent evaporation using amphiphilic block copolymers[40-45] non-ionic molecules[46] or alkyltrimethylammonium salts[47, 48] as structure-directing agents and different silica precursors under strong acidic media. Most of these silica monoliths are identified with hexagonal mesostructural order although recently cubic structural long range order has been reported by El-Safty *et al.*[45, 46]

Mesoporous thin films, materials more related with this thesis, will be described in detail in section 1.4. The role that surfactants and the inorganic precursors fulfil in the formation of the mesoporous materials is firstly considered and described in the next two sections.

1.2 Surfactants

The term surfactant is a contraction of "**Surface active agent**". Surfactants are organic compounds that are amphipathic, meaning they contain both hydrophobic groups, also called tails and hydrophilic groups or heads.

Surfactants reduce the surface tension of water by adsorbing at the air-water interface and the interfacial tension between oil and water by adsorbing at the liquid-liquid interface. Many surfactants can also assemble in the bulk solution into aggregates that are known as micelles.

1.2.1 Surfactant Classification

Surfactants, where the hydrophobic group consists of a long hydrocarbon chain can be classified as follows:

i) Ionic Molecules

a. Anionic, which are used for the structuring of positively charged inorganic species. Due to their low cost of manufacturing, rapid and high biodegradability, and low aquatic toxicity, these surfactants are excellent for many industrial applications.

i. fatty acids: $RCO_2^-Na^+$;

ii. sulfates: $RSO_4^-Na^+$ (eg. Sodium dodecyl sulphate (SDS))

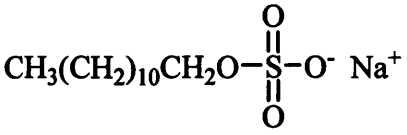

iii. sulfonates: $RSO_3^-Na^+$.

b. Cationic, which are used for the structuring of negatively charged inorganic species. Cationic surfactants are well known due to their disinfectant properties and unlike the rest of the surfactants they do not degrade in the environment and are more expensive.

i. Cetyl trimethylammonium bromide (CTAB) and other alkyltrimethylammonium salts

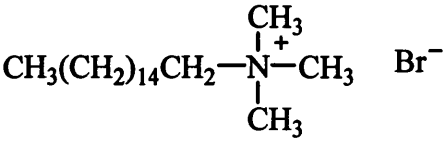

ii. Cetyl pyridinium chloride

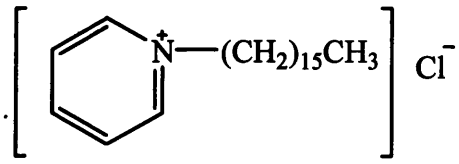

ii) Non-Ionic Molecules, without any charged interaction.

a. Amines (eg. Primary amines $C_nH_{2n+1}NH_2$).[49, 50]

b. Alkyl poly(ethylene oxide); eg. Polyoxyethylene 10 cetyl ether (Brij56®) used in experiments described later, and Polyoxyethylene 10 stearyl ether (Brij 76®). These Brij types are polydisperse surfactants that form polydisperse micelles, which are more difficult to analyse using techniques such as small angle neutron scattering (SANS). A similar surfactant is the octaethylene glycol monohexadecyl ether ($C_{16}EO_8$), which due to its high monodispersity with respect to both the alkyl chain (C_{16}) length and the oxyethylene chain length (EO) was a good surfactant for use in scattering experiments since it forms monodisperse micelles. Compared with ionic surfactants these surfactants are convenient as structure-directing agents because they are neutral, inexpensive, non-toxic, and biodegradable.[25]

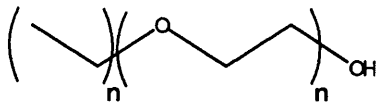

c. Alkyl polyglucosides, including: Octyl glucoside and decyl maltoside.

iii) Amphoteric Molecules. Examples are phospholipids, one of the main constituents of biological membranes: they insulate the cells from the surrounding medium.

iv) Block Copolymers are polymers formed when two different types of monomer are linked in the same polymer chain. These copolymers can also act as surfactants forming micelles in solution. For this to occur one block must be more hydrophobic than the other. These polymers have been used to create materials with much larger pore dimensions (50-300nm) depending on the chain length of the polymer.[25]

a. Diblock copolymers such as PS-b-PMMA (polystyrene-b-poly(methyl methacrylate))

b. Triblock copolymers, such as poly(oxyethylene)-poly(oxypropylene)-poly(oxyethylene) $(EO)_x(PO)_y(EO)_x$ where the EO groups are the hydrophilic part and PO groups the hydrophobic part, are commonly

used in the formation of mesoporous materials. Some examples are: Pluronic P123® ($(EO)_{20}(PO)_{70}(EO)_{20}$) and Pluronic F127® ($(EO)_{106}(PO)_{70}(EO)_{106}$).

c. Tetrablocks, pentablocks, etc. copolymers.

1.2.2 Structure in Aqueous Media

The surfactant phase formed in aqueous solution depends on the surfactant concentration and its counterion. Hence the surfactant organization may be predicted by the molecular packing parameter based on the geometry. This parameter is defined as $g = v/al$ where v is the volume of the hydrocarbon chain, a is the head-group area and l the maximum effective chain length. Typically, l and v can be calculated as:

$$v = (27.4 + 26.9\,n)\,\text{Å}^3 \text{ per hydrocarbon chain}$$

$$l = (1.5 + 1.265\,n)\,\text{Å} \text{ per hydrocarbon chain}$$

where n is the number of carbon atoms.[51] The shape of an equilibrium aggregate depends on the packing parameter as follows: $0 < v/al < 1/3$ for a spherical micelle, $1/3 < v/al < 1/2$ cylindrical micelle, and $1/2 < v/al < 1$ for a bilayer. For the majority of surfactants in solution, v/l is approximately constant (~21 Å^2). Thus, differences in the micelle configurations are due to a change in the effective packing of the head-groups. Therefore the "*a*" parameter is sensitive to the surfactant counterion and pH, if the head-group is ionisable.

The concentration at which surfactants begin to form micelles is known as the critical micelle concentration or CMC. As the phase diagram in Figure 1.6 shows at low solution concentrations, surfactant molecules are in a dynamic equilibrium of different forms of single molecules. When micelles form in water, their tails are oriented in order to avoid the water, which form a core, and their heads are oriented towards the aqueous solution formming an outer shell, or corona. Therefore spherical micelles appear beyond the first critical micelle concentration (CMC1) which is the most energetically favourable form. Increasing the concentration the micelle aggregation number rise and rod-like micelles are formed (CMC2). At still higher concentrations, various liquid crystal phases are observed, such as the hexagonal, cubic and finally lamellar liquid crystal. Liquid crystals become one structure or another depending on surfactant head-group area or tail length. At low temperatures, crystals come out of the solutions as solids.[52]

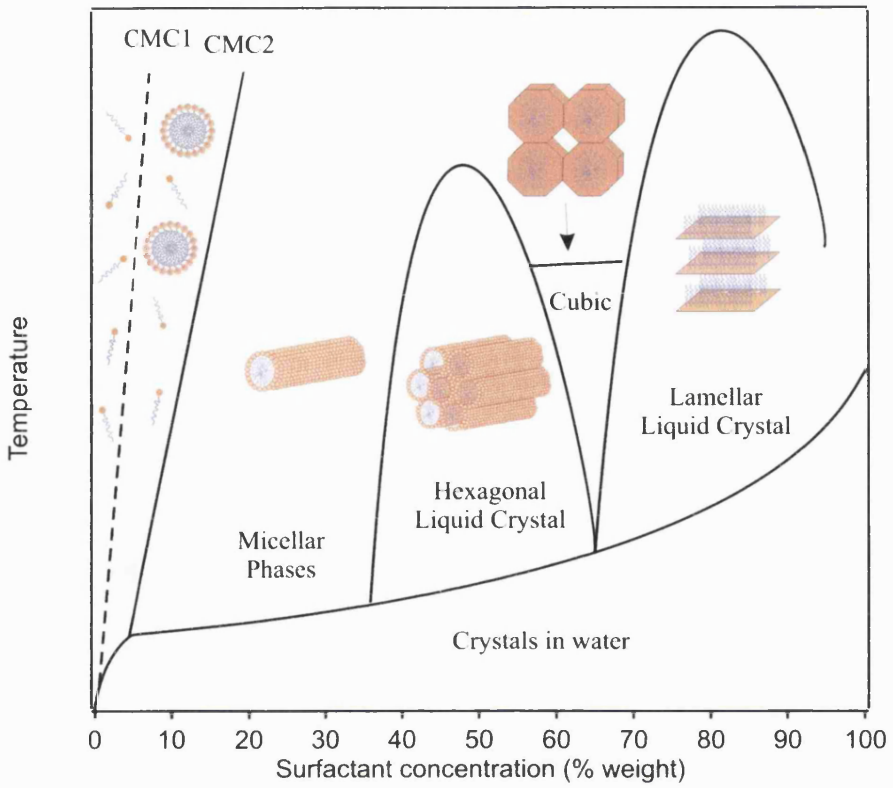

Figure1.6. Phase diagram showing different structure formation using CTAB as a surfactant in aqueous solution (after Raman *et al.* (1996)).[52] The CMC1 is the critical micelle concentration for the formation or spherical micelles and the CMC2 for the formation of rod-like micelles. Both CMC have been exaggerated to higher concentrations so they are visible on this scale.

Is important to emphasize that in the case of mesophase thin films grown at room temperature, the surfactant concentration is between the CMC1 and CMC2 in the initial synthesis solution.

1.3 Inorganic Materials

Silicon and transition metal alkoxides, $M(OR)_x$, especially (Ti and Zr) are widely used as a molecular precursors in the production of glasses and ceramics.[53-56] In particular mesoporous silica materials have been more explored than mesoporous transition metal TM-based materials, due to the lower reactivity of the silica alkoxide precursors.[1, 57, 58] The main reason why silicon alkoxides are more widespread than TM alkoxides used as precursors in sol-gel processing is the rapid kinetics of nucleophilic reactions. During hydrolysis and condensation the high reactivity of TM alkoxides causes fast chemical and structural changes making their study more difficult than $Si(OR)_4$.[13, 59]

1.3.1 Silica Precursors

The chemistry of silicon alkoxides has been studied by the condensation and polymerization processes in sol-gel reactions.

The silica sol is most often synthesized by hydrolysis of tetrafunctional alkoxide precursors using acid or base as a catalyst.[13] The most commonly used precursor materials are tetramethoxysilane (TMOS) and tetraetholxysilane (TEOS). Because these precursors are quite expensive, cheaper sources such as silicic acid and sodium silicate solution are also used.

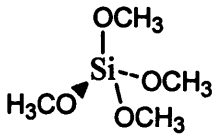

TMOS molecule

In the sol-gel process a sol is first formed by mixing a liquid alkoxide precursor (TMOS or TEOS), water, a cosolvent, and an acid or base catalyst at room temperature.

In this solution three reactions can occur:

Hydrolysis

$(RO)_3SiOR + H_2O \rightarrow (RO)_3SiOH + ROH$ (1)

Water condensation

$2(RO)_3SiOH \rightarrow (RO)_3Si\text{-}O\text{-}Si(OR)_3 + H_2O$ (2)

Alcohol condensation

$(RO)_3SiOH + ROSi(OR)_3 \rightarrow (RO)_3Si\text{-}O\text{-}Si(OR)_3 + ROH$ (3)

During the hydrolysis reaction (Eq. 1) alkoxide groups are removed by acid- or base-catalyzed hydrolysis reactions. During alkaline catalysed polymerizations silica species become negatively charged whereas positively charged silica species are obtained in acidic conditions. Subsequently networks of O-Si-O linkages are formed in condensation and polymerisation reactions involving hydroxyl groups (Eq. 2 & 3).

Typically the gel-synthesis procedures are used to form bulk gels,[60] films,[61] fibers[62], and powders [63] with different polymeric structures. Therefore depending on the alkoxide molar ratio, pH, temperature and solvent, further condensation can cause modification in the structure (e.g. linear, chains, clusters, and colloidal particles) and properties of the polysilicate products.[13, 64] The processing parameters that influence the porosity are the pH and aging. For example gels prepared from TEOS at pH less than 3.5 are microporous and at pH higher than 3.5 are mesoporous.[65]Ying *et al.* reported that silica gels prepared in acidic media are energetically more stable and require lower temperatures than the alkaline ones during drying.[66]

Concentrating on surfactant-templated mesostructured silicate films, hydrolysis and condensation (Eq. 1, 2 & 3) also occur with methanol from e.g. TMOS hydrolysis as the cosolvent. For the synthesis of the mesostructured silicate films TMOS is used as the silica precursor instead of TEOS. This is due to the inductive effect of the substituents attached to silicon, which affect the alkoxysilane hydrolysis rate depending on the acidic or basic conditions. The acidity of the substituents attached to silicon in the acid-catalysed hydrolysis increases by the effect of electron-withdrawing groups with a consequent increase of the hydrolysis rate (see Figure 1.7).[67] Therefore the use of TMOS favours the hydrolysis rate due to its acidity as well as providing less steric effect since the methoxy group is relatively smaller than the ethoxy group in TEOS.[63]

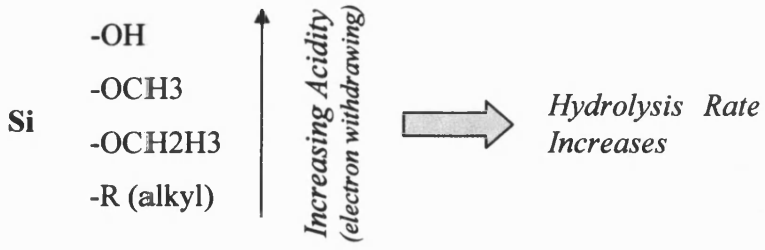

Figure1.7. Inductive effect of substituents attached to silicon.[68]

1.3.2 Titania Precursors

Titania has been studied extensively due to its wide applications in pigments, photocatalysts,[69] coatings,[70] and photoconductors.[71, 72] Its effectiveness of as a photocatalyst depends on its crystal phase, particle size, and crystallinity. Therefore both small particle sizes, which provide high surface area, and the most active titania crystal phase, anatase, are desired to produce the best photocatalyst.[73] These materials have been obtained either directly from titanium-bearing minerals or from titanium salts (such as $TiCl_4$) or alkoxides ($Ti(OR^n)_4$). The synthesis of titania from alkoxides follows similar hydrolysis and condensation reactions as silica:[74, 75]

Hydrolysis: four possible steps

$Ti(RO)_4 + H_2O \rightarrow Ti(RO)_3(OH) + ROH$ (1)

$Ti(RO)_3(OH) + H_2O \rightarrow Ti(RO)_2(OH)_2 + ROH$ (2)

$Ti(RO)_2(OH)_2 + H_2O \rightarrow Ti(RO)(OH)_3 + ROH$ (3)

$Ti(RO)(OH)_3 + H_2O \rightarrow Ti(OH)_4 + ROH$ (4)

Water condensation

$Ti\text{-}OH + HO\text{-}Ti \rightarrow Ti\text{-}O\text{-}Ti + H_2O$ (5)

Alcohol condensation

$Ti\text{-}OR + HO\text{-}Ti \rightarrow Ti\text{-}O\text{-}Ti + ROH$ (6)

Transition metal alkoxides are mostly used as precursors. Due to the higher Lewis acidity and the unsaturated coordination they can react with nucleophilic species, which affects the hydrolysis and condensation kinetics.[13, 76, 77] Apart from that, increasing the alkyl chain length in the titanium *n*-alkoxides ($Ti(OR^n)_4$) decreases the hydrolysis rate because of the consequent steric effect.[76] It has been observed that when R = Et, Pr^n, or Pr^i precipitation takes place, whereas for $R = Bu^n$ stable sols are obtained.[13] Studies of the hydrolysis behaviour for titanium tetrabutoxide ($Ti(OBu)_4$, abbreviated as TBT or TBOT) as a function of H_2O to OBu^n molar ratio were carried out by Winter and Boyd.[78, 79] They concluded that for molar ratios smaller or equal than 2.5 polymers were formed whereas for ratios higher than 3 TiO_2 precipitates appeared. Ishino *et al.* also studied the hydrolysis of TBOT but in butanol concluding that the hydrolysis was faster than the condensation.[74] The literature shows a considerable number of reports about the preparation of TiO_2 as powders and films from sol-gel processing. TiO_2 gels have been synthesized as a pure monoliths[80] as well as monolithic composite systems (TiO_2-SiO_2[81, 82] and PbO-TiO_2[83]), and silica-titania films.[84 85]

synthesized as a pure monoliths[80] as well as monolithic composite systems (TiO_2-SiO_2[81, 82] and PbO-TiO_2[83]), and silica-titania films.[84 85]

1.4 Mesoporous Thin Films

Silica has been used by a considerable number of investigators as the starting point for the formation of ordered mesoporous materials based on the surfactant-inorganic composites. Surfactant-templated mesoporous silica thin films are of great interest because of their multiple applications. Due to their geometry, these materials have a potential industrial applications as molecular sieve membranes, catalysis supports, and surface coating for sensors,[86, 87] insulation and optical devices.[88]

In early studies, surfactant-templated silicates were synthesized as powders with no well-ordered structures, however later work reports silicate materials with well-defined morphologies such as single crystals, monoliths (already mentioned in section 1.1.3.2) and films with thickness ranging from nanometres to millimetres.

This section will concentrate on the methods to create these films giving details of their properties and composition.

1.4.1 Methods of Synthesis

There are several methods to create thin films as the next organization chart shows:

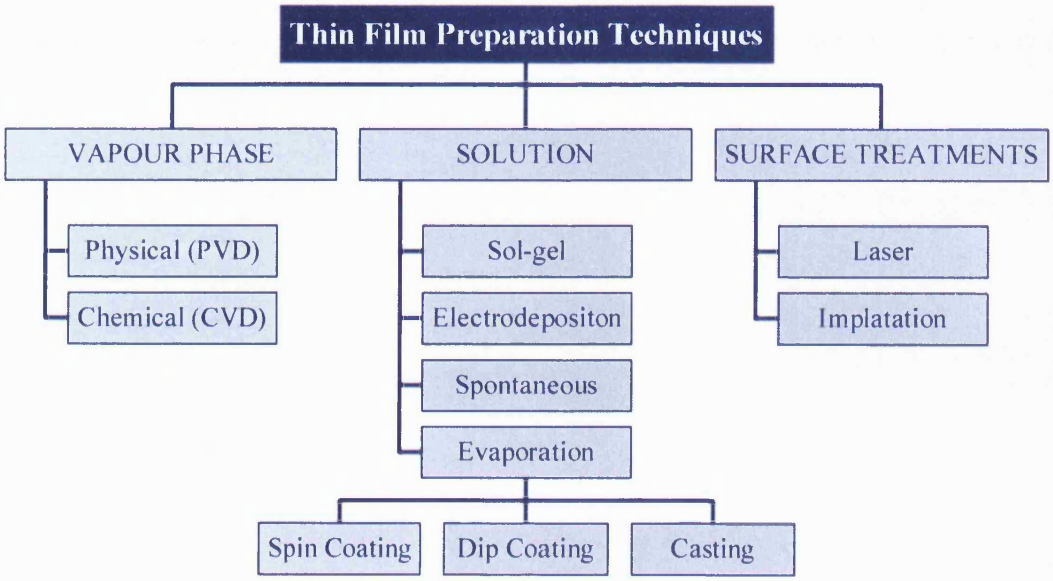

1.4.1.1 Evaporation Assisted Methods

i) *Spin coating*

Transparent thin films are formed on the substrate with thickness controlled by spin rate. The first report of these highly ordered nanostructured composites was published by Ogawa in 1994.[89] TMOS and an acidic solution containing C_{16}TAB was mixed and spin coated on to a substrate and dried at 100°C resulting in films thicker than 1 μm. In later papers X-ray diffraction (XRD) measurements applied to spin-coated films show a structural transition from lamellar to hexagonal as silica-surfactant (TMOS-C_{16}TAB) molar ratio increases. In 1997 and 1998 Ogawa *et al.* reported the synthesis of thin films of silica-alkyltrimethylammonium (akyl=decyl, dodecyl, tetradecyl, hexadecyl and octadecyl) chloride mesostructured materials by spin coating. They studied the *d* values of the silica- C_nTAC mesostructured materials as a function of alkyl chain length observing a gradual increment of the *d* values as the number of carbons in the alkyl chains increase.[90, 91] Another spin coated film was reported by Anderson *et al.*,[92] in which an homogeneous alkaline-catalysed TMOS-CTAB solution in a water-methanol solvent was used to form mesostructured silica films. Similar films were made using ethylene glycol instead of methanol as cosolvent to control evaporation.[93] Liu *et al.*[94] reported the first silicate-surfactant film with a cylindrical pore structure. An acidic solution made up with CTAB and TMOS in a water-ethanol solvent was spin coated on to silicon wafers, which gave stable 3D structures after calcination. Non-ionic poly(oxyethylene ether) surfactants were used to form a disordered mesophase silica-surfactant films obtaining thicknesses up to 1.2 μm.[95] In most cases, films have been synthesised from a water-ethanol solution containing CTAB and a silica sol prepared with an alkoxysilane under acidic conditions. During the drying process the solvent evaporates and ordered micellar domains form. Studies on the variation of surfactant-silica molar ratios show different mesophase structures such as lamellar obtained with dye impregnation,[96, 97] lamellar,[98] 2D hexagonal[98] (also called by some authors as oriented 1D hexagonal),[99] 3D hexagonal,[100] and cubic[98]. The 2D hexagonal structure refers to the formation of arrays of cylindrical micelles with their axis oriented parallel to the film plane. The 3D hexagonal structure can be defined as a hexagonal packing of spherical micelles.

Studies on the synthesis of titania thin films by spin coating can also be found in the literature such as a recent work published by Li *et al.* The TiO_2 films were obtained

Studies on the synthesis of titania thin films by spin coating can also be found in the literature such as a recent work published by Li *et al.* The TiO_2 films were obtained by sol-gel processing using a cationic surfactant as template and a titanium alkoxide as the titania precursor in a water/ethanol solution. The films were found to have a lamellar structure and a wormlike pore structure after calcination.[101]

Figure1.8. Spin coater with stage spinning up to 8,000 rpm.

ii) *Dip coating*

This technique is similar to spin coating where the substrates are drawn from a homogeneous precursor solution and allowed to drain to a particular thickness. It is advantageous for the fast film formation on non-planar surfaces. This rapid, controllable technique leaves uniform and ordered pores in the range of 2-10 nm after removal of the structure directing agents from the films. Films with high optical quality require a low silicate precursor condensation rate and a homogeneous wetting of the substrates. For silica-based films the acid catalysed solutions consist of a small amount of water highly diluted in a solvent, usually alcohol, which promotes the formation of the film via E.I.S.A. (Evaporation-Induced Self-Assembly). This process, first introduced by Brinker *et al.*,[102] involves the rapid evaporation of the volatile solvent, which induces the condensation of the inorganic precursors and the formation of the mesophase. Other dip-coated films were synthesised using cationic surfactants with TEOS in an acidic water-ethanol solutions following different dip-coating methods. As a result CTAB-templated films were found to produce lamellar,[103] 2D hexagonal,[26, 47, 103-108] 3D hexagonal,[26, 109, 110] and cubic[110, 111] phases. CTEAB-templated films[26, 104] (a large-head-group cationic surfactant) showed cubic, and 2D hexagonal upon increasing the acid concentration. A large number of 2D hexagonal silicate-surfactant composites were obtained using block copolymers[26] (e.g. Pluronic P123, Pluronic P103 etc.) in a TEOS

oxide (PO) (e.g. Pluronic F127).[26] The lower-molecular-weight alkyl(ethylene oxide) non-ionic surfactants were also used to create well-ordered 2D hexagonal phase, which with an increase in the acid concentration forms a 3D cubic phase.[112] Dip coated silica-surfactants films have also been studied using fluorescent molecules as a film structure probe. Pyrene, coumarin-153 (C-153)[113] or 2,6-TNS[111] are fluorescent probes molecules sensitive to the polarity of their microenvironment. These dyes can be incorporated into the surfactant region giving information about film structure. Therefore using fluorescence methods the *in situ* evolution of the mesophase and structure progression can be followed.[111, 114]

Works concerning other metal oxide and in particular dip-coated mesoporous TiO_2 thin films have also been reported. The first report of the preparation and characterization of uniform mesoporous TiO_2 thin films was published by Grosso *et al* followed by Hwang *et al.*[115, 116] In these two works ethanol-water solutions containing poly (ethylene oxide)-type surfactants used as structure directing agents and $TiCl_4$ as precursor were prepared. Glass or silicon substrates were dip-coated obtaining 2D hexagonal structure with mesostructure shrinkage after calcination. This method has been improved by Sanchez *et al.* in many subsequent papers.[106, 117, 118]

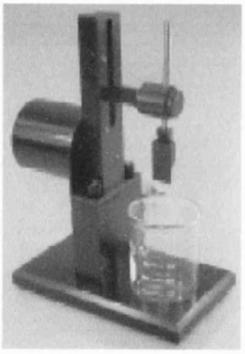

Figure1.9. Dip coater for 1 mm thick glass microscope slides.

iii) *Casting*:

Synthesis solution is dropped on to a substrate and left to solidify producing much thicker films. In 1995 Attard *et al.* mentioned very briefly a mesophase silica-surfactant film formed by casting using non-ionic surfactant as template with a TMOS silica source.[119] Ryoo *et al.* reported in 1997[120] the formations of cast films and monoliths up to 0.5 mm thick using TEOS as precursor and cationic surfactant in an azeotropic mixture. Other macroscale cast films using block copolymer templates and silicon and aluminium alkoxides as inorganic precursors were also reported.[121, 122]

1.4.1.2 Spontaneous Film growth at different interfaces

i) *Solid-liquid*

Films can grow onto a substrate from solution allowing surfaces of arbitrary shape and composition to be coated with an aligned mesoscale structure.[123] Thin films of mesostructured silicates can be formed at hydrophobic or hydrophilic surfaces. In a system under acidic conditions the surfactant micelle self-assembly and the inorganic precursor condensation take place forming an inorganic-organic nanocomposite at the solid-liquid interface.

Spontaneous growth of silicate films on mica substrates was first reported by Yang *et al.*[124] The mica substrate was laid horizontally and covered by an acidic solution containing CTACl as surfactant and TEOS as inorganic precursor. Thin ordered films of mesoporous silica were grown with thickness approximately between 0.2 and 1.0μm. Another important contribution of mesostructured surfactant-silica films on solid substrates was reported by Aksay *el al.*[125] The films were synthesised from TEOS-CTAB acidic solutions on mica, graphite and silicon substrates. XRD results revealed a surfactant layer alignment with the crystalline mica and graphite substrates, whereas with amorphous silica a random arrangement was observed. Most of the mesoporous silicate films grown at solid-liquid interface have been prepared under acidic conditions using CTAB or CTACl as structure directing agents and TEOS as the inorganic precursor with different molar ratios. These films grow on to different substrates, such as graphite,[126] gold,[127] borosilicate glass,[128] mica,[129] and silicon (110)[123, 130] or (100)[131, 132] face. Usually they form hexagonally packed cylindrical channels, which can be oriented parallel or non-parallel to the surface of the substrate

according to the type of substrate, the physical methods used (e.g. alignment through shear[133]), the hydrophobicity of some substrates (e.g. silicon (100) face[131]) etc.

ii) *Liquid-liquid*

Ordered mesostructured porous silicas can also be synthesized at the liquid-liquid interface. In 1996 Schacht *el al.*[134] reported a method for the formation of mesoporous silicate fibers, spheres and thin sheets at the oil-water interface. A first solution was prepared mixing TEOS and organic solvents such as n-hexane, benzene, toluene or mesitylene. A second solution was made up with CTAB in an acidic aqueous media. The first solution was added into the second and an oil-water emulsion was formed by stirring at room temperature. Surfactant molecules diffuse to the oil-water interface, which helps to stabilize the emulsion and leads the condensation of the TEOS at the interface. When the acid synthesis is carried out in a water-oil mixture, a solid composite will be formed at the interface between oil and water. The morphology of the material can be controlled by the stirring rate. Therefore increasing the stirring rate produced spherical morphologies that decreased in size whereas under slow stirring rope-like fibers are obtained. Huo *et al.*[135] reported another case of mesoporous silicate fibres growing at an oil-water interface under acidic conditions. Silica fibers were grown in the hydrophilic region (water) while alternative silica structures are formed in the hydrophobic part (oil). More recently silica nanostructures were synthesized by variation of the pH at the liquid-liquid interface.[136] In the laurylamine/tetraethoxysilane (LA/TEOS) system a hexagonal array or bicontinuous cubic phases were formed in the narrow pH region from 10 to 11.5. Small-angle X-ray scattering measurements were carried out to study the structural transition from early to final stages of the process.[136, 137]

iii) *Air-liquid*

The first report on surfactant-silicate films growing spontaneously at the air-solution interface was published by Yang *et al.*[138] The films were obtained from a dilute acidic solution of TEOS/CTACl resulting in film thicknesses of between tens of nanometres up to 0.5 μm. Most of the structural studies, including the first report and further work done by Yang *et al.*[138, 139] suggest that the mesoporous thin films are formed by self-assembled surfactant micelles in solution which template the polymerised silica. The micelles pack at the air-liquid interface to form highly ordered arrays. In these cases the final structure is a hexagonal mesophase with the cylindrical

micelles aligned parallel to the surface.[140, 141] However exceptions must be cited since the existence of a cubic phase during the initial stages of growth was observed by Ruggles *et al.*[142] and non-oriented films with hexagonal structure using a novel two-headed quaternary ammonium surfactant (or gemini)[143] were reported by Tolbert *el al.*[144] These and other investigations on the self-assembly of the mesophase surfactant silica thin films at the air-liquid interface were based on the use of several techniques such as X-ray and neutron reflectivity,[140, 145, 146] XRD,[142] grazing incident X-ray diffraction (GIXD),[141, 147] TEM and SEM,[138] and optical microscopy.[139] Most investigations have been focused on the structural characterization of the final films and only a few have studied the films during the formation process using techniques such as off-specular X-ray reflectivity,[140, 148, 149] small angle neutron scattering (SANS)[150] and Brewster angle microscopy (BAM).[151, 152] Brown *et al.*[145, 146] studied the film formation process and suggested that the mechanism of these mesoporous silicates films growing at the air-water interface involves two main stages. The first stage is the induction period, whose duration depends upon the concentration of the solution, and the transition and growth phases, which quickly produce a highly organized structure. Similar stages were observed and reported by Brennan *et al.*[140] The growth at the air-water interface for surfactant-templated mesoporous silica thin films was studied using X-ray reflectivity techniques observing a clear concentration-dependence of the induction period. For the longest induction times the film nucleates at the surface, as suggested by the earlier experiments, while for the shortest ones the micelles form particles in the bulk solution, which diffuse to the surface where they pack to form the film.

Some of the mentioned techniques are explained in more detail in chapter 3.

This thesis examines the growth of mesoporous thin films at the air water interface using some of the techniques mentioned above to study the structure at the air-water interface once the film is formed and some others to study structures and mechanisms during the growth process.

1.4.2 Thin Film Formation Parameters

In this section some of the parameters, which affect the formation of surfactant-templated silica thin films at the air water interface, are listed and described as follows:

i) *Type of surfactant and inorganic species*

a. Inorganic precursor- surfactant head group interaction

The molecular interaction between an inorganic material and a surfactant head group can change the formation pathways of the film and consequently the mesostructure. Since 1994 six possible molecular reaction pathways have been identified during the liquid crystal templating (LCT) process (see Table 1.1).[21, 49, 57]

Table 1.1. Schematic representation of the different inorganic-surfactant head group interactions where I represents the inorganic precursor; S the surfactant head group; X^- the counter anion; M^+ the metal cation.

I-S head group interaction	Examples
Electrostatic 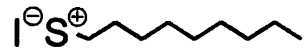	I = Si (in alkaline solution) S = trimethylammonium
Electrostatic 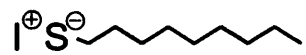	I = Sb, Si (in acidic solution) S = sulfonate
Electrostatic 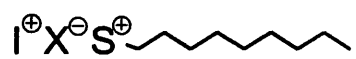	I = Si; X = Cl S = trimethylammonium
Electrostatic 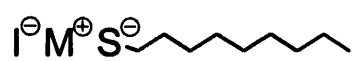	I = Al; M = Na S = phosphate
Hydrogen Bonding 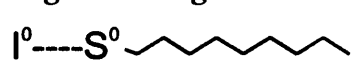	I = Si S = amine or polyethylene oxide
Covalent Bonding 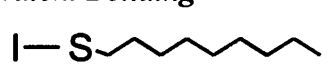	I = Nb, Ta S = amine

Huo *et al*[21] reported a possible formation of silicate mesostructures through the $I^+ X^- S^+$ synthesis route via liquid-crystal templating in a acidic media. Surfactant-templated silica composites have been synthesised not only as bulky solid materials but also as films through the counterion-mediated interaction ($I^+ X^- S^+$) between the surfactant and the silica oligomers.[146] Tanev and Pinnavaia[49] showed that mesoporous

silica sieves could also be prepared through a neutral templating route by hydrogen-bonding interaction. However, the mechanism of templating and the processes leading to development of well-defined secondary structures are still under debate. Work reported by Edler *et al*[140, 148] suggests two possible formation mechanisms for cationic surfactant-templated silica thin films, which are dependent upon the silica precursor and surfactant concentration, and the pH (parameters mentioned next).

In this thesis these mechanisms are described for cationic surfactant-templated silica thin films under different temperature and humidity conditions as well as for non-ionic and mixed surfactant-templated silica thin films, in which electrostatic and hydrogen bonding interactions are presented.

b. Substituents of the inorganic precursors

It has been explained in sections 1.3.1 and 1.3.2 how the alkyl chain length of the silica and titanium *n*-alkoxides ($Si(OR^n)_4$ and $Ti(OR^n)_4$) affect the hydrolysis and condensation rate and therefore to the global mechanism and to the final mesophases. This was not varied in this thesis.

c. Surfactant chain length

The effect of different block lengths of triblock copolymers, Pluronic surfactants ($(EO)_x(PO)_y(EO)_x$) in the formation of mesoporous silica via LCT has been investigated by Flodstrom *et al.*[153, 154] Results show that the EO-block length of the polymers determines the mesostructure of the silica while the PO-block length has a great effect on the pore diameter. However, not many studies concerned with the surfactant tail or head length variation have been published for surfactant-templated silicate films at the air-water interface. An important contribution was reported by Ruggles *et al.*[155] In this work variation in the chain length and the ionic strength of the *n*-alkyltrimethylammonium bromide and chloride (C_nTAB and C_nTACl) in the formation of surfactant-templated silicate films at the air-water interface was studied to test the generality of their proposed mechanism of structure transformation. The possible mechanism describes a sphere to rod transition in the micellar structure in which the addition of salts changes the film growth rate being slower for chloride than bromide counteranions.

ii) *Surfactant and Inorganic precursor concentration*

It has been reported that the film formation time, mechanism, and the final mesophase structure changes with regard to the variation of surfactant-silica molar ratio

in the formation of surfactant-templated mesoporous films grown at the air-water interface. The formation of these thin films has been carried out varying the silica precursor concentration (TMOS) using CTAB[140, 148] as cationic surfactant and in this thesis octa-ethylene glycol mono n-hexadecyl ether ($C_{16}EO_8$)[156] as non-ionic surfactant. In the TMOS/CTAB system the film formation rate shows a "horse-shoe" dependence whereas it is shown in chapter 5 that for TMOS/ $C_{16}EO_8$ the dependence is lineal. This behaviour affects the formation mechanism and consequently to the final mesostructure of the film. Both systems are reported in more detail in chapters 4, 5, and 6.

iii) *pH*

Depending on the pH value the thin film growth can follow different reaction pathways, or can change completely the evolution in the formation process. Then, in the spontaneous formation of surfactant-templated silica mesoporous materials a change in the pH affects the final material structure as follows:

If pH > 2, will produce powders

If pH < 2, films will be formed

In the pH range from 0 to 2 there is a significant variation of film formation times, mechanisms and structure. Experiments reported by Edler *et al.*[148] demonstrate the variation of film formation time with acid concentration. Results show that for pH values between 0.8 and 0.2 the film formation rate increases as the pH decreases.

iv) *Temperature and Humidity*

Temperature and humidity appear to have an important effect in the growth process and final structure of mesostructured silica-surfactant thin films. Both parameters, detailed studied in chapter 4, are directly related with the evaporation process occurring during the film formation at the air-water interface.

For a better understanding of these effects, the use of special characterization techniques is essential; therefore a brief description is considered in chapter 3.

1.5 References

(1) Sayari, A.; Liu, P. *Microporous Materials* **1997**, *12*, 149-177.
(2) Corma, A. *Chemical Reviews* **1997**, *97*, 2373-2419.
(3) Freyhardt, C. C.; Tsapatsis, M.; Lobo, R. F.; Balkus, K. J.; Davis, M. E. *Nature* **1996**, *381*, 295-298.
(4) Taramasso, M.; Perego, G.; Notari, B.: US Pat.,, 1983.
(5) Adam, W.; Corma, A.; Reddy, T. I.; Renz, M. *Journal of Organic Chemistry* **1997**, *62*, 3631-3637.
(6) Reddy, J. S.; Kumar, R.; Ratnasamy, P. *Applied Catalysis* **1990**, *58*, L1-L4.
(7) Huybrechts, D. R. C.; Debruycker, L.; Jacobs, P. A. *Nature* **1990**, *345*, 240-242.
(8) Camblor, M. A.; Corma, A.; Martinez, A.; Perezpariente, J. *Journal of the Chemical Society-Chemical Communications* **1992**, 589-590.
(9) Sastre, G.; Corma, A. *Chemical Physics Letters* **1999**, *302*, 447-453.
(10) Camblor, M. A.; Corma, A.; Esteve, P.; Martinez, A.; Valencia, S. *Chemical Communications* **1997**, 795-796.
(11) Sanjuan, A.; Alvaro, M.; Corma, A.; Garcia, H. *Chemical Communications* **1999**, 1641-1642.
(12) Edler, K. J.; Roser, S. J. *International Reviews in Physical Chemistry* **2001**, *20*, 387-466.
(13) Brinker, C. J.; Schaefer, D. W. *Sol-Gel Science. The Physics and Chemistry of Sol-Gel Processing*; Academic Press: Boston, 1990.
(14) Brinker, C. J. In *Colloid Chemistry of Silica*, 1994; Vol. 234, pp 361-402.
(15) Beck, J. S.; Vartuli, J. C.; Roth, W. J.; Leonowicz, M. E.; Kresge, C. T.; Schmitt, K. D.; Chu, C. T. W.; Olson, D. H.; Sheppard, E. W.; McCullen, S. B.; Higgins, J. B.; Schlenker, J. L. *Journal of the American Chemical Society* **1992**, *114*, 10834-10843.
(16) Kresge, C. T.; Leonowicz, M. E.; Roth, W. J.; Vartuli, J. C.; Beck, J. S. *Nature* **1992**, *359*, 710-712.
(17) Chen, C.-Y.; Burkett, S. L.; Li, H.-X.; Davis, M. E. *Microporous Materials* **1993**, *2*, 27-34.
(18) Inagaki, S.; Fukushima, Y.; Kuroda, K. *Journal of the Chemical Society-Chemical Communications* **1993**, 680-682.
(19) Monnier, A.; Schuth, F.; Huo, Q.; Kumar, D.; Margolese, D.; Maxwell, R. S.; Stucky, G. D.; Krishnamurty, M.; Petroff, P.; Firouzi, A.; Janicke, M.; Chmelka, B. F. *Science* **1993**, *261*, 1299-1303.
(20) Huo, Q. S.; Margolese, D. I.; Ciesla, U.; Feng, P. Y.; Gier, T. E.; Sieger, P.; Leon, R.; Petroff, P. M.; Schuth, F.; Stucky, G. D. *Nature* **1994**, *368*, 317-321.
(21) Huo, Q. S.; Margolese, D. I.; Ciesla, U.; Demuth, D. G.; Feng, P. Y.; Gier, T. E.; Sieger, P.; Firouzi, A.; Chmelka, B. F.; Schuth, F.; Stucky, G. D. *Chemistry of Materials* **1994**, *6*, 1176-1191.
(22) Stucky, G. D.; Monnier, A.; Schuth, F.; Huo, Q.; Margolese, D.; Kumar, D.; Krishnamurty, M.; Petroff, P.; Firouzi, A.; Janicke, M.; Chmelka, B. F. *Molecular Crystals and Liquid Crystals Science and Technology Section a-Molecular Crystals and Liquid Crystals* **1994**, *240*, 187-200.
(23) Firouzi, A.; Kumar, D.; Bull, L. M.; Besier, T.; Sieger, P.; Huo, Q.; Walker, S. A.; Zasadzinski, J. A.; Glinka, C.; Nicol, J.; Margolese, D.; Stucky, G. D.; Chmelka, B. F. *Science* **1995**, *267*, 1138-1143.
(24) Huo, Q. S.; Leon, R.; Petroff, P. M.; Stucky, G. D. *Science* **1995**, *268*, 1324-1327.

(25) Zhao, D. Y.; Huo, Q. S.; Feng, J. L.; Chmelka, B. F.; Stucky, G. D. *Journal of the American Chemical Society* **1998**, *120*, 6024-6036.
(26) Zhao, D.; Yang, P.; Melosh, N.; Feng, J.; Chmelka, B. F.; Stucky, G. D. *Advanced Materials* **1998**, *10*, 1380-1385.
(27) Zhang, W. H.; Froba, M.; Wang, J. L.; Tanev, P. T.; Wong, J.; Pinnavaia, T. J. *Journal of the American Chemical Society* **1996**, *118*, 9164-9171.
(28) Corma, A.; Navarro, M. T.; Pariente, J. P. *Journal of the Chemical Society-Chemical Communications* **1994**, 147-148.
(29) Morey, M.; Davidson, A.; Stucky, G. *Microporous Materials* **1996**, *6*, 99-104.
(30) Corma, A.; Kan, Q. B.; Rey, F. *Chemical Communications* **1998**, 579-580.
(31) Zheng, S.; Gao, L. A.; Zhang, Q. H.; Guo, J. K. *Journal of Materials Chemistry* **2000**, *10*, 723-727.
(32) Blasco, T.; Camblor, M. A.; Corma, A.; Esteve, P.; Martinez, A.; Prieto, C.; Valencia, S. *Chemical Communications* **1996**, 2367-2368.
(33) Antonelli, D. M.; Ying, J. Y. *Angewandte Chemie-International Edition in English* **1995**, *34*, 2014-2017.
(34) Antonelli, D. M. *Microporous and Mesoporous Materials* **1999**, *30*, 315-319.
(35) Sakamoto, Y.; Kaneda, M.; Terasaki, O.; Zhao, D. Y.; Kim, J. M.; Stucky, G.; Shim, H. J.; Ryoo, R. *Nature* **2000**, *408*, 449-453.
(36) Chen, B. C.; Chao, M. C.; Lin, H. P.; Mou, C. Y. *Microporous and Mesoporous Materials* **2005**, *81*, 241-249.
(37) Yu, C. Z.; Tian, B. Z.; Fan, J.; Stucky, G. D.; Zhao, D. Y. *Journal of the American Chemical Society* **2002**, *124*, 4556-4557.
(38) Kim, J. M.; Kim, S. K.; Ryoo, R. *Chemical Communications* **1998**, 259-260.
(39) Kong, L. D.; Liu, S.; Yan, X. W.; Li, Q. Z.; He, H. Y. *Chemistry Letters* **2005**, *34*, 568-569.
(40) Goltner, C. G.; Henke, S.; Weissenberger, M. C.; Antonietti, M. *Angewandte Chemie-International Edition* **1998**, *37*, 613-616.
(41) Melosh, N. A.; Lipic, P.; Bates, F. S.; Wudl, F.; Stucky, G. D.; Fredrickson, G. H.; Chmelka, B. F. *Macromolecules* **1999**, *32*, 4332-4342.
(42) Melosh, N. A.; Davidson, P.; Chmelka, B. F. *Journal of the American Chemical Society* **2000**, *122*, 823-829.
(43) Yang, H. F.; Shi, Q. H.; Tian, B. Z.; Xie, S. H.; Zhang, F. Q.; Yan, Y.; Tu, B.; Zhao, D. Y. *Chemistry of Materials* **2003**, *15*, 536-541.
(44) Zhou, X. F.; Yu, C. Z.; Tang, J. W.; Yan, X. X.; Zhao, D. Y. *Microporous and Mesoporous Materials* **2005**, *79*, 283-289.
(45) El-Safy, S. A.; Hanaoka, T.; Mizukami, F. *Advanced Materials* **2005**, *17*, 47-+.
(46) El-Safty, S. A.; Hanaoka, T. *Chemistry of Materials* **2003**, *15*, 2892-2902.
(47) Lebeau, B.; Fowler, C. E.; Hall, S. R.; Mann, S. *Journal of Materials Chemistry* **1999**, *9*, 2279-2281.
(48) El Haskouri, J.; de Zarate, D. O.; Guillem, C.; Latorre, J.; Caldes, M.; Beltran, A.; Beltran, D.; Descalzo, A. B.; Rodriguez-Lopez, G.; Martinez-Manez, R.; Marcos, M. D.; Amoros, P. *Chemical Communications* **2002**, 330-331.
(49) Tanev, P. T.; Pinnavaia, T. J. *Science* **1995**, *267*, 865-867.
(50) Tanev, P. T.; Pinnavaia, T. J. *Chemistry of Materials* **1996**, *8*, 2068-2079.
(51) Israelachvili, J. N.; Mitchell, D. J.; Ninham, B. W. *Journal of the Chemical Society-Faraday Transactions Ii* **1976**, *72*, 1525-1568.
(52) Raman, N. K.; Anderson, M. T.; Brinker, C. J. *Chemistry of Materials* **1996**, *8*, 1682-1701.
(53) Sakka, S.; Kamiya, K.; Yoko, T. *Abstracts of Papers of the American Chemical Society* **1987**, *193*, 1-INOR.

(54) Sakka, S. *Nippon Kagaku Kaishi* **1988**, 243-252.
(55) Monde, T.; Kozuka, H.; Sakka, S. *Chemistry Letters* **1988**, 287-290.
(56) Lee, G. R.; Crayston, J. A. *Advanced Materials* **1993**, *5*, 434-442.
(57) Behrens, P. *Angewandte Chemie-International Edition in English* **1996**, *35*, 515-518.
(58) Schuth, F. *Chemistry of Materials* **2001**, *13*, 3184-3195.
(59) Soler-Illia, G.; Louis, A.; Sanchez, C. *Chemistry of Materials* **2002**, *14*, 750-759.
(60) Nogami, M.; Moriya, Y. *Journal of Non-Crystalline Solids* **1980**, *37*, 191-201.
(61) Sakka, S.; Kamiya, K.; Makita, K.; Yamamoto, Y. *Journal of Non-Crystalline Solids* **1984**, *63*, 223-235.
(62) Matsuzaki, K.; Arai, D.; Taneda, N.; Mukaiyama, T.; Ikemura, M. *Journal of Non-Crystalline Solids* **1989**, *112*, 437-441.
(63) HyeonLee, J.; Beaucage, G.; Pratsinis, S. E. *Chemistry of Materials* **1997**, *9*, 2400-2403.
(64) Bryans, T. R.; Brawner, V. L.; Quitevis, E. L. *Journal of Sol-Gel Science and Technology* **2000**, *17*, 211-217.
(65) Klein, L. C.; Woodman, R. H. In *Porous Ceramic Materials*, 1996; Vol. 115, pp 109-124.
(66) Ying, J. Y.; Benziger, J. B.; Navrotsky, A. *Journal of the American Ceramic Society* **1993**, *76*, 2571-2582.
(67) Schmidt, H.; Scholze, H.; Kaiser, A. *Journal of Non-Crystalline Solids* **1984**, *63*, 1-11.
(68) Brinker, C. J. *Journal of Non-Crystalline Solids* **1988**, *100*, 31-50.
(69) Ohtani, B.; Ogawa, Y.; Nishimoto, S. *Journal of Physical Chemistry B* **1997**, *101*, 3746-3752.
(70) Patsi, M. E.; Hautaniemi, J. A.; Rahiala, H. M.; Peltola, T. O.; Kangasniemi, I. M. O. *Journal of Sol-Gel Science and Technology* **1998**, *11*, 55-66.
(71) Gao, F. G.; Bard, A. J.; Kispert, L. D. *Journal of Photochemistry and Photobiology a-Chemistry* **2000**, *130*, 49-56.
(72) Hagfeldt, A.; Gratzel, M. *Accounts of Chemical Research* **2000**, *33*, 269-277.
(73) Stone, V. F.; Davis, R. J. *Chemistry of Materials* **1998**, *10*, 1468-1474.
(74) Ishino, T.; Minami, S. *Technology Reports of the Osaka University* **1953**, *3*, 357.
(75) Barringer, E. A.; Bowen, H. K. *Langmuir* **1985**, *1*, 414-420.
(76) Livage, J. *Solid State Ionics* **1988**, *26*, 144-144.
(77) Sanchez, C.; Ribot, F. *New Journal of Chemistry* **1994**, *18*, 1007-1047.
(78) Winter, G. J. *Oil Colour Chemists Association* **1953**, *36*, 689.
(79) Boyd, T. J. *Polymer Science* **1951**, *7*, 591.
(80) Yao, B. D.; Zhang, L. D. *Journal of Materials Science* **1999**, *34*, 5983-5987.
(81) Yoldas, B. E. *Journal of Non-Crystalline Solids* **1980**, *38-9*, 81-86.
(82) Lee, J. H.; Choi, S. Y.; Kim, C. E.; Kim, G. D. *Journal of Materials Science* **1997**, *32*, 3577-3585.
(83) Katagiri, Y.; Nasu, H.; Matsuoka, J.; Kamiya, K. *Journal of the American Ceramic Society* **1994**, *77*, 673-677.
(84) Martins, O.; Almeida, R. M. *Journal of Sol-Gel Science and Technology* **2000**, *19*, 651-655.
(85) Orignac, X.; Barbier, D.; Du, X. M.; Almeida, R. M.; McCarthy, O.; Yeatman, E. *Optical Materials* **1999**, *12*, 1-18.
(86) Kim, Y. S.; Yang, S. M. *Advanced Materials* **2002**, *14*, 1078-+.
(87) Yamada, T.; Zhou, H. S.; Uchida, H.; Tomita, M.; Ueno, Y.; Honma, I.; Asai, K.; Katsube, T. *Microporous and Mesoporous Materials* **2002**, *54*, 269-276.

(88) Ozkan, E.; Lee, S. H.; Liu, P.; Tracy, C. E.; Tepehan, F. Z.; Pitts, J. R.; Deb, S. K. *Solid State Ionics* **2002**, *149*, 139-146.
(89) Ogawa, M. *Journal of the American Chemical Society* **1994**, *116*, 7941-7942.
(90) Ogawa, M.; Igarashi, T.; Kuroda, K. *Bulletin of the Chemical Society of Japan* **1997**, *70*, 2833-2837.
(91) Ogawa, M.; Ishikawa, H.; Kikuchi, T. *Journal of Materials Chemistry* **1998**, *8*, 1783-1786.
(92) Anderson, M. T.; Martin, J. E.; Odinek, J. G.; Newcomer, P. In *Microporous and Macroporous Materials*, 1996; Vol. 431, pp 217-223.
(93) Martin, J. E.; Anderson, M. T.; Odinek, J.; Newcomer, P. *Langmuir* **1997**, *13*, 4133-4141.
(94) Liu, J.; Bontha, J. R.; Kim, A. Y.; Baskaran, S. In *Microporous and Macroporous Materials*, 1996; Vol. 431, pp 245-250.
(95) Baskaran, S.; Liu, J.; Domansky, K.; Kohler, N.; Li, X. H.; Coyle, C.; Fryxell, G. E.; Thevuthasan, S.; Williford, R. E. *Advanced Materials* **2000**, *12*, 291-294.
(96) Honma, I.; Zhou, H. S. *Advanced Materials* **1998**, *10*, 1532-1536.
(97) Zhou, H. S.; Kundu, D.; Honma, I. *Journal of the European Ceramic Society* **1999**, *19*, 1361-1364.
(98) Ogawa, M.; Masukawa, N. *Microporous and Mesoporous Materials* **2000**, *38*, 35-41.
(99) Honma, I.; Zhou, H. S.; Kundu, D.; Endo, A. *Advanced Materials* **2000**, *12*, 1529-1533.
(100) Besson, S.; Ricolleau, C.; Gacoin, T.; Jacquiod, C.; Boilot, J. P. *Journal of Physical Chemistry B* **2000**, *104*, 12095-12097.
(101) Li, X. S.; Fryxell, G. E.; Birnbaum, J. C.; Wang, C. M. *Langmuir* **2004**, *20*, 9095-9102.
(102) Brinker, C. J.; Lu, Y. F.; Sellinger, A.; Fan, H. Y. *Advanced Materials* **1999**, *11*, 579-585.
(103) Sellinger, A.; Weiss, P. M.; Nguyen, A.; Lu, Y. F.; Assink, R. A.; Gong, W. L.; Brinker, C. J. *Nature* **1998**, *394*, 256-260.
(104) Zhao, D. Y.; Yang, P. D.; Margolese, D. I.; Chmelka, B. F.; Stucky, G. D. *Chemical Communications* **1998**, 2499-2500.
(105) Doshi, D. A.; Gibaud, A.; Goletto, V.; Lu, M. C.; Gerung, H.; Ocko, B.; Han, S. M.; Brinker, C. J. *Journal of the American Chemical Society* **2003**, *125*, 11646-11655.
(106) Grosso, D.; Babonneau, F.; Sanchez, C.; Soler-Illia, G.; Crepaldi, E. L.; Albouy, P. A.; Amenitsch, H.; Balkenende, A. R.; Brunet-Bruneau, A. *Journal of Sol-Gel Science and Technology* **2003**, *26*, 561-565.
(107) Klotz, M.; Albouy, P. A.; Ayral, A.; Menager, C.; Grosso, D.; Van der Lee, A.; Cabuil, V.; Babonneau, F.; Guizard, C. *Chemistry of Materials* **2000**, *12*, 1721-1728.
(108) Klotz, M.; Ayral, A.; Guizard, C.; Cot, L. *Journal of Materials Chemistry* **2000**, *10*, 663-669.
(109) Grosso, D.; Balkenende, A. R.; Albouy, P. A.; Lavergne, M.; Mazerolles, L.; Babonneau, F. *Journal of Materials Chemistry* **2000**, *10*, 2085-2089.
(110) Grosso, D.; Babonneau, F.; Albouy, P. A.; Amenitsch, H.; Balkenende, A. R.; Brunet-Bruneau, A.; Rivory, J. *Chemistry of Materials* **2002**, *14*, 931-939.
(111) Lu, Y. F.; Ganguli, R.; Drewien, C. A.; Anderson, M. T.; Brinker, C. J.; Gong, W. L.; Guo, Y. X.; Soyez, H.; Dunn, B.; Huang, M. H.; Zink, J. I. *Nature* **1997**, *389*, 364-368.
(112) Bagshaw, S. A.; Prouzet, E.; Pinnavaia, T. J. *Science* **1995**, *269*, 1242-1244.

(113) Ferrer, M.; Lianos, P. *Langmuir* **1996**, *12*, 5620-5624.
(114) Huang, M. H.; Dunn, B. S.; Soyez, H.; Zink, J. I. *Langmuir* **1998**, *14*, 7331-7333.
(115) Grosso, D.; Soler-Illia, G.; Babonneau, F.; Sanchez, C.; Albouy, P. A.; Brunet-Bruneau, A.; Balkenende, A. R. *Advanced Materials* **2001**, *13*, 1085-1090.
(116) Hwang, Y. K.; Lee, K. C.; Kwon, Y. U. *Chemical Communications* **2001**, 1738-1739.
(117) Crepaldi, E. L.; Soler-Illia, G.; Grosso, D.; Cagnol, F.; Ribot, F.; Sanchez, C. *Journal of the American Chemical Society* **2003**, *125*, 9770-9786.
(118) Angelome, P. C.; Aldabe-Bilmes, S.; Calvo, M. E.; Crepaldi, E. L.; Grosso, D.; Sanchez, C.; Soler-Illia, G. *New Journal of Chemistry* **2005**, *29*, 59-63.
(119) Attard, G. S.; Glyde, J. C.; Goltner, C. G. *Nature* **1995**, *378*, 366-368.
(120) Ryoo, R.; Ko, C. H.; Cho, S. J.; Kim, J. M. *Journal of Physical Chemistry B* **1997**, *101*, 10610-10613.
(121) Templin, M.; Franck, A.; DuChesne, A.; Leist, H.; Zhang, Y. M.; Ulrich, R.; Schadler, V.; Wiesner, U. *Science* **1997**, *278*, 1795-1798.
(122) Zhao, D. Y.; Yang, P. D.; Chmelka, B. F.; Stucky, G. D. *Chemistry of Materials* **1999**, *11*, 1174-1178.
(123) Miyata, H.; Kuroda, K. *Chemistry of Materials* **2000**, *12*, 49-54.
(124) Yang, H.; Kuperman, A.; Coombs, N.; MamicheAfara, S.; Ozin, G. A. *Nature* **1996**, *379*, 703-705.
(125) Aksay, I. A.; Trau, M.; Manne, S.; Honma, I.; Yao, N.; Zhou, L.; Fenter, P.; Eisenberger, P. M.; Gruner, S. M. *Science* **1996**, *273*, 892-898.
(126) Yang, H.; Coombs, N.; Sokolov, I.; Ozin, G. A. *Journal of Materials Chemistry* **1997**, *7*, 1285-1290.
(127) Yang, H.; Coombs, N.; Ozin, G. A. *Advanced Materials* **1997**, *9*, 811-&.
(128) Hillhouse, H. W.; Okubo, T.; vanEgmond, J. W.; Tsapatsis, M. *Chemistry of Materials* **1997**, *9*, 1505-&.
(129) Hillhouse, H. W.; van Egmond, J. W.; Tsapatsis, M.; Hanson, J. C.; Larese, J. Z. *Chemistry of Materials* **2000**, *12*, 2888-2893.
(130) Miyata, H.; Kuroda, K. *Journal of the American Chemical Society* **1999**, *121*, 7618-7624.
(131) Holt, S. A.; Reynolds, P. A.; White, J. W. *Physical Chemistry Chemical Physics* **2000**, *2*, 5667-5671.
(132) Holt, S. A.; Edler, K. J.; Fernandez-Martin, C. In *Surface and Colloid Science*, 2004; Vol. 128, pp 169-174.
(133) Hillhouse, H. W.; van Egmond, J. W.; Tsapatsis, M. *Langmuir* **1999**, *15*, 4544-4550.
(134) Schacht, S.; Huo, Q.; VoigtMartin, I. G.; Stucky, G. D.; Schuth, F. *Science* **1996**, *273*, 768-771.
(135) Huo, Q. S.; Zhao, D. Y.; Feng, J. L.; Weston, K.; Buratto, S. K.; Stucky, G. D.; Schacht, S.; Schuth, F. *Advanced Materials* **1997**, *9*, 974-&.
(136) Adachi, M. *Colloid and Polymer Science* **2003**, *281*, 370-385.
(137) Adachi, M.; Murata, Y.; Sago, K.; Nakagawa, K. *Langmuir* **2004**, *20*, 5965-5968.
(138) Yang, H.; Coombs, N.; Sokolov, I.; Ozin, G. A. *Nature* **1996**, *381*, 589-592.
(139) Yang, H.; Coombs, N.; Ozin, G. A. *Journal of Materials Chemistry* **1998**, *8*, 1205-1211.
(140) Brennan, T.; Hughes, A. V.; Roser, S. J.; Mann, S.; Edler, K. J. *Langmuir* **2002**, *18*, 9838-9844.
(141) Holt, S. A.; Foran, G. J.; White, J. W. *Langmuir* **1999**, *15*, 2540-2542.
(142) Ruggles, J. L.; Holt, S. A.; Reynolds, P. A.; Brown, A. S.; Creagh, D. C.; White, J. W. *Physical Chemistry Chemical Physics* **1999**, *1*, 323-328.

(143) Huo, Q. S.; Margolese, D. I.; Stucky, G. D. *Chemistry of Materials* **1996**, *8*, 1147-1160.
(144) Tolbert, S. H.; Schaffer, T. E.; Feng, J. L.; Hansma, P. K.; Stucky, G. D. *Chemistry of Materials* **1997**, *9*, 1962-1967.
(145) Brown, A. S.; Holt, S. A.; Dam, T.; Trau, M.; White, J. W. *Langmuir* **1997**, *13*, 6363-6365.
(146) Brown, A. S.; Holt, S. A.; Reynolds, P. A.; Penfold, J.; White, J. W. *Langmuir* **1998**, *14*, 5532-5538.
(147) Brennan, T.; Roser, S. J.; Mann, S.; Edler, K. J. *Langmuir* **2003**, *19*, 2639-2642.
(148) Edler, K. J.; Brennan, T.; Roser, S. J.; Mann, S.; Richardson, R. M. *Microporous and Mesoporous Materials* **2003**, *62*, 165-175.
(149) Fernandez-Martin, C.; Edler, K. J.; Roser, S. J. *Langmuir* **2004**, *20*, 10679-10684.
(150) Brennan, T.; Roser, S. J.; Mann, S.; Edler, K. J. *Chemistry of Materials* **2002**, *14*, 4292-4299.
(151) Edler, K. J.; Goldar, A.; Hughes, A. V.; Roser, S. J.; Mann, S. *Microporous and Mesoporous Materials* **2001**, *44*, 661-670.
(152) Edler, K. J.; Roser, S. J.; Mann, S. *Chemical Communications* **2000**, 773-774.
(153) Kipkemboi, P.; Fogden, A.; Alfredsson, V.; Flodstrom, K. *Langmuir* **2001**, *17*, 5398-5402.
(154) Flodstrom, K.; Alfredsson, V. *Microporous and Mesoporous Materials* **2003**, *59*, 167-176.
(155) Ruggles, J. L.; Holt, S. A.; Reynolds, P. A.; White, J. W. *Langmuir* **2000**, *16*, 4613-4619.
(156) Fernandez-Martin, C.; Edler, K. J.; Roser, S. J. **(in preparation)**.

Chapter 2 Mesoporous Silica and Titania Thin Films

2.1 Synthesis of Silica and Titania Thin Films

Mesophase surfactant-templated silica and titania thin films grow spontaneously at the surface of a dilute acidic solution. Films are synthesized using self-assembled arrays of surfactant molecules, where the hydrophilic part is oriented towards the bulk water and the hydrophobic part positioned in order to avoid the water. Addition of inorganic species promotes formation of an inorganic-organic mesophase by polymerisation of the inorganic, incorporating the micellar assembly and forming the thin film at the air- liquid interface (see Figure 2.1).

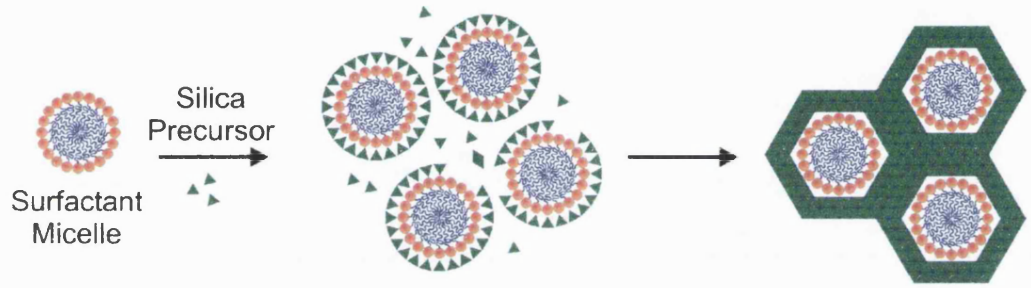

Figure 2.1. Schematic of the formation of the surfactant-templated silica thin film.

2.1.1 Standard experimental procedure for surfactant-templated silica thin films

To obtain surfactant-templated silicate thin films at the air-water interface an acidic solution with HCl in water is required. The surfactant is added into the acidic solution at room temperature. The reactant proportion in the mixture depends on what kind of surfactant or inorganic precursor is used. Therefore the molar ratios necessary to grow the thin films are defined for every experiment in the following chapters. Finally the silicate precursor is added and the solution is shaken until clear for a few seconds. The final mixture is poured into a Teflon trough with a surface area of $\approx 63 cm^2$ and several millimetres deep until a raised meniscus is reached, (see Figure 2.2). The solution is left for a certain time at ambient temperature until the film is formed. After that the film is collected by touching a microscope slide to the film surface causing the

film to become attached to the slide. The precipitated bulk is separated and dried to afterwards obtain powder, which can be analysed in techniques such as XRD, SAXS or SANS.

The surfactants used in this thesis are: cetyltrimethylammonium bromide (CTAB, Sigma 99%), octa-ethylene glycol mono n-hexadecyl ether ($C_{16}EO_8$, BC-8SY, Nikko Chemicals, Japan). Tetramethoxysilane (TMOS, Acros 98 %) was used as the silica precursor. Hydrochloric acid (HCl, Aldrich 37% w/w) was used to prepare solutions at pH < 2. HCl with Milli-Q purified water (18 MΩ).

Table 2.1. Standard concentration to prepare surfactant-templated silica thin films.

Reactants	M (mol/l)
Surfactant	0.075
Alkoxysilane	0.54
HCl (10M) in water	0.2

Deuterium oxide (D_2O 99.9%) supplied by Aldrich was used for mesoporous silica thin films during small angle neutron scattering (SANS) experiments.

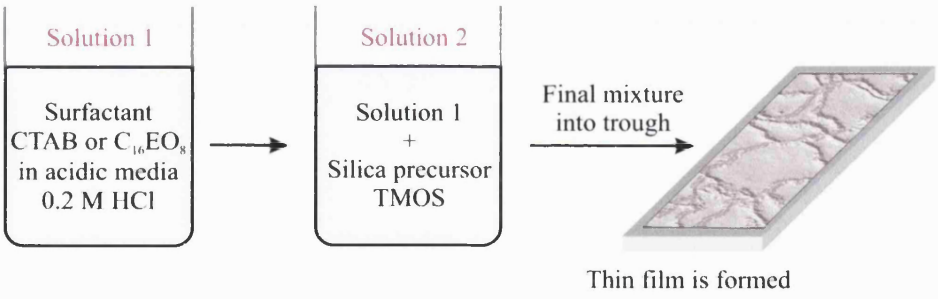

Figure 2.2. Schematic of the mesoporous silica thin films preparation

2.1.2 Standard experimental procedure for templated-surfactant titania thin films

The standard preparation of these films is based on the recipe published by Henderson *et al.*[1]

The preparation method to obtain the mesoporous titania thin films at the air-liquid interface requires the preparation of two solutions as Figure 2.3 illustrates. The first solution consists of adding either an anionic or a non-ionic surfactant into pure water. Titanium (IV) butoxide (TBOT), which acts as a precursor, is added to a specific

volume of 10 M HCl forming the second solution which is stirred until any precipitate is dissolved and allowed to cool to room temperature. This second mixture gives a clear solution that is yellow in some cases and colourless in others, depending on the TBOT concentration.[1] Afterwards both solution are mixed and poured into the Teflon trough.

For these specific films the surfactants used during this thesis are: Sodium dodecyl sulphate (SDS, Acros) and Polyoxyethylene 10 cetyl ether (Brij56®, Aldrich). Titanium (IV) butoxide ($Ti(OR^n)_4$, Aldrich 97%) was used as titania precursor.

Table 2.2. Standard concentration to prepare surfactant-templated titania thin films.

Reactants	M (mol/l)
Surfactant	0.014
Titanium alkoxide	0.087
HCl (10M) in water	1.46

Deuterium oxide (D_2O, Aldrich 99.9%) was also used for mesoporous titania thin films during SANS experiments.

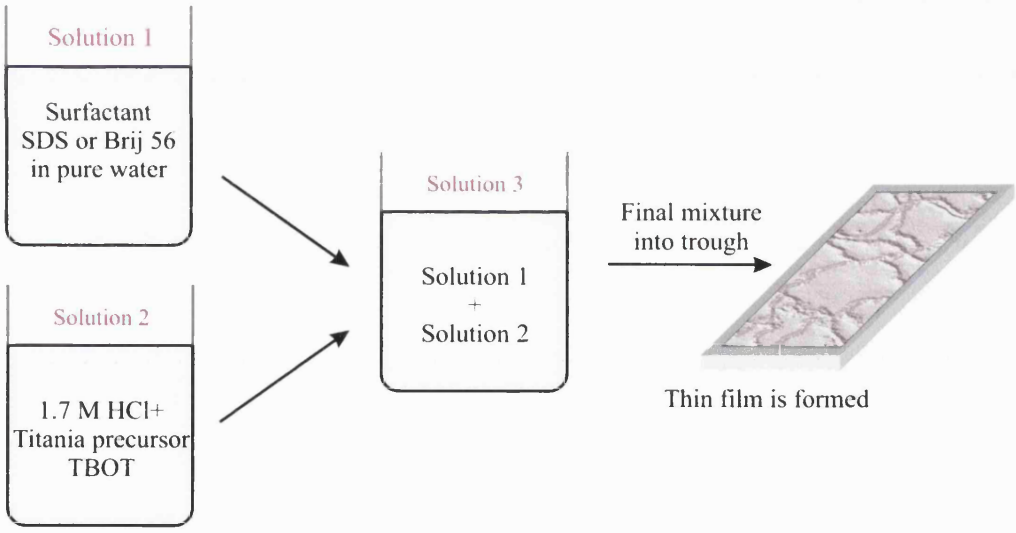

Figure 2.3. Schematic of the mesoporous titania thin films preparation

2.2 Growth Stages or Formation Periods

The growth of mesostructured silica thin films at the air-water interface occurs in three stages[2]:

2.2.1 Induction Period

During this period nothing appears to happen at the surface of the mixed solution. It is characterised by the lack of solid domains, which can be viewed using the Brewster angle microscopy.

2.2.2 Mesostructure development period or film development stage

In this stage the film starts to grow covering partially the interface.

2.2.3 Surface-coarsening period or surface-consolidation stage

It is the period in which the film consolidates covering most of the surface and becoming more homogeneous. In the case of silica thin films using as surfactant CTAB the film becomes increasingly rough, unlike films observed for non-ionic surfactants.

Thin film stages are studied in more detail along the thesis for different experiments using X-ray reflectivity and Brewster angle microscopy. However a characteristic representation of these three stages can be observed in the next images (see Figure 2.4) obtained by Brewster angle microscopy:

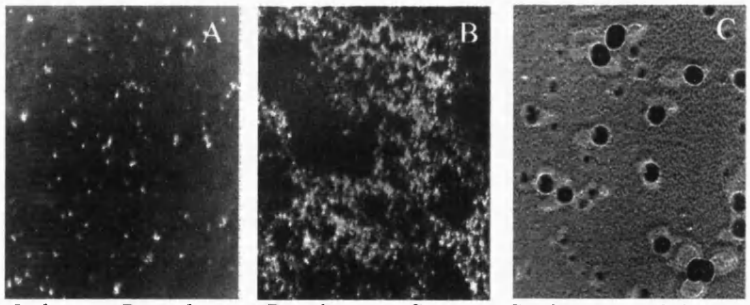

Induction Period *Development Stage* *Surface-consolidation Stage*

Figure 2.4. Example of BAM images of the mixed surfactant-templated mesoporous silica film. Brij56® and CTAB have been used as the surfactant mixture and TMOS as the silica precursor in an acidic solution following these molar ratios: 0.23 Brij56®/ 0.76 CTAB: 3.6 $\times 10^{-3}$ HCl: 1 water: 1.07 $\times 10^{-2}$ TMOS. The pictures were taken: A) 108 min, B) 326 min, and C) 350 min after mixing.

2.3 Mechanisms

A full understanding of the formation mechanisms in the self-assembling system of surfactant-templated mesoporous silica thin films is yet to be achieved. However, Edler *et al.* investigated the concentration dependence of the self-assembly process observed during the formation of the thin films using CTAB as the surfactant and TMOS as the silica precursor.[2, 3] The development of the solution towards the final film formation was studied using the off specular X-ray reflectivity technique (explained in more detail in Chapter 3). The observed behavior of the intensity of the specular peak and of the peak width for the different diffraction peaks was the evidence to determine the possible existence of two distinguishable mechanisms. Consequently two self-assembly regimes were suggested in the formation of these films the surface-driven and the bulk-driven mechanisms. These mechanisms are studied in more detail in further chapters looking at different systems; CTAB/ TMOS system with variation in temperature and humidity,[4] and $C_{16}EO_8$/ TMOS system[5] using X-ray reflectivity and Brewster angle microscopy techniques.

A brief description of these mechanisms is given next.

2.3.1 Bulk-driven Mechanism

This mechanism takes place when micelles aggregate forming particles with a large domain size in the bulk solution. These particles diffuse to the surface where they pack to form the film.[2, 3, 6]

2.3.2 Surface-driven Mechanism

The film nucleates at the air-water interface by addition of single silica coated micelles and grows downward into the solution.[2, 3]

2.4 References

(1) Henderson, M. J.; King, D.; White, J. W. *Australian Journal of Chemistry* **2003**, *56*, 933-939.

(2) Edler, K. J.; Brennan, T.; Roser, S. J.; Mann, S.; Richardson, R. M. *Microporous and Mesoporous Materials* **2003**, *62*, 165-175.

(3) Brennan, T.; Hughes, A. V.; Roser, S. J.; Mann, S.; Edler, K. J. *Langmuir* **2002**, *18*, 9838-9844.

(4) Fernandez-Martin, C.; Edler, K. J.; Roser, S. J. *Langmuir* **2004**, *20*, 10679-10684.

(5) Fernandez-Martin, C.; Edler, K. J.; Roser, S. J. **(in preparation)**.

(6) Edler, K. J.; Goldar, A.; Hughes, A. V.; Roser, S. J.; Mann, S. *Microporous and Mesoporous Materials* **2001**, *44*, 661-670.

Chapter 3 Methods of Characterization of Mesoporous Thin Films

To provide structural and chemical information about surfactant-templated thin films several techniques with different sources, such as neutrons, X-rays, electrons, photons are required. For a better understanding about neutron and X-ray techniques, some fundamental differences between both sources are briefly described.

3.1 X-rays and Neutrons

3.1.1 Differences and Similarities

The most fundamental difference between neutron and electromagnetic radiation is the interaction with matter.

When an X-ray beam collides with an atom, the beam only interacts with the electrons. The more electrons the atom contains, the stronger the intensity of the interaction is. Atoms with small atomic number (Z), such as hydrogen, practically do not "feel" the X-rays. This indicates that the elastic X-ray scattering is proportional to the Z^2. When a neutron collides with an atom, due to its electronic neutrality, it does not interact with the electrons. Neutrons can penetrate easily inside the atom, crossing the electronic cloud and reaching the nucleus.

The amount by which atoms scatter neutrons, called the neutron cross section (σ), varies randomly with Z, whereas for X-rays it increases steadily (see Figure 3.1). Therefore the cross section depends on nuclear properties, not on Z^2. This means that neutrons are useful for studying light atoms, materials with different isotopes and samples that contain elements of similar atomic mass as these can have very different neutron cross sections.

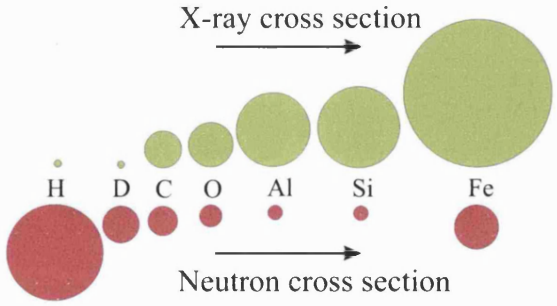

Figure 3.1. Variation of the X-ray and neutron cross-section as the Z increases (after NIST 2003 annual report [1])

The most significant isotopic variation occurs when Z = 1. Hydrogen has a coherent cross section (σ_{coh}) of 1.75×10^{-24} cm^2 (or 1.75 barns) and for deuterium σ_{coh} = 5.6 barns. Neutrons not only can "see" hydrogen and deuterium but also distinguish between the two of them. Hydrogen has the advantage that its scattering length (b) is negative; hence it gives more contrast to other atoms. It has the disadvantage that the incoherent cross section (σ_{inc}), responsible for the undesirable background, is very large. Therefore it is often convenient to deuterate the sample (see Table 3.1).[2,3]

Table 3.1. Neutron scattering cross-sections (σ), and neutron scattering lengths (b) values for several atomic nucleus.

Atomic Nucleus	b_{coh} (fm)	σ_{coh} (barns)	σ_{inc} (barns)	σ_{abs} (barns)
^{1}H	- 3.741	1.8	80.3	0.3
^{2}D	6.671	5.6	2.1	0.0
C	6.646	5.6	0.0	0.0
N	9.362	11.0	0.5	1.9
O	5.803	4.2	0.0	0.0
Na	3.580	1.6	1.7	0.5
Si	4.153	2.2	0.0	0.2
Cl	9.577	11.5	5.3	33.5
Ti	- 3.438	1.5	2.9	6.1
Br	6.795	5.8	0.1	6.9

Hence, neutrons provide the advantage that isotopic substitution can be used to achieve large contrasts in the *scattering length density*, explained further on in this section. The interaction of neutrons with matter is weak and the absorption of neutrons by most materials is correspondingly small. Neutron radiation is therefore very penetrating, providing less resolution. This can be translated as neutrons require more time and the data collection, therefore, is slower. Neutrons, on the other hand, can be used to probe the bulk properties of samples with pathlengths of several centimetres.

Among the similarities X-rays and neutrons can be polarised, give rise to birefringence, have optical activity and demonstrate the concept of refractive indices. The neutron refractive index, n, of any material is a function of the scattering length density, Nb, and the neutron wavelength, λ:

$$n \approx (1 - \frac{\lambda^2 N_b}{2\pi}) \qquad 3\text{-}1$$

Optical refractive indices are, typically, greater than unity while neutron refractive indices are smaller than one. This difference allows neutrons to be totally externally reflected from a surface. In addition neutron refractive index depends not only on the number of nuclei but also on how strongly they scatter. To explain this connection the parameter known as the scattering length density, *Nb* that indicates a nucleus' ability to scatter neutrons is defined as

$$N_b = b_j n_j \qquad 3\text{-}2$$

where n_j is the number of nuclei per unit volume and b_j is the scattering length of nucleus j.[4-7]

3.1.2 X-rays Sources: Synchrotron Radiation

When high energy electrons are deflected by strong magnetic fields, they emit electro-magnetic waves called *synchrotron radiation.* Covering the whole spectral range from microwaves to hard X-rays, the light produced by a storage ring comes in the form of a fine and very intense beam, similar to that from a laser.

There are about 50 synchrotrons in the world. The three largest and most powerful are the Advance Photon Source (APS) in Illinois, USA; the Spring-8 in Nishi Harima, Japan; and the European Synchrotron Radiation Facility (ESRF) in Grenoble, France. In particular, the ESRF is a third generation synchrotron source optimized to emit hard X-rays that are a trillion (10^{12}) times more brilliant than those produced by X-ray tubes with energy range from 1 up to hundreds keV. The majority of the beamlines use an insertion device (ID) as a source point, which generates high fluxes and brilliance in the 2 to 40 keV range of photon energy. 26 IDs have been installed, nearly all made of permanent magnet material with magnet blocks placed in the air outside the vacuum chamber of the electron beam.[8-10]

In this thesis X-ray reflectivity and grazing X-ray diffraction (GIXD) experiments were carried out at the ESRF on the ID10B beamline.

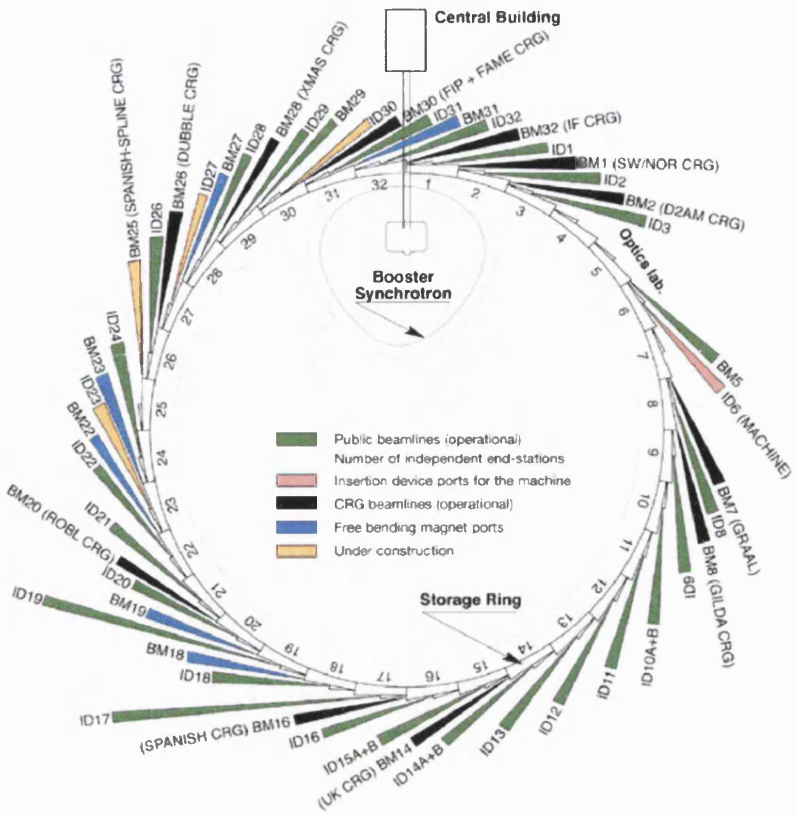

Figure 3.2. Scheme showing the layout of the beamlines on the European Synchrotron Radiation Facility (ESRF) in Grenoble, France.[11]

3.1.3 Neutron sources

There are two means of producing neutrons in sufficient quantities for worthwhile experiments. One is the nuclear reactor where neutrons are released by the fission of uranium-235. Each fission event releases 2-3 neutrons, though one of these is needed to sustain the chain reaction. The most powerful of the reactor neutron sources in the world today is the 57 MW HFR (High-Flux Reactor) at the Institute Max von Laue - Paul Langevin (ILL) in Grenoble, France.[12]

The other approach to neutron production is that used in *spallation* neutron sources. The most powerful spallation neutron source in the world is ISIS in Oxford, UK. ISIS produces neutrons by bombarding a tantalum target with protons (travelling at 84% of the speed of light) from a particle accelerator. Each high-energy proton releases from the target approximately 15 neutrons in pulses at 50 Hz. Neutrons, on a pulsed source as at ISIS, are detected according to their speed. They arrive at the detector at different

times with different wavelength and scatter through the same angle acquiring different Q-values. This way of measuring is called "time-of- flight" unlike reactor-based neutron diffraction instruments, which work with a fixed wavelength.[7]

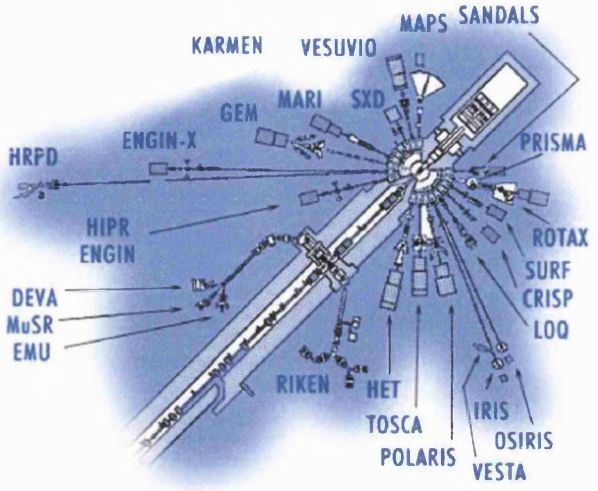

Figure 3.3. Scheme showing the layout of the instruments on the ISIS pulsed neutron facility.[13]

3.2 Fundamentals of Crystallography

Before starting with the techniques overviews some of the fundamentals of crystallography, crucial in this thesis, are briefly explained here.

In general the number of Bragg reflections d_{hkl} observed in reflectivity profiles or GIXD patterns depend on the symmetry of the lattice and which are related to the Miller indices (hkl). The values of the interplanar spacing (d_{hkl}) associated with the hexagonal and cubic crystal systems, relevant for this thesis, can be written as

$$\text{Cubic}: \quad \frac{1}{d_{hkl}} = \left[\frac{1}{a^2}\left(h^2 + k^2 + l^2\right)\right]^{1/2} \qquad 3\text{-}3$$

$$\text{3 - D Hexagonal}: \quad \frac{1}{d_{hkl}} = \left[\frac{4}{3a^2}\left(h^2 + hk + k^2\right) + \frac{l^2}{c^2}\right]^{1/2} \qquad 3\text{-}4$$

$$\text{2 - D Hexagonal}: \quad \frac{1}{d_{hkl}} = \frac{2}{a\sqrt{3}}\left(h^2 + hk + k^2\right)^{1/2} \qquad 3\text{-}5$$

In these equations a, b and c are the lattice parameters that define the unit cell.

- Cubic: $a = b = c$ with $\alpha = \beta = \gamma = 90°$
- Hexagonal: $a = b \neq c$ with $\alpha = \beta = 90°$ and $\gamma = 120°$

Some typical ratios of Q values relative to the fundamental reflection at Q^* are given for various symmetries in Table 3.2.

Table 3.2. Ratios Q/Q^* for the Bragg reflections from different structures.

Structure	Ratio Q/Q^*
Lamellar	1: 2: 3: 4: 5: 6...
Hexagonal	1: √3: 2=√4: √7: 3=√9: √11.....
Cubic bcc	1: √2: √3: 2=√4: √5: √6.....
Cubic fcc	1: √(4/3): √(8/3): √(11/3): 2=√(12/3): √(16/3)...

3.3 Interface Study Techniques

3.3.1 Reflectivity

Surfaces and interfaces can be studied by X-ray or neutron reflection. These techniques explore the variation in composition normal to the reflecting surface. X-rays, for example, pass from a medium of a given refractive index to another of different refractive index. Reflection or transmission can occur depending on the wavelength of the radiation, angle of incidence θ_i, and refractive indices of the media (n).[14] The refractive index is defined as the speed of light (c) in vacuum divided by the speed of light in the medium (v):

$$n = \frac{c}{v} \qquad 3\text{-}6$$

Snell's Law, which defines the indices of refraction n of the two media to the directions of propagation relative to the angles to the normal (incident θ_i, and transmitted θ_t angles), is defined as:

$$\frac{\sin\theta_i}{\sin\theta_t} = \frac{n_2}{n_1} \qquad 3\text{-}7$$

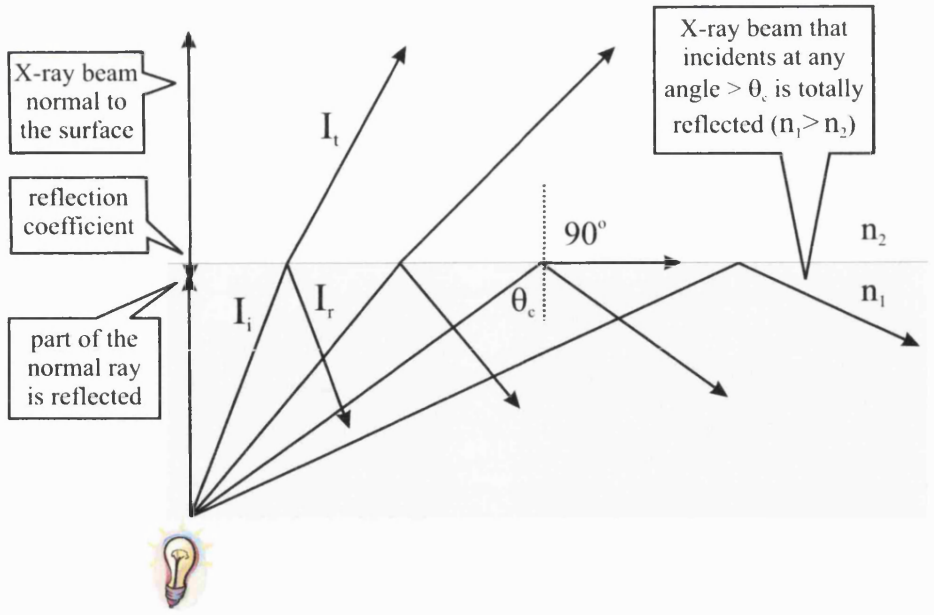

Figure 3.4. Reflection and transmission of an X-ray beam at different incident angles.[15]

For X-rays, i.e. electromagnetic radiation with a wavelength λ around 1 Å, the refractive index is:[16-19]

$$n = 1 - \delta + i\beta \qquad 3\text{-}8$$

where δ represents the ability of the material to scatter the X-ray and β is the absorption coefficient.

$$\delta = \frac{\lambda^2}{2\pi} r_e \rho_e \quad \text{and} \quad \beta = \frac{\lambda}{4\pi} \mu_x . \qquad 3\text{-}9$$

The parameter $r_e = 2.818 \times 10^{-15}$ m. is the electron radius, ρ_e is the electron density of the material, and μ_x is the absorption length.

In the case of neutrons δ depends on the scattering length b of the nuclei, which varies randomly across the periodic table, as mentioned in section 3.1.1.

$$\delta = \frac{\lambda^2}{2\pi} b \rho_n \quad \text{and} \quad \beta = \frac{\lambda}{4\pi} \mu_n \qquad 3\text{-}10$$

For X-rays $\delta > 0$ and β is usually much smaller than δ, which is ignored for convenience, the refractive index is less than that of the air, $n_2 < 1$ (see Figure 3.4). Therefore total reflection occurs for incident angles θ_i above the critical angle, θ_c. It is shown by Snell's Law that:

$$\theta_c = \arcsin\left(\frac{n_2}{n_1}\right) \qquad 3\text{-}11$$

The reflectivity profile can be calculated from the reflection coefficient as $R = |r|^2$, which describes the amplitude of a reflected wave relative to an incident wave. Incident radiation is the result of the superposition of two plane-polarized beams, one parallel to the plane of incidence (p-polarized) and the other perpendicular to the plane of incidence (s-polarized). Fresnel's laws[20] can be summarized in the following two equations, which give the reflectance of the s- and p-polarized components:

$$r_s = \left[\frac{\sin(\theta_1 - \theta_2)}{\sin(\theta_1 + \theta_2)}\right]^2 \qquad r_p = \left[\frac{\tan(\theta_1 - \theta_2)}{\tan(\theta_1 + \theta_2)}\right]^2 \qquad 3\text{-}12$$

The Fresnel's law calculates the reflectivity assuming an optically flat interface. Reflectivity from complex interfaces such as rough surfaces may be calculated using either a recursion algorithm[21] or an optical matrix method.[20, 22]

In the study of surfactant-templated silica and titania thin films at air-liquid interface, X-ray reflectivity gives information about the structure of the interface along the surface normal direction, providing information about the film structure and also about growth mechanism, interfacial roughness, the surface coverage of the film etc. To achieve this information two reflectivity measurement modes, specular and off specular were used.

3.3.1.1 Specular X-ray Reflectivity

Specular reflectivity occurs when the angle of the incident beam is equal to the angle of the reflected beam; $\theta_i = \theta_r$ as Figure 3.5 shows.

Considering the specular part the reflectivity is defined as the ratio of the incident and reflected intensities for each θ,

$$R(\theta, \lambda) = \frac{I_r}{I_i}(\lambda) \qquad 3\text{-}13$$

The reflectivity is calculated as a function of the wave vector perpendicular to the reflecting surface called momentum transfer (Q). The momentum transfer conventionally used in reflectivity plots, is obtained by Bragg's law:

$$n\lambda = 2d \sin\theta \qquad 3\text{-}14$$

$$Q = \left(\frac{4\pi}{\lambda}\right) \sin\theta \qquad 3\text{-}15$$

The momentum transfer, consequently, is directly proportional to the reflection angle, θ, and inversely proportional to the wavelength, λ, and to the interplane distance or d-spacing as the next expression describes:

$$Q = \frac{2\pi}{d} \qquad 3\text{-}16$$

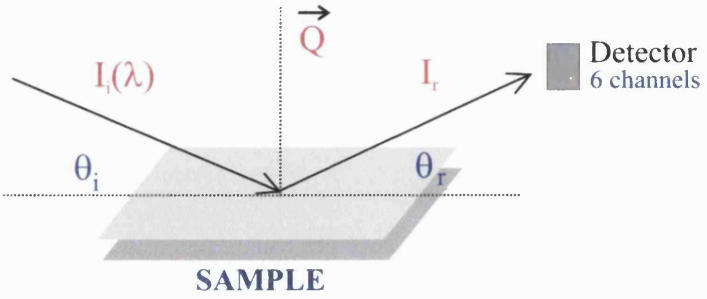

Figure 3.5. Representation of specular X-ray reflectivity.

An example of specular X-ray reflectivity profile is shown in Fig. 3.6. The intensity of the critical angle in reflectivity, from a bulk interface, is unity and for $Q > Q_c$ it decays sharply as $R \sim Q^{-4}$. The presence of peaks in the reflectivity profile is a sign of a well-ordered structure. The peak intensity and its position in Q provide information about the roughness, and number of layers within the film.

The formation of these layers are associated with different densities and thickness which can correspond either to the hydrocarbon tails of the surfactants in the interior of the micelles or surfactant headgroups bonding with the inorganic precursor.

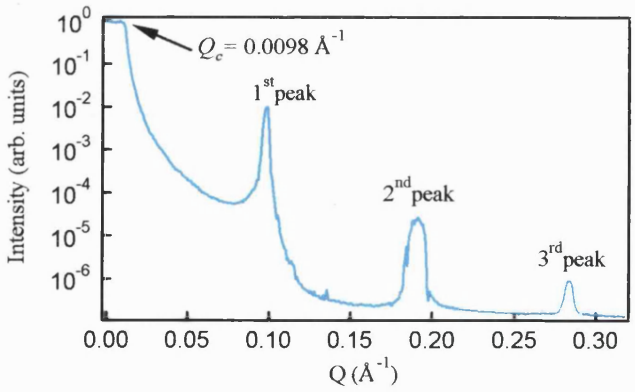

Figure 3.6. Example of a specular X-ray reflectivity profile.

3.3.1.2 *Off-specular X-ray Reflectivity*

Measurements in the specular mode take 1 hour for the angle range shown in Figure 3.6 since both arms move, resulting a slower technique. Therefore specular reflectivity is not used for studying the thin film growth progress with time. However in off specular none of the arms in the reflectometer; detector or source, move so the data collection is every 60 seconds. The off specular scattering is relatively weak compared to the specular reflectivity, requiring the intensity available at a synchrotron facility for X-rays to obtain fast, time-resolved data.

Off-specular reflectivity occurs when the incident angle is different to the reflected angle $\theta_i \neq \theta_r$. Depending on the angle chosen, the linear detector is able to collect different peaks at different channel positions, which afterwards are transformed into Q (Å^{-1}) (see Figure 3.7).

In the case of off-specular X-ray reflectivity measurements[23] a linear position sensitive detector is aligned in the vertical direction, perpendicular to the sample plane, and to the incident angle (θ_i) as Figure 3.7 shows. In this geometry not only the specularly reflected beam is seen, but also diffuse scattering at angles other than the specular ($\theta_i \neq \theta_r$).

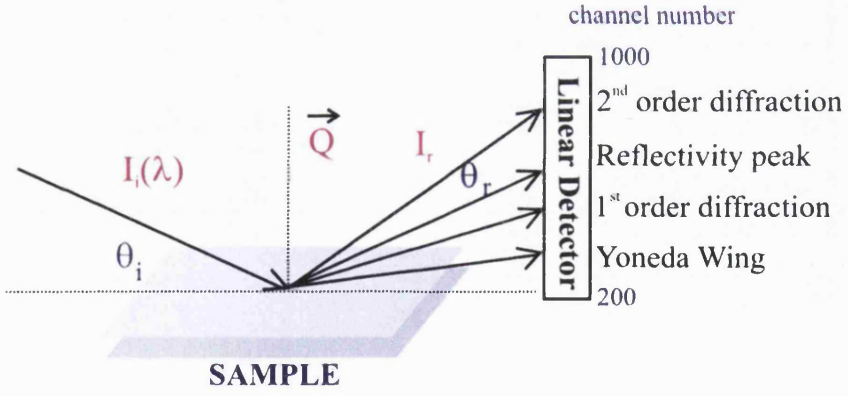

Figure 3.7. Representation of the off-specular X-ray reflectivity showing the characteristic peak positions in the linear detector.

Variation of the peak intensities with time can be followed indicating how the surface structure changes as the film grows. The incident angle θ_i is chosen so that the first and the second orders of diffraction appear on either side of the specularly reflected beam.

The most characteristic peaks in off specular reflectivity, shown in Figure 3.8, are described as follows:

- *The Yoneda Wing*, which is a doubling of intensity at the critical angle of the surface, which is related to mesoscale surface roughness.
- *Specular reflectivity peak*, which is due to the specular reflectance and occurs when the incident angle and the scattered angle are equal.
- *Diffraction peaks*, which shows the mesostructural definition of the thin film.

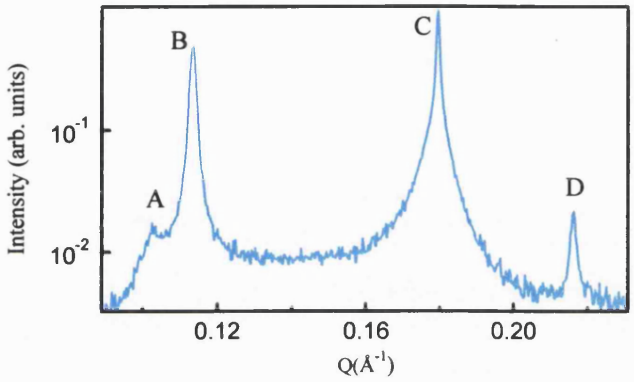

Figure 3.8. Example of an off specular X-ray reflectivity profile. The peaks are defined as: Yoneda wing (A); first diffraction peak (B); specular reflectivity peak (C); second diffraction peak (D);

In the following chapters the study of the formation mechanism for the thin film growth will consider the full width half-maximum (FWHM) of the diffraction peaks. Thus it is important to cite the Scherrer formula, which relates the FWHM with domain size being inversely proportional with each other:

$$t = (K\lambda)/(\beta\cos\theta) \qquad 3\text{-}17$$

where t is the domain size, K is the Scherrer's constant (from 0.89 to 1.0), β is the FWHM, and θ is the diffraction angle.[24] The number of repeat units can be calculated from the domain size:

$$n = t/d\ spacing \qquad 3\text{-}18$$

3.3.2 *Grazing Incidence X-ray Diffraction (GIXD)*

In mesoporous silica thin films micelles are expected to pack and align themselves in a specific and preferred orientation at air-liquid interface. With such ordering only lattice planes parallel to the surface can be detected by reflectivity. To obtain information on the in-plane periodic lattice in the film, the grazing incidence x-ray diffraction (GIXD) technique is employed.[25, 26]

Unlike specular and off specular X-ray reflectivity, GIXD records data in the XY plane, rotating the detector through the angle δ (see Figure 3.9). GIXD is an ideal in-plane structural probe (Q_{xy}) of surfaces and interfaces, combining the power of conventional X-ray diffraction (XRD) for determining bulk structure with refraction effects. [27]

In this technique the incident angle of X-ray (θ_i) is set at a very small angle, usually close to the critical angle ($\theta_i \approx \theta_c$) and the incident beam will be reflected $90^\circ - \theta_i$ with the normal to the surface in a specular geometry. For $\theta_i > \theta_c$, we get a diffraction pattern from the bulk of the film. The d-spacing of periodicities normal to the surface can be obtained from in-plane XRD by $n\lambda = 2d\sin(\delta/2)$ (Bragg's law).

2D GIXD patterns provide structural information about both out-of-plane and in-plane lattices, as well as periodicities that are neither normal nor parallel to the film.[26]

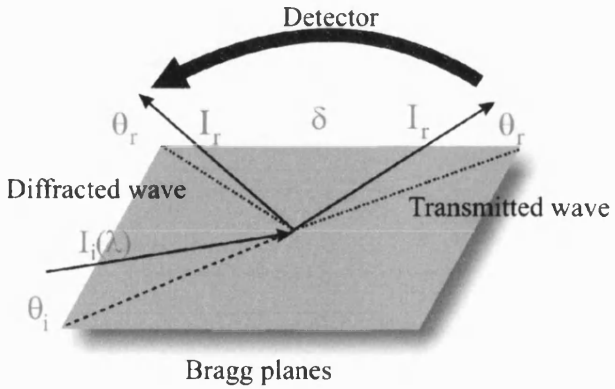

Figure 3.9. Geometrical representation of the GIXD.

An example of diffraction patterns produced by lamellar and 2D hexagonal phases are shown below. The lamellar phase consists of a series of two-dimensional sheets layered on top of each other. When they are highly ordered the pattern displays diffraction spots. For more random orientations or micellar transitions leading towards hexagonal or cubic mesophases[28] powder-like diffraction rings are shown.

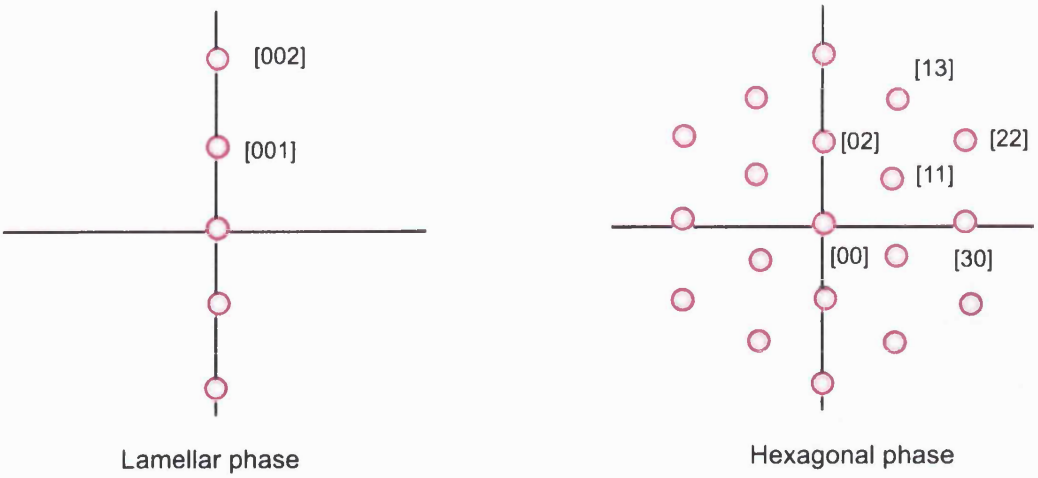

Grazing incident small angle X-ray scattering (GISAXS) patterns of dip-coated nanoporous silica thin films were measured by Eggiman *et al.*[29] Simulated GISAXS patterns were analysed for different space groups (see Figure 3.10). These X-ray spot pattern simulations show differences between space groups that can also be observed by GIXD.

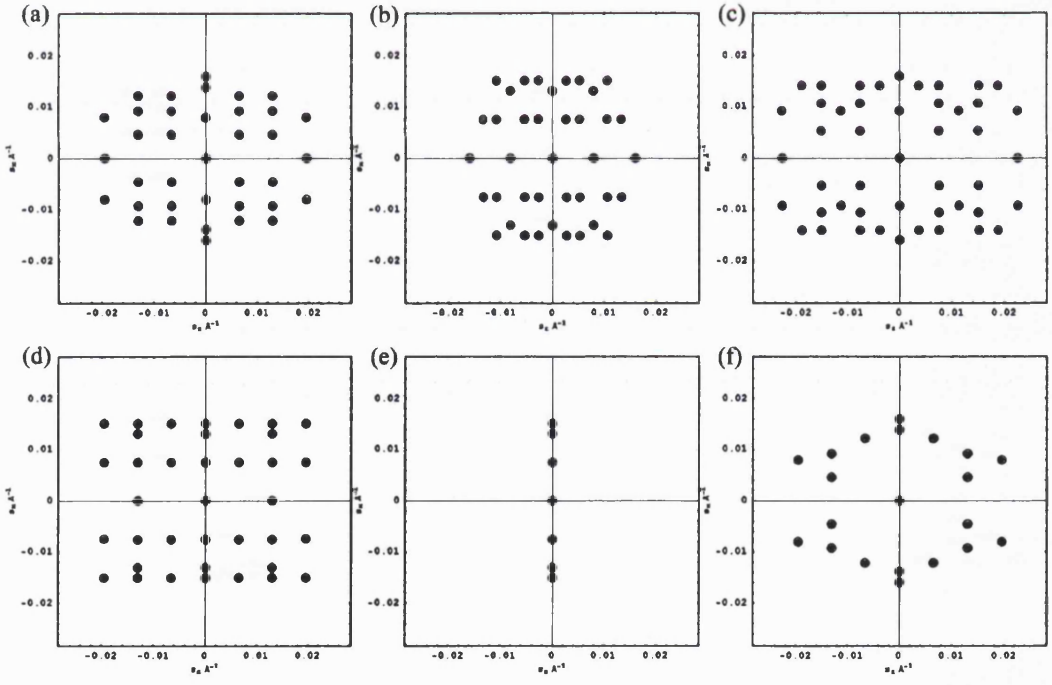

Figure 3.10. GISAXS pattern simulations of **(a)** (111) oriented body-centered cubic phase ($Im\bar{3}m$), **(b)** face-centered cubic phase (111) oriented ($Fm\bar{3}m$), **(c)** primitive cubic phase (111) oriented ($Pm\bar{3}n$), **(d)** 3D hexagonal phase ($P6_3/mmc$), **(e)** 2D hexagonal with sixfold axis perpendicular to the substrate $p6mm$, and **(f)** distorted cubic phase (111) oriented ($Ia\bar{3}d$) nanostructured thin films.[29]

3.3.3 *Description of the instrument: TROÏKA II (ID10B beamline)*

The ID10B is a multi-purpose beamline, which combine different techniques such as high-resolution diffraction, grazing-incidence diffraction, x-ray reflectometry and grazing-incidence small-angle scattering. These different setups are optimized for the study of liquid and solid interfaces.

The main parts of the beamline optics are the undulator, slits, monochromators, foil monitor, mirrors finishing with the photon shutter. This is in the optic hutch where the beam energies are split, directed, and filtered to get a very clean high-brilliance x-ray beam with an energy range of 8-13.5 keV. The equipment in the experimental hutch consists of the beam deflector, the incident flight path and the diffractometer, including various configurations of the detector arm (see Figure 3.11).[30]

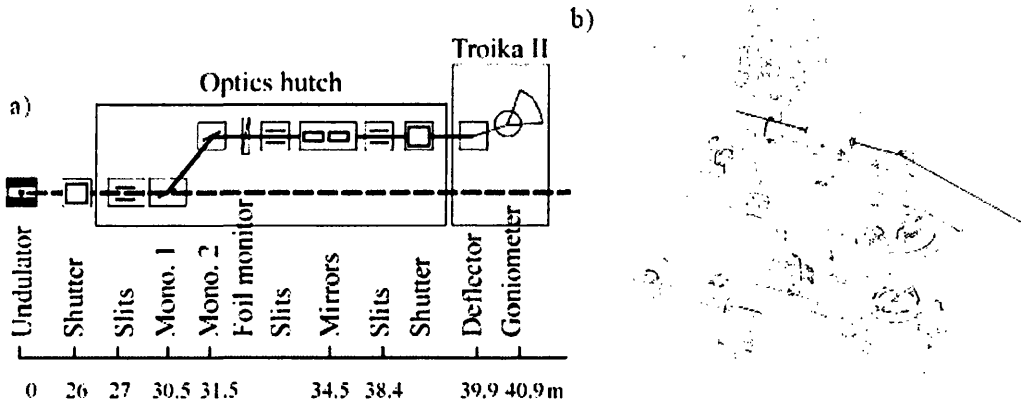

Figure 3.11. a) General layout of the ID10B beamline; b) Deflector and goniometer with no detector arm.[30]

Results obtained from both the X-ray reflectivity techniques and GIXD were extracted and analysed using IGOR PRO (Wavemetrics, Inc) program. The intensities were normalized by the intensity of the synchrotron beam monitored before the sample by the foil monitor. Due to intensity lost during scattering the measured intensity was lower than the monitored (incoming) intensity so the normalized values are less than one.

3.3.4 Brewster Angle Microscopy (BAM)

This optical microscopy technique allows the direct observation of thin films on transparent dielectric substrates as well as following the film growth progression in real time with high resolution.[23] It is based on the effect that from a clean surface no reflection occurs of p-polarized incoming light under the Brewster angle.[31] The "black background" of the Brewster Angle set-up allows using the detector (CCD-camera) with the maximum of change in intensity. A very thin layer with different refractive index will cause reflection. The reflectivity of a plane interface between two media of refractive index n_1, and n_2, depends on the polarization of the incident light and the angle of incidence θ. For a Fresnel interface the reflectivity vanishes at the Brewster angle θ_B[32]

$$\tan[\theta_B] = \frac{n_2}{n_1} \qquad 3\text{-}19$$

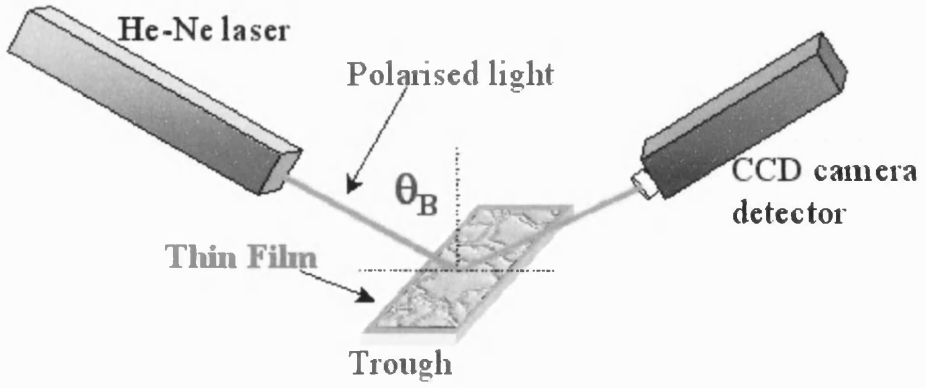

Figure 3.12. Representative scheme of the Brewster angle microscopy (BAM).

For a real interface, the reflected light intensity has a minimum at the Brewster angle, but does not vanish. The low reflected intensity at the Brewster angle is strongly dependent on the interfacial properties.[32]

The reflectivity of a real interface at the Brewster angle for the *p*-polarization has four origins:[32]

- The *thickness* of the interface. A dense monolayer of amphiphilic molecules introduces a variation of refractive index n over a thickness l ~20 Å. n and l depend on the phase domain of the monolayer: two different phase domains have different reflectivities.

- The *roughness* of interfaces. At liquid interfaces, the origin of the roughness is thermal fluctuations. However for monolayers at the water surface, the surface tension is large and the surface thermal fluctuations are small, introducing a small error on the thickness of the monolayer. And particularly for films thicker than monolayers substantial surface roughening can occur.
- The *anisotropy* of monolayers. Some concentrated phases in monolayers are optically anisotropic. This anisotropy can greatly increase the reflected intensity.
- The *density* of surface layer. This feature does not change much for amphiphilic monolayers but certainly does with the addition of silica or titania precursors.

As the Figure 3.12 shows the source is a polarized light coming from a He-Ne laser, with a wavelength of 532 nm, and the detector is a CCD camera, which collects the images. In the BAM images changes in brightness and contrast in solid-phase domains at the air-liquid interface are usually observed due to differences in molecular density as well as in the refractive index. When the beam hits the sample at the Brewster angle (53° for the air-water interface) and the film has not grown yet, then total absorption is produced in water solution. But when the film starts to grow the refractive index changes and total reflection occurs.[23, 33]

After further film development the film become continuous. Interference fringes may be visible at this point. These thin films present a non-uniform image in which alternating bright and dark bands or lines called fringes are observed (see Figure 3.13). This optical phenomenon occurs when interference occurs between light hitting the top air-film interface and bottom film-solution interface showing a smooth film of extremely uniform thickness, otherwise this effect could not be observed.

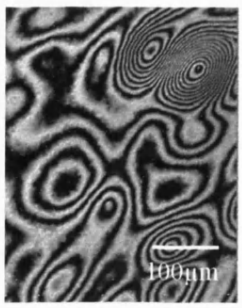

Figure 3.13. BAM image of the formed film showing the interference fringes.

3.4 Sub-phase Solution Study Techniques

3.4.1 Small Angle Neutron Scattering (SANS)

Small angle scattering (SAS) is the collective name given to the techniques of small angle neutron (SANS), X-ray (SAXS) and light (SALS, or LS) scattering. In each of these techniques radiation is scattered by the sample and the resulting scattering pattern is analysed to provide information about the size, shape and orientation of some components of the sample.

In any SAS experiment, some of the incident radiation is transmitted by the sample, some is absorbed and some is scattered. A detector positioned a distance L from the sample (see Figure 3.14) records the flux of radiation scattered. This flux, $I(\lambda,\theta)$, may be expressed in general terms in the following way

$$I(\lambda,\theta) = I_0(\lambda)\ \Delta\Omega\ \eta(\lambda)\ T\ V\ \frac{\partial\sigma}{\partial\Omega}(Q) \qquad 3\text{-}20$$

where I_0 is the incident flux, η is the detector efficiency (or response), T is the sample transmission and $(d\sigma/d\Omega)(Q)$ is a function known as the *differential cross-section.* The differential scattering cross-section measures the ability of an object to remove particles from a directed beam and send them into new directions (see Fig. 3.14).

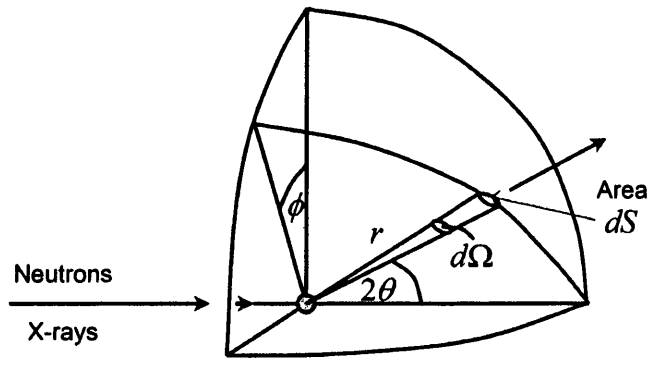

Figure 3.14. Geometrical representation of the scattering cross section.[34]

$$\frac{\partial\sigma}{\partial\Omega}(Q)=\frac{\left(\text{No. scattered/sec into } d\Omega = dS/r^2\right)}{\Phi\, d\Omega} \rightarrow \sigma(Q)=\int\frac{d\sigma}{d\Omega}d\Omega \qquad 3\text{-}21$$

From equation 3-20 the first three terms are clearly instrument-specific whilst the last three terms are sample-dependent. The objective of a SANS experiment is to determine the differential cross-section, since it is this which contains all the information on the

shape, size and interactions of the scattering bodies in the sample. The differential cross-section, normally expressed in cm^{-1}, is given by

$$\frac{\partial\sigma}{\partial\Omega}(Q)=N_i V_i^2 (\Delta\rho)^2 P(Q)S(Q)+B_{inc} \qquad 3\text{-}22$$

where N_i is the number concentration of scattering bodies, V_i is the volume of one scattering body, $P(Q)$ is the form or shape factor, $S(Q)$ is the interparticle structure factor, and B_{inc} is the incoherent background signal. $(\Delta\rho)^2$ is the square of the difference in neutron scattering length density (also called the *contrast*) between that part of the sample of interest, ρ_p, and the surrounding medium, ρ_m.

$$(\Delta\rho)^2 = (\rho_p - \rho_m)^2 \qquad 3\text{-}23$$

The cross-section depends on Q, which is the modulus of the *scattering vector* ($Q = (4\pi\sin\theta)/\lambda$) where θ is half of the scattering angle. The scattering length density (ρ) describes the ability of the nucleus to scatter neutrons and it is defined as $\rho = b_j n_j$ where n_j is the number of nuclei and b_j is the scattering length of the nucleus j of every atom type. Consequently variations in $P(Q)$ would imply changes in the shape of the micelles, whilst variations in $S(Q)$ would indicate changes in intermicellar force. [35, 36]

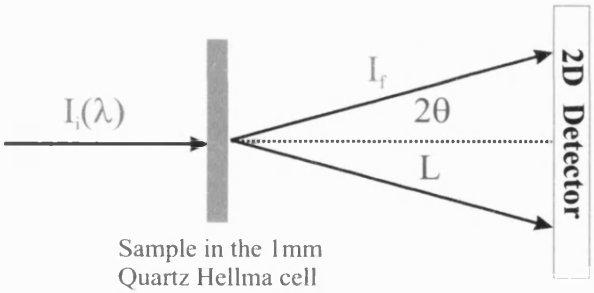

Figure 3.15. Scheme showing the Small Angle Scattering geometry.

One of the most important aspects of neutron techniques is that hydrogen and deuterium have completely different scattering powers as mentioned in section 3.1.1. Since water is the main component in most of the samples, in this case as the solvent, its total or partial substitution by D_2O was prepared. The differences in scattering length of H_2O and D_2O ($b_{H2O} = -1.68 \times 10^{-5}$ Å and $b_{D2O} = 19.15 \times 10^{-5}$ Å) allow us to highlight or mask the scattering from different parts of the silica-surfactant assembly.[37, 38]

X-rays and neutron scattering length densities for every reactant involved in the synthesis of silica and titania mesoporous thin films, described in this thesis, are summarised in Table 3.3. The first column in the table is the molecular weight (MW),

the second is the bulk density (*d*), the third is the X-ray scattering length density calculated assuming a wavelength of 1.54 Å and the forth column is the neutron scattering length density.

Table 3.3. Scattering length densities (ρ) for the components involves in the synthesis of the mesoporous silica and titania thin films

			Cu Kα X-rays	SANS
Compounds	**MW**	***d* (g/cc)**	**$\rho/10^{-6}$ Å^{-2}**	**$\rho/10^{-6}$ Å^{-2}**
-$C_{16}H_{33}$	225	0.77	7.49	-0.351
-$C_{16}H_{33}O_9$	369	0.977	9.05	0.561
-$N^+(CH_3)_3$	59.11	~1	9.78	-0.443
$C_{16}EO_8$	594	0.977	9.22	0.18
Brij 56	683	0.997	9.39	0.232
CTAB	364.45	~1	9.2	-0.241
SDS	288.38	0.37	3.41	0.123
TMOS	152.22	1.03	9.47	0.37
$Ti(OBu)_4$	340.34	0.99	9.21	-0.149
SiO_2	60.08	2.205	18.9	3.49
TiO_2	79.87	3.9	2.4	31.7
MeOH	32.04	7.91	7.57	-0.373
BuOH	74.12	0.81	7.81	-0.329
HCl	36.45	1.2	10.2	1.16
H_2O	18.015	1	9.46	**-0.56**
D_2O	20.03	1.107	9.42	**6.37**

The hexadecyl group, highlighted in green, corresponds with the $C_{16}EO_8$ and CTAB hydrophobic part; the ethylene oxide and the trimethylammonium groups, highlighted in red, are the hydrophilic parts of the $C_{16}EO_8$ and CTAB respectively; the compounds in blue are the products obtained after the TMOS and $Ti(OBu)_4$ hydrolysis and condensation.

To obtain the value of the scattering length densities shown in the table above, the $\rho(H_2O)$ is calculated as example:

– The neutron scattering length density is given by:

$$\rho = \frac{\sum b_i}{V_m} \quad \text{or} \quad \frac{\sum b_i \times d \times N_A}{\text{MW}} \qquad 3\text{-}24$$

where V_m is the molecular volume, d is the density, N_A the Avogadro's number, and MW the molecular weight.

Therefore, using the scattering length values for H and O given in Table 3.1 the scattering length density for water is:

$$\rho(H_2O) = \frac{\left[\left(2 \times -3.74 \times 10^{-13}\right) + \left(1 \times 5.8 \times 10^{-13}\right)\right] \times 1.0 \times N_A}{18} = -0.56 \times 10^{10}\,\text{cm}^{-2} \text{ or } -0.56 \times 10^{-6}\,\text{Å}^{-2}$$

— The corresponding quantity for X-rays is obtained by replacing the b_i values in the expression by Zr_e, where $r_e = 2.81 \times 10^{-13}$ cm, is the classical radius of the electron, and Z is the atomic number of the i atoms in the molecular volume V_m.

3.4.1.1 Description of the instrument LOQ

In this thesis neutron scattering experiments were performed on the SANS instrument, called LOQ, at the ISIS Spallation Neutron Source of the Rutherford Appleton Laboratory, Oxfordshire, UK (see Figure 3.16). A range of wavelengths between 2.2 Å to 10 Å at 25 Hz are used to cover the scattering vector range of Q = 0.06 - 0.24 $Å^{-1}$ by the time-of-flight method with a 4m sample to detector distance (L). The samples are prepared and transferred into 1.0 mm thick, double stopper, quartz Hellma cells which can be sealed or opened to allow faster reaction since some evaporation is allowed to occur.[39, 40] The data was collected and corrected using the LOQ programme "Collete". The data is normalized by transmission measurements, corrected by background subtraction, and radially averaged to produce a 1D pattern. The background consisted of an acidic solution using three D_2O/ H_2O contrasts. Results from SANS were processed by IGOR PRO (Wavemetrics, Inc.) program. Structural models, written by the "SANS group" at the NIST Centre for Neutron Research, were used to fit the data.

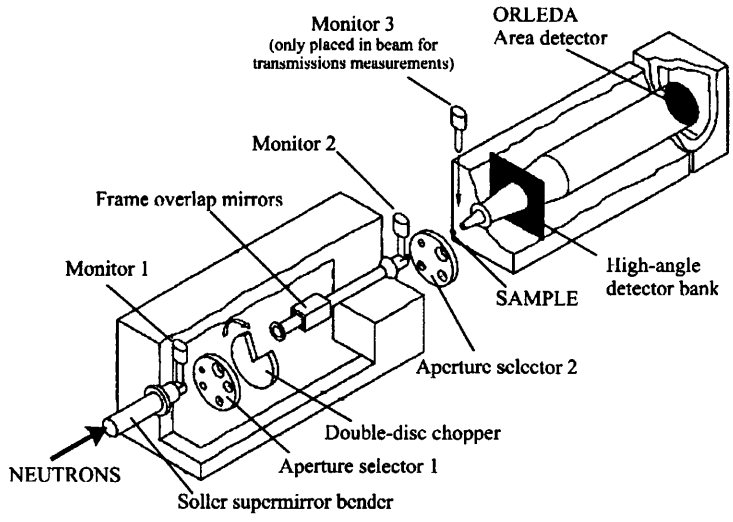

Figure 3.16. Diagram of the LOQ-small angle scattering instrument.[7]

Concluding, SANS measurements record the processes occurring in the bulk solution, which precede the film formation.

3.5 References

(1) Jacobson, D.; Arif, M.; Huffman, P.; Satija, R. In *NCNR 2003 Annual Report*; NIST: Gaithersburg, US, 2003.
(2) Wiley, J. *Modern Techniques for Polymer Characterisation*; R A Pethrick & J V Dawkins, 1999.
(3) Sears, V. F. *Neutron News* **1992**, *3*, 26-37.
(4) Cubbit, R.; Fragneto, G. In *Scattering in Microscopic Physics and Chemical Physics.*, 2002.
(5) Cubitt, R.; Fragneto, G.; Ghosh, R. E.; Rennie, A. R. *Langmuir* **2003**, *19*, 7685-7687.
(6) Penfold, J. In *Trends in Colloid and Interface Science Iv*, 1990; Vol. 81, pp 198-202.
(7) King, S. M. *Fibre Diffraction Review* **2004**, *12*, 15-20.
(8) Haensel, R. *Ieee Transactions on Nuclear Science* **1992**, *39*, 44-48.
(9) Altarelli, M. *Physica Scripta* **1994**, *55*, 9-13.
(10) Chavanne, J.; Elleaume, P.; Van Vaerenbergh, P.; European Synchrotron Radiation Facility: B.P. 220, F-38043 Grenoble Cedex, France.
(11) *http://www.esrf.fr/UsersAndScience/Experiments/Beamlines/*.
(12) Ibel, K.; Scientific Coordination Office, ILL, 1994.
(13) *http://www.isis.rl.ac.uk/LargeScale/LOQ/loq.htm*.
(14) Als-Nielsen, J.; Jacquemain, D.; Kjaer, K.; Leveiller, F.; Lahav, M.; Leiserowitz, L. *Physics Reports* **1994**, *246*, 251-313.
(15) *http://hyperphysics.phy-astr.gsu.edu/hbase/phyopt/totint.html*.
(16) Brown, A. S.; Holt, S. A.; Saville, P. M.; White, J. W. *Australian Journal of Physics* **1997**, *50*, 391-405.
(17) Tolan, M. *X-Ray Scattering from Soft-Matter Thin Films*; Springer: Berlin, 1999.
(18) Holy, V.; Pietsch, U.; Baumbach, T. *High-Resolution X-Ray Scattering from Thin Films and Multilayers*; Springer: Berlin, 1999.
(19) Als-Nielsen, J.; Mc Morrow, D. *Elements of Modern X-ray Physics*; Wiley: Chichester, 2001.
(20) Born, M.; Wolf, E. *Principles of Optics*; Pergamon Press: Oxford, UK., 1993.
(21) Parratt, L. G. *Physical Review* **1954**, *95*, 359–369.
(22) Sinha, S. K.; Sirota, E. B.; Garoff, S.; Stanley, H. B. *Physical Review B* **1988**, *38*, 2297-2311.
(23) Edler, K. J.; Goldar, A.; Hughes, A. V.; Roser, S. J.; Mann, S. *Microporous and Mesoporous Materials* **2001**, *44*, 661-670.
(24) Klug, H. P.; Alexander, L. E. *X-Ray Diffraction Procedures for Polycrystalline and Amorphous Materials.*; John Wiley & Sons: New York, 1974.
(25) Klotz, M.; Albouy, P. A.; Ayral, A.; Menager, C.; Grosso, D.; Van der Lee, A.; Cabuil, V.; Babonneau, F.; Guizard, C. *Chemistry of Materials* **2000**, *12*, 1721-1728.
(26) Chao, K.-j.; Liu, P.-h.; Huang, K.-y. *Comptes Rendus Chimie* **2005**, *8*, 727-739.
(27) Holt, S. A.; Foran, G. J.; White, J. W. *Langmuir* **1999**, *15*, 2540-2542.
(28) Doshi, D. A.; Gibaud, A.; Goletto, V.; Lu, M. C.; Gerung, H.; Ocko, B.; Han, S. M.; Brinker, C. J. *Journal of the American Chemical Society* **2003**, *125*, 11646-11655.
(29) Eggiman, B. W.; Tate, M. P.; Hillhouse, H. W. *Chemistry of Materials* **2006**, *18*, 723-730.

(30) Konovalov, O.; Struth, B.; Smilgies, D. M.; European Synchrotron Radiation Facility: Grenoble, France, pp 1-5.
(31) Honig, D.; Mobius, D. *Journal of Physical Chemistry* **1991**, *95*, 4590-4592.
(32) Henon, S.; Meunier, J. *Review of Scientific Instruments* **1991**, *62*, 936-939.
(33) Edler, K. J.; Roser, S. J.; Mann, S. *Chemical Communications* **2000**, 773-774.
(34)
(35) King, S. M.; ISIS Facility, Ruterford Appleton Laboratory: Didcot, UK, 1995.
(36) Penfold, J.; Staples, E.; Cummins, P. G. *Advances in Colloid and Interface Science* **1991**, *34*, 451-476.
(37) Brennan, T.; Roser, S. J.; Mann, S.; Edler, K. J. *Chemistry of Materials* **2002**, *14*, 4292-4299.
(38) Penfold, J. *Current Science* **2000**, *78*, 1458-1466.
(39) Mortensen, K.; Pedersen, J. S. *Macromolecules* **1993**, *26*, 805-812.
(40) Pedersen, J. S.; Hamley, I. W.; Ryu, C. Y.; Lodge, T. P. *Macromolecules* **2000**, *33*, 542-550.

Chapter 4 Temperature and Humidity effect on CTAB-Templated Mesophase Silica Films

4.1 Introduction

In the formation process of mesoporous silica from acidic solutions, the inorganic silica network is formed via a so-called counterion mediated interaction ($S^+ X^- I^+$) at low pH where both the surfactant and inorganic precursor species are positively charged.[1] Work by others, based on reflectivity measurements, described the main stages in the mechanism, with an induction period and transitional growth phase observed prior to establishment of the final film structure.[2] The addition of extra counterions, accelerates the film formation and causes a shift in the phase diagram changing the mesostructure of the films.[3-5] Previously Edler *et at*[6, 7] reported a study of the concentration dependence of the self-assembly process. A mechanism was proposed to explain the spontaneous self-assembly observed during the formation of thin films at air-water interface using cetyltrimethylammonium bromide (CTAB) as the surfactant and tetramethoxysilane (TMOS) as the silicate precursor. This mechanism is based on the observed horse-shoe-shaped variation in the film formation time with changing TMOS concentration and studies of the development of mesostructure at the air solution interface, which suggest two self-assembly regimes in the formation of these films. [6, 7] The mechanism is surface-driven at high and low silica concentrations where cylindrical silica-coated micelles reach the surface and reorder to form the oriented hexagonal mesophase observed in the final film.[8]

However at intermediate concentrations a bulk-driven mechanism takes place where larger mesostructured particles are formed in the bulk solution and diffuse to the surface where they pack to form the film.[6, 7] In this CTAB/TMOS system where the surfactant and silica have the same charge, it is suggested that the silica acts like a polyelectrolyte and a complex coacervation process occurs in solution for a narrow range of concentrations, forming concentrated phase-separated liquid particles surrounded by a dilute silica-surfactant solution.[1] Brennan *et al* [7] demonstrated that at intermediate concentrations there is formation of mesostructured particles in the bulk solution, corresponding to the observed particle-driven film formation at these

concentrations. At high silica concentrations the coacervation does not occur due to repulsion between the silica-coated micelles and the partial silica-coated micelles at these concentrations.[7, 9]

In this chapter, it is examined how the in situ control of temperature and humidity, as well as silicate precursor concentration, affect the kinetics, the structure, and the mechanism of the formation of surfactant-templated mesoporous silicate thin films at the air-liquid interface. Changes in the film formation mechanism have been observed, which suggest that, along with the surfactant-silicate concentration and charge density, the humidity and temperature determine whether a bulk or surface-driven formation mechanism occurs. Using off-specular X-ray reflectivity as a surface characterization technique and controlling the atmosphere above the growing film in an enclosed sample cell enables changes in the film growth process to be followed in real time.

4.2 Experimental Procedure

4.2.1 Sample preparation

Surfactant-templated silica thin films in acidic solution using cetyltrimethylammonium bromide (CTAB) as surfactant and tetramethyl orthosilicate (TMOS) as the silica precursor were obtained following the experimental procedure explained in chapter 2.The synthesis solution was prepared with molar ratios of: CTAB/ water/ HCl/ TMOS $1.53x10^{-3}$: 1: 3.63 x 10^{-3}: X, varying the TMOS molar ratio in the range (X) from $5.4x10^{-3}$ to $1.63x10^{-2}$ (ie from 0.29 to 0.80 M).

The film growth was carried out at different TMOS concentrations under specific temperature and humidity conditions using an enclosed sample cell, which was designed for this purpose. The cell consists of a copper base provided with temperature control by water flow from a water bath, through a reservoir set in the base (see Figure 4.1). The Teflon trough sits in a copper block holder on top of the base to maintain good thermal contact but allow easy removal for cleaning. The bottom of the Teflon trough is ~ 0.5 mm thick to ensure good heat transfer to the solution.

To study the effect of changing the atmosphere above the solution the trough is covered by an aluminium box with two double windows made from pure polyimide film (thickness 0.025 mm Grade: Kapton HN®) situated in both sides. These allow X-rays to pass through with no detected peaks in the small angle region and the double window

construction helps to prevent condensation on the windows at high temperatures. An inlet -outlet tap system allows dry N_2 to flow through the cell. A foil baffle was positioned over the inlet to prevent the airflow from disturbing the surface of the solution. To measure the humidity (RH) and the temperature a hand held thermohygrometer probe (ROTRONIC, Hygrolog-D®) was inserted into the cover. Temperatures in the range from 25 to 40 ± 0.7°C and relative humidities in the range from 50 to 100 ± 6% were studied. 100% RH is reached by leaving the cell closed and lower RH was achieved by regulating the flow of dry N_2 gas.

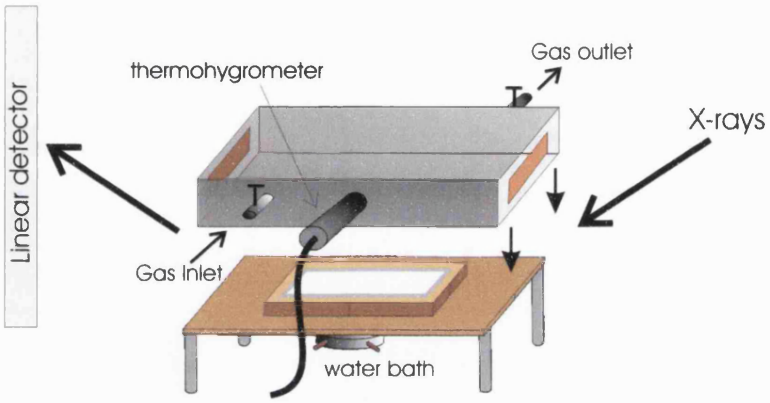

Figure 4.1. Schematic of the enclosed cell used to control the humidity and the temperature during X-ray reflectivity measurements.

4.2.2 Experimental techniques

Off specular X-ray reflectivity measurements were carried out on beamline ID10B (Troika II) at the ESRF using an energy of 8.01 keV (λ = 1.54613 Å). Specular reflectivity was measured for an angular range of 0-4° (Q = 0-0.567 $Å^{-1}$). The incident angle (θ_i) was set at 1.27°.

4.3 Results

4.3.1 Humidity effects

The growth of mesostructured silica thin films at the air-water interface occurs in three stages; an induction period; a mesostructure development period; and a surface-coarsening period (see Figure 4.2).[10] These stages will be used to define the process of film growth in the following off specular reflectivity measurements. Figure 4.2 shows off specular patterns as observed on the linear detector, with the bottom of the detector on the left of the figure and the top of the detector on the right. The induction period covers the time from when the mixed solution is poured into the trough, to when the first diffraction order peak starts to grow at Q = 0.11 $Å^{-1}$. During this period the observed pattern closely resembles that of a clean water interface (Figure 4.2a) with only a peak due to the specularly reflected beam and the Yoneda wing at an angle corresponding to the critical angle of the surface (Q = 0.077 $Å^{-1}$). The Yoneda wing is a doubling of the scattered intensity at the critical angle of the surface caused by mesoscale surface roughness.[7] The mesostructure development period represents a period of rapid film growth over a period of about 30 minutes to cover the interface (Figure 4.2b & 4.2c). It is distinguished by the presence of the specular peak, which starts to decrease in intensity and by the Yoneda wing and diffraction peaks, which increase in intensity. The increase in intensity of the diffraction peaks corresponds to development of an ordered mesophase in the growing film. Finally the surface-coarsening period, in which the surface becomes increasingly rough, is shown by the absence of a specular reflection peak, a constant or decreasing Yoneda peak and the further development of the intensity of diffraction peaks (Figure 4.2d).

Changes in the Yoneda wing and specular peak intensity indicate the rate at which the film surface becomes rough.[11] In fact as the surface becomes increasingly rough the specular peak decreases in intensity while the Yoneda wing grows in intensity until the roughness becomes macroscopic at which point the Yoneda wing intensity begins to decrease again.[11] Changing the TMOS concentration alters the shape of the developing first and second order diffraction peaks and the rate of disappearance of the specular peak,[7, 11] which suggests that the mechanism by which the ordered mesostructured film at the air- liquid interface is formed is different.

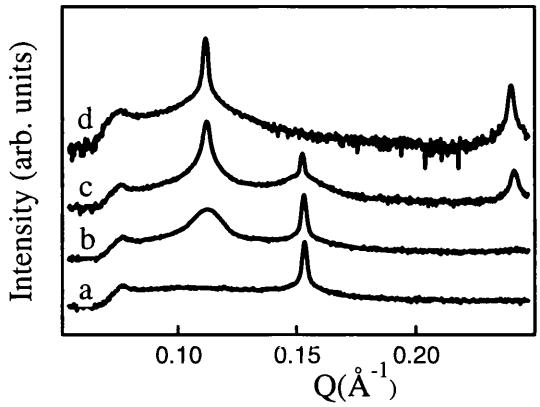

Figure 4.2. Off specular profiles showing the three stages of growth in the silica thin films: a) induction period; b) and c) mesostructure development period; d) surface coarsening period.

To understand how ambient humidity affects the film development, off-specular studies were performed on 7.2 TMOS/ CTAB molar ratio under different humidities at room temperature. Previous measurements at ambient humidity have shown that this ratio is in the particle-driven regime of film development.

During the early induction period at 100% RH, as Figure 4.3a shows, the Yoneda and the specular peak only are present. At the same RH, the profile in Figure 4.3b shows a very broad first order diffraction peak, which develops from 636 to 713 min after mixing, and the specular reflectivity peak. A third measurement, represented in Figure 4.3c, was performed within ambient conditions (25 °C and 50% RH) where a sharp first diffraction peak is observed after 110 min. In previous investigations at ambient humidity (ca. 50% RH) well-defined first and second order peaks, corresponding to the final film formation and surface roughening, were observed to appear after 200 min, almost four times faster than the sample shown in Figure 4.3b.[7] Therefore the high humidity slows down the reaction and prevents mesostructural ordering, since only a low broad first order diffraction peak is visible. The continued presence of the specular reflectivity peak and unchanging Yoneda peak also show that high humidity prevents surface roughening.

Looking at the sample case shown in Figure 4.3b, after 713 min dry N_2 was pumped through the cell decreasing the humidity to 55.5% and instigating a number of rapid changes in the reflectivity profile. A sharper and more intense first order diffraction peak developed from the broad low intensity peak and specular peak

vanished, which indicates a fast development of a well-ordered mesostructure within the existing film upon the reduction in the % RH.

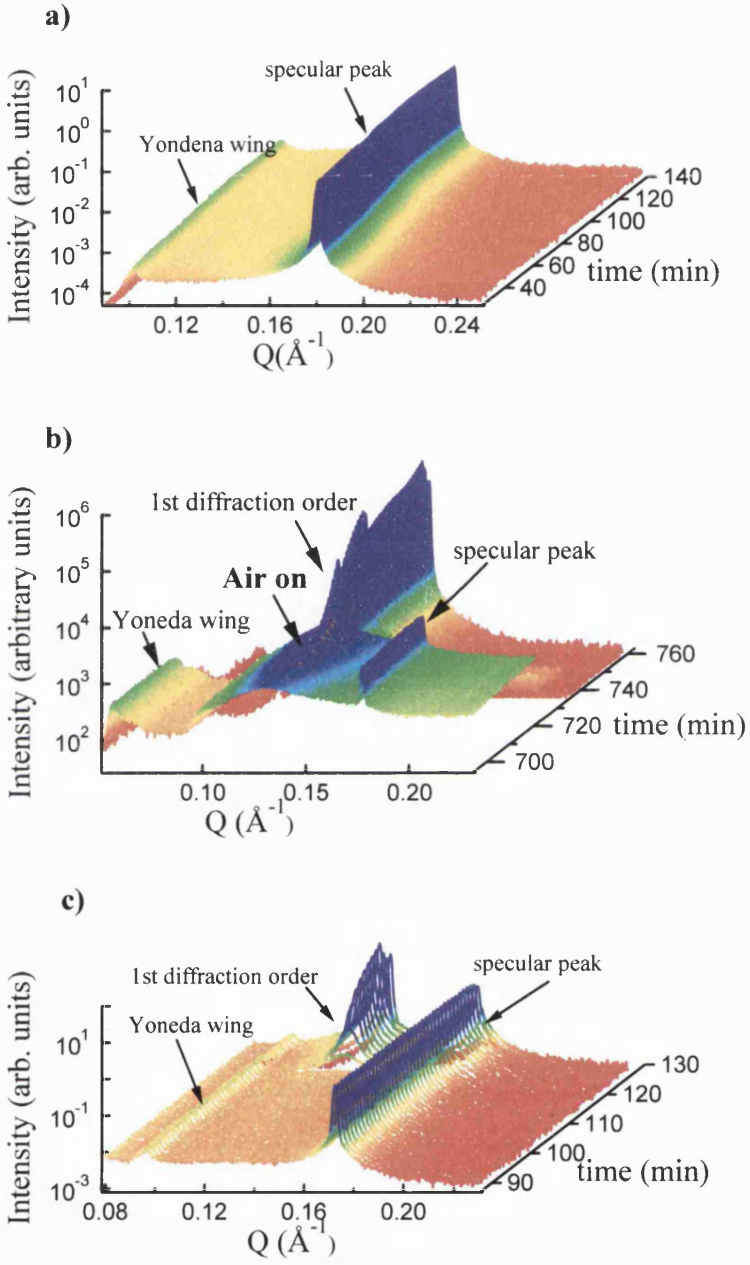

Figure 4.3. Off specular profile against time showing the effect of relative humidity on mesostructure development for a molar ratio of TMOS/CTAB = 7.2 at: a) 25 °C and 100%RH from short reaction times; b) 25 °C in which the initial humidity during film growth was 100% RH until 720 min since mixing and this was reduced to 55.5 % RH when the N_2 flow was turned on at 720 min after mixing; c) 25 °C and 50%RH from times between 85 and 130 min after mixing.

Looking more closely at Figure 4.3b shows an interesting weak, but sharp peak, that appears at Q = 0.138 $Å^{-1}$ (d = 45.5 Å) close to the first order diffraction peak, at Q = 0.136 $Å^{-1}$ (d = 46.2 Å), shown in Figure 4.4. This small peak grew at the time when the dry N_2 was injected through the cell, changing the humidity conditions, and became obscured by the developing first order after 14 minutes.

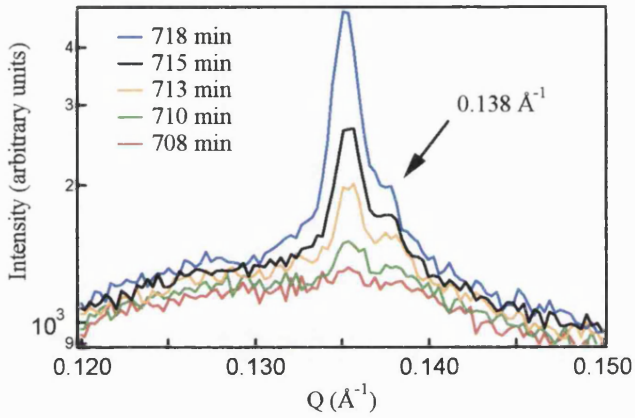

Figure 4.4. Off specular profile of a weak peak that appears, close to the first diffraction peak, 14 min after the dry N_2 was injected through the cell.

Although there is not enough information to assign this peak to a specific mesophase, the new d spacing suggests a transition in the mesophase structure. It could belong to several structures (a hexagonal phase with different spacing or a lamellar phase among others), but a transient 3D organized micellar phase of close packed spherical micelles could be one possibility. The broad peak of the observed mesophase developed at high humidity, prior to the gas flow, is similar to that suggested to belong to a film mesostructure consisting of glass of spherical micelles. Such structures were observed using dodecyltrimethylammonium chloride by Ruggles *et al.*[3] When the humidity is reduced, drying out the top layers of the film, the removal of water may bring these charged spherical micelles closer together, causing transient formation of an ordered phase composed of close-packed spheres, either in a cubic or 3D hexagonal arrangement. Further rearrangement of the micelles in the film to minimize the energy of the system after the sudden change in humidity results in the production of the normally observed 2D hexagonal phase consisting of long rodlike micelles arranged parallel to the interface. Other workers have shown that the transition between the micellar cubic $Pm\bar{3}n$ phase and the 2D *p6mm* hexagonal phase occurs via a facile

rearrangement of micelles along the related (10) plane of the hexagonal and (211) plane of the cubic,[12] and a similar transition could occur between the close-packed micelles in these films. The driving force for this transition would be the increasing local charge density caused by the removal of water from the interface.

The general effect of humidity on film growth is represented in Figure 4.5 where the intensity of the specularly reflected peak and the first order diffraction peak are extracted as a function of time. As the RH increases there is a progressive increase in the time taken for both the specular reflectivity peak to drop in intensity (Figure 4.5a) and the first order diffraction peak to grow in (Figure 4.5b). In Figure 4.5a the specular peak intensity decays to a higher background value in the 70% RH than in the 50% RH data since there is more parasitic scattering due to the water in the atmosphere above the film. At 100%RH the intensity of the specular peak decreases slowly over the entire period of film development, since the film in this case never becomes rough. The intensity of the first order diffraction peak at 100% RH in Figure 4.5b shows a roughly constant behaviour in time since no sharp peak was observed at this %RH. At about 636 minutes there is a small increase in intensity corresponding with the development of the low intensity bump at the first order diffraction peak position shown in Figure 4.3b (prior to the humidity jump). In Figure 4.5b the discontinuities in the 100% RH profile between 488 - 496 minutes and between 601 - 633 minutes, were due to temporary interruptions to the synchrotron beam.

Therefore the humidity directly affects the time for both mesostructure formation and surface roughening, demonstrating that as the %RH increases the film takes more time to form. This is also reflected in the evaporation rate from the solution surface for these samples, which can be measured by observing the change in position of the specular peak on the detector with time. As the solution evaporates, the specular peak moves down the detector at a constant rate. By plotting this position with time the rate of evaporation can be expressed in $Å^{-1}min^{-1}$. The measured evaporation rates change by an order of magnitude between the samples at the three %RH measured from 5.46×10^{-6} $Å^{-1}min^{-1}$ at 100% RH, to 1.70×10^{-5} $Å^{-1}min^{-1}$ at 70% RH and 2.06×10^{-4} $Å^{-1}min^{-1}$ at 50% RH. Similar experiments have been carried out at 40°C and also show an increasing time for film formation with increasing %RH corroborating the conclusion derived at 25°C.

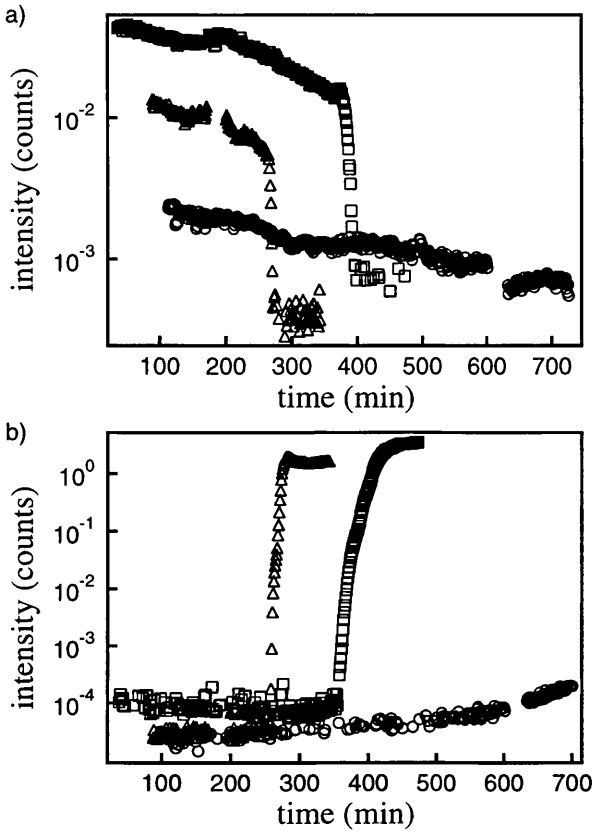

Figure 4.5. Variation of the peak intensities with time at different humidity values (△ 50 % RH, □ 70 % RH, ○ 100 % RH) during the diffuse scattering experiments, collected from 7.2 TMOS/CTAB molar ratio film at 25°C for (a) the reflectivity peak and (b) first diffraction order peak.

4.3.2 Silica precursor concentration effect

Besides the effect of humidity on the development of the off-specular scattering profile, it is interesting to note the effect of varying TMOS concentration at 100% RH. Although film formation is generally slower for the 10.7 than the 7.2 TMOS/CTAB molar ratio film the specular reflectivity peak has a significantly greater intensity after 700 min in the 10.7 molar ratio film (Figure 4.6). This suggests that the ratio 10.7 film is much smoother than the 7.2 molar ratio film, although a film was visible to the eye at the surface of solution in both cases. The presence of a weak bump at the position of the first order diffraction peak, at both TMOS/CTAB molar ratios, suggests a poorly ordered mesostructure, corresponding possibly to a glass of spherical micelles[3-5] or a very disordered wormlike structure. Previous experiments at ambient humidity have suggested that film formation at 10.7 TMOS/CTAB ratio is surface driven, forming through the gradual accumulation of micelles at the interface, while at 7.2

TMOS/CTAB the film forms from the packing of particles created in the bulk.[6] In this case, the high humidity appears to prevent ordering of the mesostructure at the interface, but a film composed of silica-surfactant particles from the bulk would be expected to be rougher than one formed through gradual aggregation of individual micelles, indicating that the expected mechanisms may be operating in both films at high humidity.

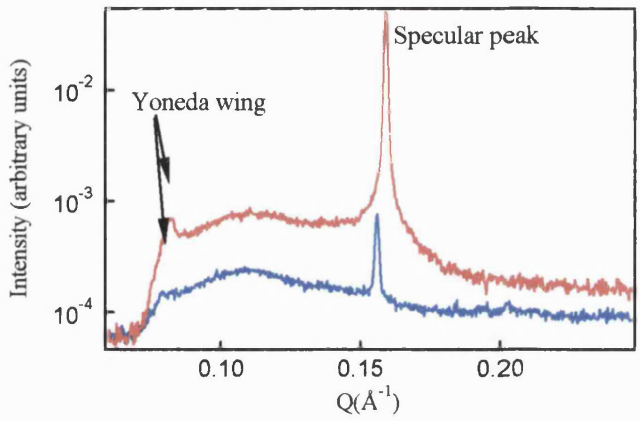

Figure 4.6. Diffuse X-ray scattering data for two TMOS/ CTAB molar ratios: (—) 7.2 and (—) 10.7, recorded 700 min after mixing at 25°C and 100% of humidity.

4.3.3 Temperature effect (50% RH)

The time required for film formation while changing the TMOS/CTAB molar ratio at ~36°C and ~50% RH is also studied to compare with our earlier results collected under ambient conditions. In this case, temperature and humidity were controlled by a water bath and the air flowing though the enclosed cell. The average measured temperature was 36.75 ± 0.36°C and average value of the relative humidity was 51.75 ± 2.87% over all the experiments at different molar ratios although there were slight differences for each sample (see Table 4.1). A comparison between the times for film formation at the same TMOS/CTAB molar ratio and humidity at two different temperatures are shown in Figure 4.7. The data at 22°C were taken with no humidity control, although subsequent measurements of the ambient humidity in the ID10B blockhouse showed it to be roughly constant around 50%. The ambient temperature within the blockhouse was maintained at 22 ± 1°C.[6] A decrease in the film formation time was observed at the higher temperature. Thus the effect of increasing the humidity on the rate of film growth is opposite to the effect of increasing the temperature.

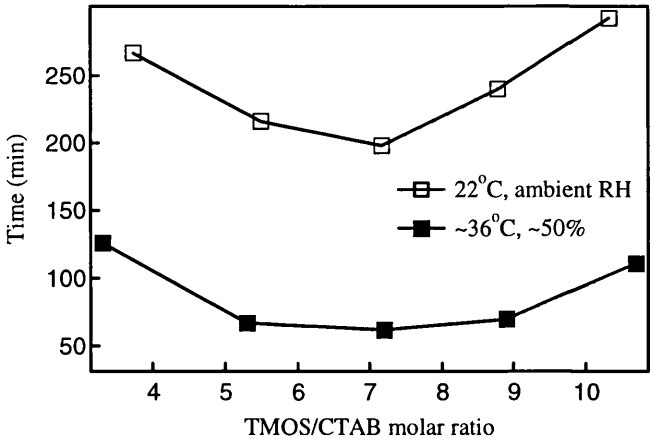

Figure 4.7. Film formation time for various TMOS/CTAB molar ratios at ambient temperature and RH (□) obtained from previous experiments, and 36°C, 50% RH (■) obtained from diffuse X-ray scattering measurements.

Table 4.1. Time taken for the first diffraction peak to appear in the off specular reflectivity measurements and the peak position for different TMOS/CTAB molar ratios at ~ 36°C and ~ 50% RH.

TMOS/CTAB molar ratio	Time (mins)	T (°C)*	RH (%)*	Evaporation rate ($Å^{-1}min^{-1}$)	1st order peak position ($Å^{-1}$)
3.3	126	37.44 ± 0.11	48.12 ± 1.92	1.03×10^{-4}	0.143
5.3	67	36.88 ± 0.58	54.69 ± 3.99	2.28×10^{-4}	0.140
7.2	62	36.0 ± 0.87	53.40 ± 6.67	2.06×10^{-4}	0.143
8.9	65	36.62 ± 0.14	52.25 ± 1.18	2.55×10^{-4}	0.140
10.7	107	36.81 ± 0.09	50.31 ± 0.58	2.22×10^{-4}	0.146

*The errors in the temperature and humidity are the standard deviation of all measurements taken from 25 minutes after the sample was added into the trough until the film was formed. During the first 25 minutes the temperature and humidity had not reached stable values but oscillated around the set points.

Interestingly the position of the minimum time for film formation remains at a TMOS/CTAB ratio of 7.2 suggesting that there is little change in the formation mechanism with increasing temperature despite the faster film formation times.

Examination of the peak width with time of the growing first order diffraction peak was performed at 50% RH for two different temperatures conditions, at 22°C (Figure 4.8A) and 36°C (Figure 4.8B) for several TMOS/CTAB molar ratios, where an important temperature effect on the formation mechanism was observed. In Figure 4.8A a large decrease in peak width for 3.3 and 10.7 ratios can be seen, although in Figure

4.8B this peak width decrease is observable in all cases except for the ratio at the minimum film formation time (TMOS/CTAB = 7.2). This suggests that the surface driven mechanism becomes more strongly favoured at higher temperatures.

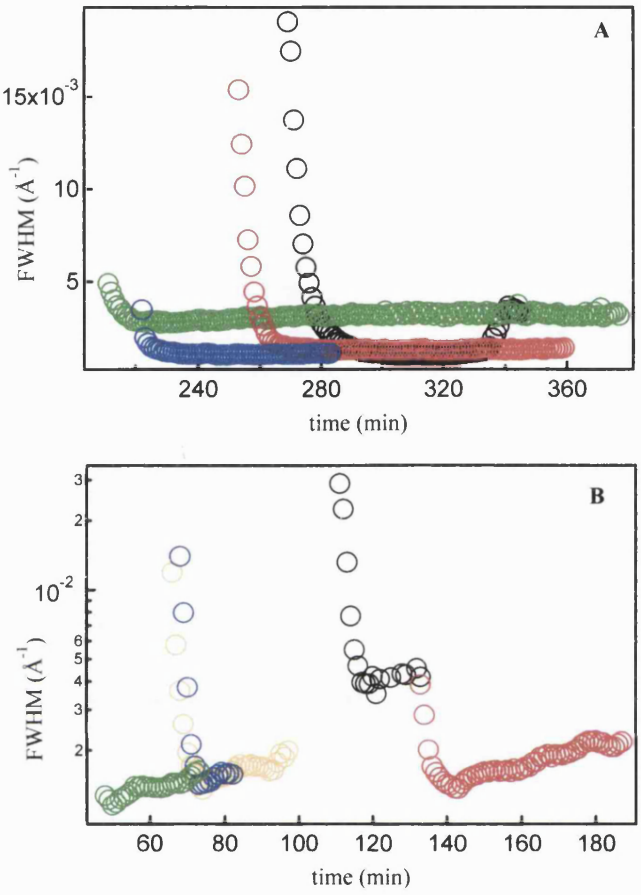

Figure 4.8. The temporal variation of the peak width (FWHM) of the first diffraction peak in the off specular reflectivity patterns at (**A**) ~22°C and ~50% RH and (**B**) ~36°C and ~50% RH for different TMOS/CTAB molar ratios: 3.3 (O), 5.3 (O), 7.2 (O), 8.9 (O), and 10.7 (O).

The data for the highest TMOS concentration studied is ambiguous, since although a diffraction peak developed in this sample the peak shape was square rather than sharp and it evolved over a short time and remained constant and relatively low in intensity thereafter. Possibly in this sample the high concentration of TMOS accompanied by the high evaporation rates at 36°C prevented full ordering by freezing in the structure through silica condensation before the methanol in the surface film fully evaporated. From the calculated evaporation rates (see Table 4.1) it is clear that the evaporation is slowest from the solution with least TMOS, and generally increases as

TMOS concentration increases, presumably due to the higher methanol levels present after TMOS hydrolysis. The samples at 7.2 TMOS/CTAB and 10.5 TMOS/CTAB do not however appear to fit the trend. In the case of ratio 7.2 this may be because of the high standard deviation in the %RH recorded for this sample.

The intensity fluctuations of the specular peak for this data as seen by Brennan *et al*[7] could potentially also be studied, however due to the extra noise induced in the patterns by the gas flow causing waves in the surface of the solution prior to solid film growth this method was less successful than under ambient conditions. Under ambient conditions ripples in the intensity of the specular peak indicating the formation of an unstructured thin film at the interface during the induction period were observed for films where the surface driven growth mechanism operated, but grew smaller in amplitude and fewer in number as the bulk driven mechanism became more dominant (see Figure 4.9).

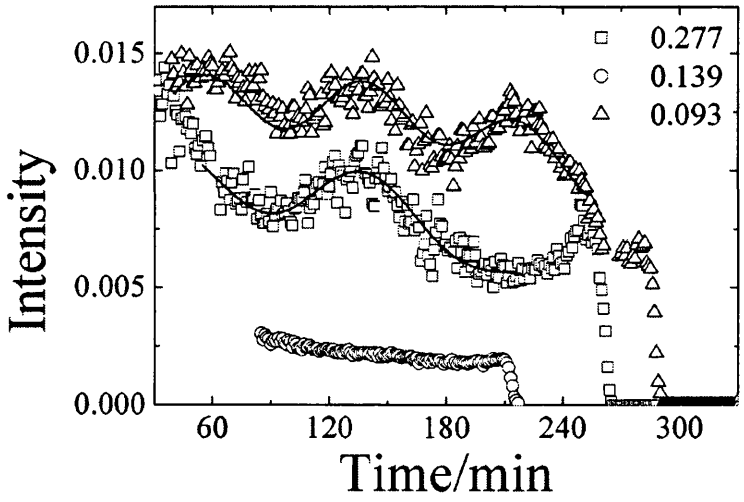

Figure 4.9. Plots of specular reflectivity peak intensities against time for three CTAB/TMOS molar ratios: 0.277 (or TMOS/CTAB= 3.6), 0.139 (or TMOS/CTAB= 7.2), and 0.093 (or TMOS/CTAB= 10.7) a t22°C and 50% RH.[7]

In the current data, some evidence of ripples is seen for all TMOS concentrations except the TMOS/CTAB ratio of 7.2, however they are very shallow and much more noisy than in the previous data so it is hard to draw any conclusions as to mechanism from this analysis.

4.3.4 Mesophase structures

In the off-specular data, further development of the film mesostructure after the formation of the first order diffraction peak is also observed. In most cases, at all temperatures studied, the intensity of the first order diffraction peak increases as the film grows, but then decreases again. This could be interpreted as a change in the nature of the scattering from diffraction rings, which intersect the plane of our detector and which are observed in the initially formed films, to diffraction spots which are observed by GIXD[13] after the film has formed and completed the ordering of the mesostructure. The diffraction spots for the first order peak are located slightly off the perpendicular axis and so do not fall on our detector causing the first order peak to apparently disappear or at least to decrease in intensity as the ring contracts towards a spot. The second order peak generally remains visible, and often remains as a small arc in GIXD patterns allowing it to continue to intersect with the detector.

In the case of the high temperature, lower TMOS concentration films, restructuring of the mesophase is also observed. The first order diffraction peak is observed to begin to grow at one angle, and after some time, a second peak appears as a shoulder on the first, which continues to grow, as the first peak shrinks. The final film has either a final first order diffraction peak at the new angle, or, as the first order diffraction peaks decrease in intensity, two peaks instead of one. At TMOS/CTAB =3.3 (see Figure 4.10) the peak shifts from Q=0.143 $Å^{-1}$ (43.8Å) to Q=0.141 $Å^{-1}$ (44.5 Å) via a pronounced double peak at 126 minutes while a single second order peak grows in at Q=0.262 $Å^{-1}$. The second order peak is at lower spacing than expected from the position of the first order peak due to refraction effects in the film. This effect is generally observed for diffraction peaks in reflectivity profiles from multilayered films (e.g. Kim *et al*[14]). After this point the first order peak and second order move slowly to higher Q, with the first order reaching 0.152 $Å^{-1}$ (41.2Å) as the peak intensity decays. The second order peak becomes a double peak (Q= 0.279 and 0.284 $Å^{-1}$) at around 200 minutes after the solution was prepared, and at the same time a shoulder at Q= 0.147 $Å^{-1}$ appears on the first order peak (Q=0.152 $Å^{-1}$), however the decreasing peak intensity due to the effect mentioned above caused the experiment to be ended at this point.

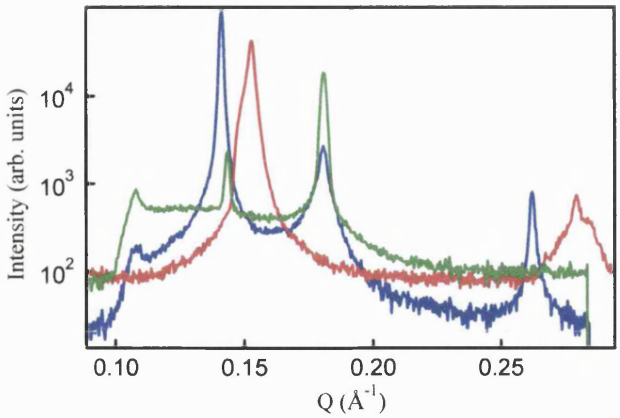

Figure 4.10. Diffuse reflectivity patterns for TMOS/CTAB = 3.3 showing patterns at 130 minutes (—), (b) 137 minutes (—) and (c) 217 minutes (—) after mixing.

At TMOS/CTAB = 5.3 (see Figure 4.11) the initial peak grows in at Q=0.142 $Å^{-1}$ with a second order at 0.264 $Å^{-1}$ but as the intensity of the first order decays, it shifts gradually to 0.150$Å^{-1}$ then back to 0.145 $Å^{-1}$. The second order peak in this case becomes a double peak at 0.272 and 0.277$Å^{-1}$ when the first order is at 0.150$Å^{-1}$. When the first order returns to 0.145 $Å^{-1}$ a second small peak grows in at 0.158 $Å^{-1}$. Finally the second order peaks merge leaving a final peak at 0.277$Å^{-1}$.

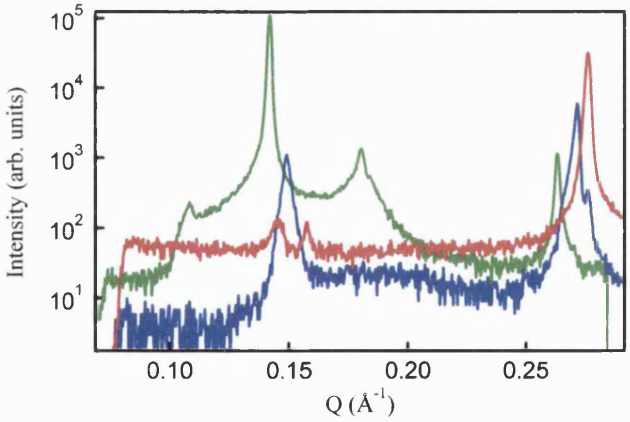

Figure 4.11. Diffuse reflectivity patterns for TMOS/CTAB = 5.3 showing patterns at 73 minutes (—), (b) 99 minutes (—) and (c) 109 minutes (—) after mixing.

At TMOS/CTAB =7.2 (see Figure 4.12) a shift of the first order peak from Q= 0.143$Å^{-1}$ to 0.140$Å^{-1}$ occurs via a double peak at 66 minutes. In this pattern a low intensity broad peak grows in next to the specular peak at Q=0.165$Å^{-1}$ while the second

order begins to grow at Q=0.262Å^{-1}. The first order becomes one peak at Q=0.141 Å^{-1} again by 71 minutes, the low intensity peak disappears and the second order peak moves to 0.264 Å^{-1}. At 94 minutes a second broad low intensity feature appears at 0.218Å^{-1}, which also disappears soon afterwards. At 94 minutes the pattern also contains a strong peak at 0.148 Å^{-1} with a shoulder at 0.145 Å^{-1}, and a second order at 0.273 Å^{-1}. In the final pattern as the intensity of the first order peak decreases, the peak splits, leaving two small peaks at 0.145 and 0.153Å^{-1} and an intense peak at 0.273Å^{-1}. At higher TMOS/CTAB ratios however the peaks do not significantly change position after they first form.

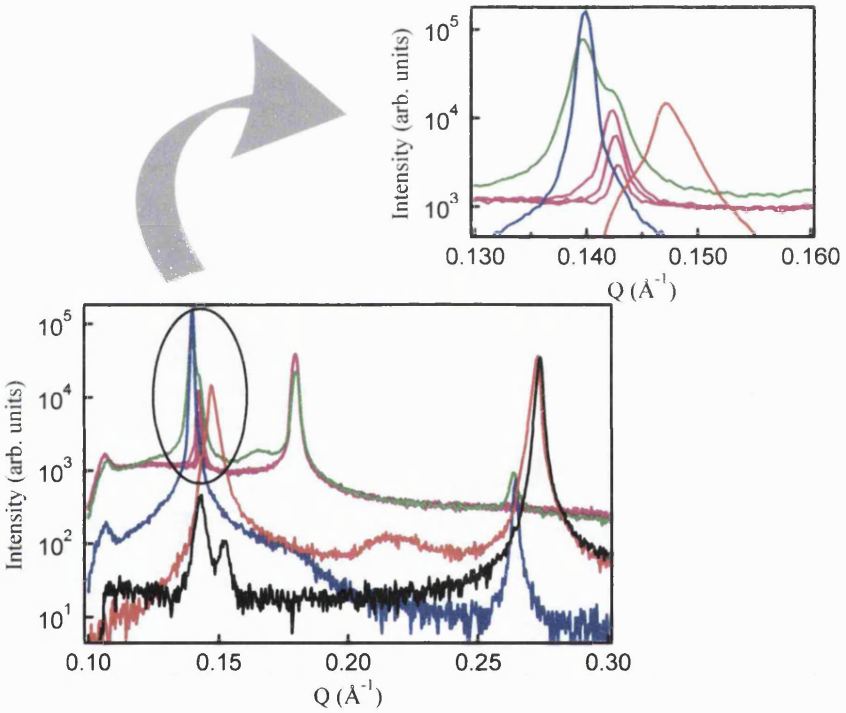

Figure 4.12. Diffuse reflectivity patterns for TMOS/CTAB = 7.2 showing patterns at: ~ 60 min (—) when the first diffraction peak starts to grow; 66 min (—); 71 min (—); 94 min (—); and 100 minutes (—) after mixing. The graph above shows a magnified first diffraction peak development.

Table 4.2. Changes in peak position given as Q value, for different TMOS/CTAB molar ratios at ~ 36 °C and ~ 50 % RH. Two intermediate structures were observed for TMOS/CTAB = 7.2.

TMOS/CTAB molar ratio	Initial structure (Å^{-1})		Intermediate structure (Å^{-1})		Final structure (Å^{-1})	
	1st order	2nd order	1st order[a]	2nd order[a]	1st order[a]	2nd order[a]
3.3	0.143		0.141	0.262	0.152 and 0.147	0.279 and 0.284
5.3	0.142	0.264	0.150	0.272 and 0.277	0.158 and 0.145	0.277
7.2	0.143	0.262	0.141[b]	0.264[b]	0.153 and 0.145	0.273
			0.148[b] and 0.145	0.273[b]		

[a] Peaks which developed through modulation of the original first and second order peaks.

[b] Two intermediate structures were observed sequentially for TMOS/CTAB) 7.2.

At all three TMOS/CTAB ratios where changes in peak position are observed, the final pattern can be indexed as belonging to a distorted cubic phase of the $Pm\bar{3}n$ type, similar to that seen by Che *et al*[12] for a powder preparation of mesoporous silica using cetyltriethylammonium bromide as the template in acidic conditions. As mentioned above, in the discussion of the results at high humidity, in that work a transition from the two dimension *p6mm* hexagonal phase to the $Pm\bar{3}n$ cubic phase was observed where the (10) peak of the hexagonal phase became the (211) peak of the cubic phase, so a similar transition may occur in these films. GIXD measurements on the in-plane structure of the films would be needed to unambiguously confirm this assignment. The initial phase with two peaks is likely (on the basis of our earlier work) to belong to the oriented two-dimensional hexagonal phase which forms with the long axis of the surfactant cylinders parallel to the interface. This phase then transforms as the surface dries out, and as the silica continues to polymerise, reducing the charge density of the silica interface with the surfactant. The surface drying, which will occur more rapidly at high temperatures, is probably the main driving force for rearrangement in these films since such rearrangements are not observed in films grown at lower temperatures, and as it will cause increased local charge density which typically causes the cubic phase to form. In the low temperature case the silica polymerization is sufficiently advanced to freeze in the initial hexagonal structure before the surface drying can affect the film structure.

4.4 Discussion

The use of a cell allowing for both humidity and temperature control, and the use of a precise surface technique such as diffuse X-ray scattering, can help to improve understanding of the self-assembly mechanism. When the film is grown at 100% humidity (Figure 4.3), the film grows without evaporation and a broad peak results, indicating a poorly ordered surfactant liquid crystalline structure. Decreasing the humidity results in the rapid formation of narrow diffraction peaks in the off-specular profile, consequently evaporation is necessary for ordering. During evaporation the water and methanol produced by TMOS hydrolysis are removed allowing a closer silica-surfactant approach, and contracting the silica network. As evaporation progresses the changing local concentration may promote dynamic transitions in the micellar phase, specifically from wormlike or disordered elliptical shapes to ordered cylinders[8]. However in the absence of evaporation a more disordered micellar phase results due to the higher surfactant solubility in this methanol. In some cases when the thin film is allowed to grow for a long time in a humid atmosphere the silica can become too condensed so that the disordered structure is frozen, and as a result sharp peaks do not develop when the humidity is reduced (experiment not shown). The time results for three different humidity stages (50, 70 and 100% RH), laid out in Figure 4.5 (a & b), confirm that the more evaporation, the faster the film mesostructure orders. High humidity overrides any other parameter that can alter the reaction, such as concentration and temperature, slowing down both the thin film growth and mesostructural ordering. For long reaction times at TMOS/CTAB=7.2 the specular peak is lower in intensity than that observed for TMOS/CTAB=10.7, suggesting greater surface roughness. In prior studies, films grown at TMOS/CTAB=7.2 develop via the formation of mesostructured particles in the bulk solution, which rise to the surface to form the film.[11] It is suggested that the rougher film observed here is also the result of these pre-formed particles at the surface, consisting of phase separated micelles and TMOS polymers. However at TMOS/CTAB= 10.7 molar ratio, individual silica coated micelles are formed which rise to the surface forming a smoother film, although with no observable mesostructural order. The Yoneda wing, which probes the surface roughness[11], appears sharper at 10.7 than at 7.2 molar ratio indicating that there is some surface roughness in the 10.7 molar ratio film. However if the amplitude of the surface roughness becomes too large the Yoneda intensity will decrease which may explain the less intense Yoneda wing at

TMOS/CTAB= 7.2. Increasing the temperature (Figure 4.7) improves the speed of the growth process owing to the faster evaporation and faster silica polymerization. High temperatures appear to extend the region where the surface-driven mechanism operates. Drying of the film under these conditions is faster than at ambient conditions and this may be responsible for the phase changes observed in the films at lower silica concentrations where the silica has not yet frozen in the initial mesostructure formed in the films.

4.5 Conclusions

The growth process and final structure of mesostructured silica-surfactant thin films depend on many factors. In this case, the effects of humidity, temperature, and inorganic precursor concentration were studied using off specular X-ray reflectivity and an enclosed cell providing humidity and temperature control. In general terms, high humidity slows down the growth processes due to the absence of evaporation. When the film is grown at 100% humidity, the film grows without evaporation and a broad peak results, indicating a poorly ordered surfactant liquid crystalline structure within the films. Decreasing the humidity by increasing the flow of air over the solution surface causes the opposite effect, resulting in a decrease in the film-formation time, as well as in a structural development into a well-ordered network. Humidity appears to have little effect on the formation mechanisms observed at different TMOS/CTAB ratios. Increasing the temperature improves the speed of the growth process, owing to the faster evaporation and faster silica polymerization, but also favors the surface-driven formation mechanism. The balance between evaporation from the surface, which causes ordering of the mesoscale structure, and formation of the rigid silica network, which traps that structure, determines the extent and type of structural ordering observed in the films.

4.6 References

(1) Huo, Q. S.; Margolese, D. I.; Ciesla, U.; Demuth, D. G.; Feng, P. Y.; Gier, T. E.; Sieger, P.; Firouzi, A.; Chmelka, B. F.; Schuth, F.; Stucky, G. D. *Chemistry of Materials* **1994**, *6*, 1176-1191.

(2) Brown, A. S.; Holt, S. A.; Dam, T.; Trau, M.; White, J. W. *Langmuir* **1997**, *13*, 6363-6365.

(3) Ruggles, J. L.; Holt, S. A.; Reynolds, P. A.; White, J. W. *Langmuir* **2000**, *16*, 4613-4619.

(4) Brown, A. S.; Holt, S. A.; Reynolds, P. A.; Penfold, J.; White, J. W. *Langmuir* **1998**, *14*, 5532-5538.

(5) Ruggles, J. L.; Gilbert, E. P.; Holt, S. A.; Reynolds, P. A.; White, J. W. *Langmuir* **2003**, *19*, 793-800.

(6) Edler, K. J.; Brennan, T.; Roser, S. J.; Mann, S.; Richardson, R. M. *Microporous and Mesoporous Materials* **2003**, *62*, 165-175.

(7) Brennan, T.; Hughes, A. V.; Roser, S. J.; Mann, S.; Edler, K. J. *Langmuir* **2002**, *18*, 9838-9844.

(8) Brennan, T.; Roser, S. J.; Mann, S.; Edler, K. J. *Chemistry of Materials* **2002**, *14*, 4292-4299.

(9) Wang, Y. L.; Kimura, K.; Dubin, P. L.; Jaeger, W. *Macromolecules* **2000**, *33*, 3324-3331.

(10) Edler, K. J.; Roser, S. J.; Mann, S. *Chemical Communications* **2000**, 773-774.

(11) Edler, K. J.; Goldar, A.; Hughes, A. V.; Roser, S. J.; Mann, S. *Microporous and Mesoporous Materials* **2001**, *44*, 661-670.

(12) Che, S. N.; Kamiya, S.; Terasaki, O.; Tatsumi, T. *Journal of the American Chemical Society* **2001**, *123*, 12089-12090.

(13) Brennan, T.; Dalgliesh, R. M.; Lovell, M. R.; Richardson, R. M.; Barnes, A. C.; Sergeant, S. A. *Langmuir* **2003**, *19*, 7761-7767.

(14) Kim, D. E.; Lee, S. M.; Jeon, I. J.; Yanagihara, M. *Applied Surface Science* **1998**, *129*, 531-535.

Chapter 5 Non-ionic Surfactant Templated Silica Thin Films

5.1 Introduction

Most of the work on silica mesostructures templated with non-ionic surfactants has been concerned with powders from hydrothermal syntheses using dilute solutions or monolithic samples synthesised via the true liquid crystal templating method with a high surfactant concentration.[1, 2] In 1995 Pinnavaia *et al.* prepared mesoporous materials using C_nH_{2n+1} NH_2 primary amines[3, 4] or alkyl poly(ethylene oxide)[5] as surfactants and tetraethyl orthosilicate (TEOS) as inorganic precursor in a neutral templating synthesis. These materials, designated as MSU-X, self-assemble through hydrogen bonding between the hydrophilic $(EO)_n$ segments in the case of polyethylene oxide surfactants and the silanol groups from the inorganic precursor.[5] The amphiphile complex induces the formation of rodlike micelles and the silanol groups encapsulate the self-assembled micelles producing a hexagonal structure. Attard *et al*[6] have reported several studies on mesoporous silica powders prepared through the true liquid crystal templating pathway by using Brij-type non-ionic alkyl poly(oxyethylene) surfactants, obtaining three liquid-crystal phases, hexagonal, lamellar and cubic. Some of these studies were based on electrodeposited mesoporous platinum films using octaethylene glycol monohexadecyl ether ($C_{16}EO_8$) as a non-ionic surfactant. These platinum films were one of the earliest mesoporous materials studied due to their optical properties and thermal stability.[7-9] A later synthesis of liquid crystal phases of mesoporous silicate materials has been also reported using Brij 56 ($C_{16}EO_n$, n ~ 10) as non-ionic surfactant and TMOS as silica precursor in a highly acidic media by Coleman *et al.*[10] A recent approach to the study presented in this thesis has been published by Hayward *et al.*[11] who synthesized thin films of bicontinuous cubic mesostructured silica using Brij 56 as a structure-directing agent by the method of dip-coating.

Since 1995 the use of non-ionic surfactants has constituted a new direction in the synthesis of mesoporous materials due to their properties. Non-ionic surfactants are inexpensive, non-toxic, and biodegradable in contrast to the cationic surfactants commonly and initially used for this kind of synthesis.[12] For this reason, this mesoporous silica thin films study is focused on this neutral surfactant templated system obtaining well-ordered films enabling comparison with previous cationic surfactant templated mesoporous silica thin films.

Therefore, this work covers the study of thin film evolution at the air-liquid interface using off specular x-ray reflectivity measurements and Brewster angle microscopy (BAM) for a non-ionic surfactant templated silica system. The structure of micelles in the bulk solution has also been analysed via small angle neutron scattering (SANS). These methods allow us to discuss the different mechanisms evident in the growth processes of the thin film at the air-liquid interface and the self assembly of micelles that happens in the bulk solutions from the very early reaction state to the very developed and ordered system.

A great number of SANS studies of single[13-17] and mixed[18-24] surfactant micelle structures in aqueous solutions using di and triblock copolymers and anionic and cationic surfactant, have been reported by Pedersen *et al.* They have presented useful form and structure factors and have identified a large diversity of micelles shapes. In addition not only SANS but also some small angle x-ray scattering (SAXS) studies have been performed to investigate formation mechanisms and mesostructure variations in mesoporous silica materials. Among these materials the MSU-X family,[25] synthesized by the addition of TEOS and non-ionic surfactant such as Tergitol 15-S-12 ($CH_3(CH_2)_{14}(EO)_{12}$), was proposed to form a three-layered micellar structure consisting of an alkyl core, a poly (ethylene oxide) (PEO) first shell, and a silica second shell. A micellar study by SAXS was also investigated for Brij-based mesostructured films using polydisperse non-ionic surfactant (Brij 58) prepared by evaporation-induced self-assembly.[26] They form 2D hexagonal cylindrical micelles in which a certain fraction of PEO groups are mixed with silica while the remaining majority rejects the silica matrix. Flodström *et al* have also reported studies based on SAXS technique regarding mesoporous silica materials such as SBA-15[27] formed by triblock copolymers, $(EO)_x$-$(PO)_y$-$(EO)_x$ (Pluronic types). They found that the EO-block length of the polymers determines the phase of the silica while the PO-block length has a great effect on the pore diameter.[27-29]

5.2 Experimental Procedure

5.2.1 Sample preparation

Silica-non-ionic surfactant templated thin films were prepared using octa-ethylene glycol mono n-hexadecyl ether ($C_{16}EO_8$) (BC-8SY, Nikko Chemicals, Japan) as the non-ionic surfactant and tetramethoxysilane (TMOS, Acros 98 %) as the silica precursor in acidic media (0.2 M HCl). $C_{16}EO_8$ is a surfactant with high monodispersity with respect to both the alkyl chain (C_{16}) length and the oxyethylene chain length (EO) and was used as a model surfactant similar to the commercial polydisperse polyoxyethylene surfactants.

Solutions were prepared by varying TMOS concentration at the following molar ratios:

1.5×10^{-3} $C_{16}EO_8$: 3.6×10^{-3} HCl: 1 water: X TMOS (see Table 5.1)

Table 5.1. TMOS molar ratios and its concentration fractions.

Molar relation	X
1/2	5.37×10^{-3}
1*	1.07×10^{-2}
3/2	1.64×10^{-2}

Samples are also expressed in TMOS/ $C_{16}EO_8$ molar ratios: 3.5, 7.1 and 10.8.

5.2.2 Scattering techniques

Off specular X-ray reflectivity was used as a surface characterisation technique. Variation of the peak intensity, peak position and peak shape are followed with time indicating film growth rate and providing some information on growth mechanism.[30, 31]

The incident angle, in GIXD, was kept constant and the linear detector records the scattering in Q_{xy} space scanning up to 5°.[35] Measurements were carried out using two different angles, mentioned in the results section, which allows investigation of the structures as a function of penetration depth for the same solutions used in the off specular X-ray reflectivity experiments.

Off specular X-ray reflectivity and GIXD measurements were carried out using an energy of 8.07 keV (λ =1.537 Å).

Neutron scattering experiments were performed using a range of wavelengths between 2.2 Å to 10 Å at 25 Hz to cover the scattering vector range of Q = 0.06 - 0.24 $Å^{-1}$ by time-of-flight method with a 4m sample to detector distance.[36, 37]

Time-evolution of structures in the bulk solution was studied for these molar ratios: 1.4×10^{-3} $C_{16}EO_8$: 3.6×10^{-3} HCl: 1 solvent: 1.1×10^{-2} TMOS.

As solvent three contrast variations of D_2O and H_2O were used: 100% D_2O, 60% D_2O 40% H_2O and 40% D_2O 60% H_2O. The cells were left open to allow evaporation to occur to mimic the same conditions as when the thin film grows at the air-liquid interface. 15 min patterns were collected alternately between 100 and 60% D_2O samples and 20 min patterns were measured for 40% D_2O samples until precipitate was formed. The characteristically long induction periods observed in acidic media allows collection of useful data on these time-scales.

5.3 Results

5.3.1 BAM studies

The growth of mesostructured silica thin films at the air-water interface was followed in real time by Brewster angle microscopy (BAM). The measurements were carried out for a wide range of TMOS/ $C_{16}EO_8$ molar ratios: 3.5, 5.3, 7.1, 8.9 and 10.8 (see Figure 5.1). Film development occurs in three stages: an induction period, a film development period, and a surface-consolidation period. Every sample shows clearly these three stages except 3.5 TMOS/ $C_{16}EO_8$ sample, which presents a long induction period (~ 6h.). The final film could not be recorded by BAM since, by that time, most of the solution evaporated. However, some time later, the film was observed by naked eye.

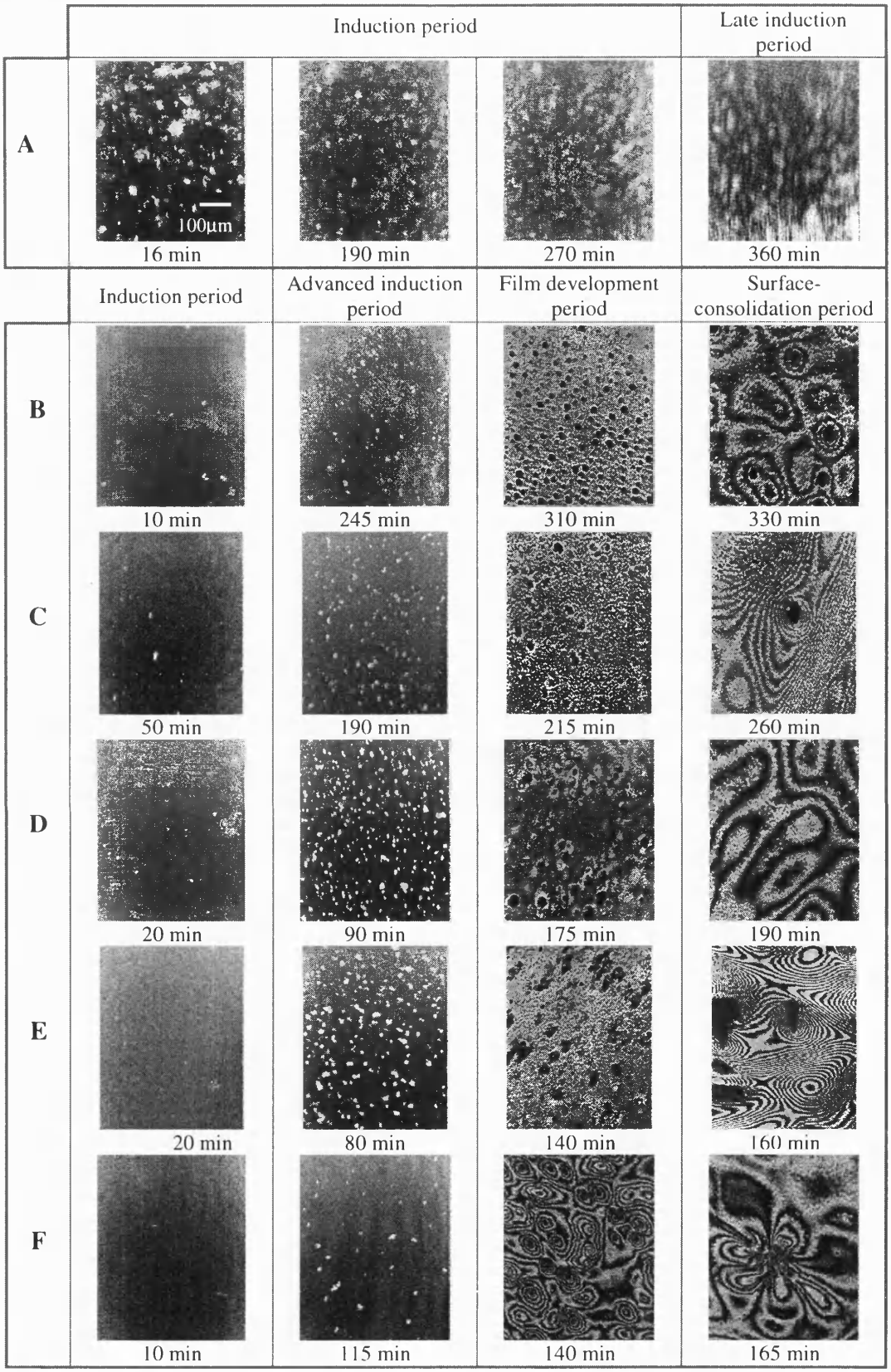

Figure 5.1. BAM pictures for TMOS/ $C_{16}EO_8$ (**A**) 3.5, (**B**) 5.3, (**C**) 7.1, (**D**) 8.9, (**E**) 10.8, and (**F**) 14.2 molar ratios collected at several formation times after mixing.

The induction period in BAM is characterised by the lack of solid domains. The image appears black where the surface of the liquid is visible and brighter in spot domains due to small local changes in the refractive index. During the film development period film growth occurs, eventually covering most of the interface. After further film development the film becomes continuous and develops interference fringes as shown in Figure 5.1. Thin films present a non-uniform image in which alternating bright and dark bands or lines are observed. This optical phenomenon occurs when interference occurs between the top, air-film interface and the bottom, film-solution interface. The beam reflects from the air-film interface and undergoes a 180° phase change when reflecting from the liquid film interface. The phase change is caused by the difference in the refractive index of the film, which is greater than that of the solution. The appearance of these fringes shows that the film surfaces are smooth and that the film is of roughly uniform thickness on a local scale. Samples B, C, D, E and F displayed in Figure 5.1 show an irregular fringe pattern, which indicates that the thin film surface is not optically flat across tens of microns.

These experiments show a decreasing behaviour of growth time as a function of silica concentration as shown in Figure 5.2. At higher concentrations the silica gels so no film growth is observed.

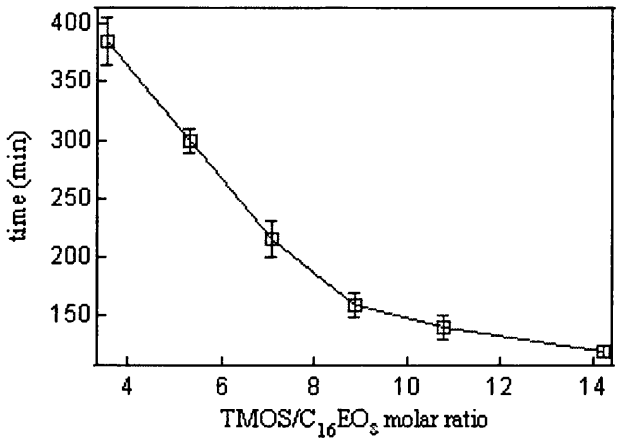

Figure 5.2. Film formation time in function of TMOS/ $C_{16}EO_8$ molar ratio obtained from BAM measurements.

5.3.2 *Off specular X-ray reflectivity studies*

Off specular experiments were carried out at three TMOS/ $C_{16}EO_8$ molar ratios, 3.5, 7.1 and 10.8 in order to understand the self-assembly behaviour of non-ionic surfactant-silica films. This is a gradual process involving three main growth stages, the induction period, the mesostructure development period and the surface-coarsening period thoroughly detailed in chapter 2 and further explained in the Brewster angle microscopy section above.

To understand how the silica concentration affects the formation time as well as to understand the growth mechanism we studied the off specular x-ray reflectivity profiles, displayed in Figure 5.3, which follow the mesostructure development. The profile as shown in the inset graph in Figure 5.3a consists of the Yoneda wing (a) and the specular reflectivity peak (d) corresponding with the clean surface observed in the period before the film is formed. Figure 5.3a shows the first and second diffraction peaks (b & e), which appeared 352 minutes after the TMOS was added into the surfactant solution. The presence of the specular peak in Figure 5.3a coexisting with the diffraction peaks suggests a relatively smooth film surface unlike that seen for films grown using CTAB as template.[38] The appearance of new diffraction peaks (c, f & g) in the 7.1 TMOS/ $C_{16}EO_8$ molar ratio profile, apart from b & e observed also in the 3.5 TMOS/ $C_{16}EO_8$ molar ratio profile, indicate the formation of a film with a different mesostructure.

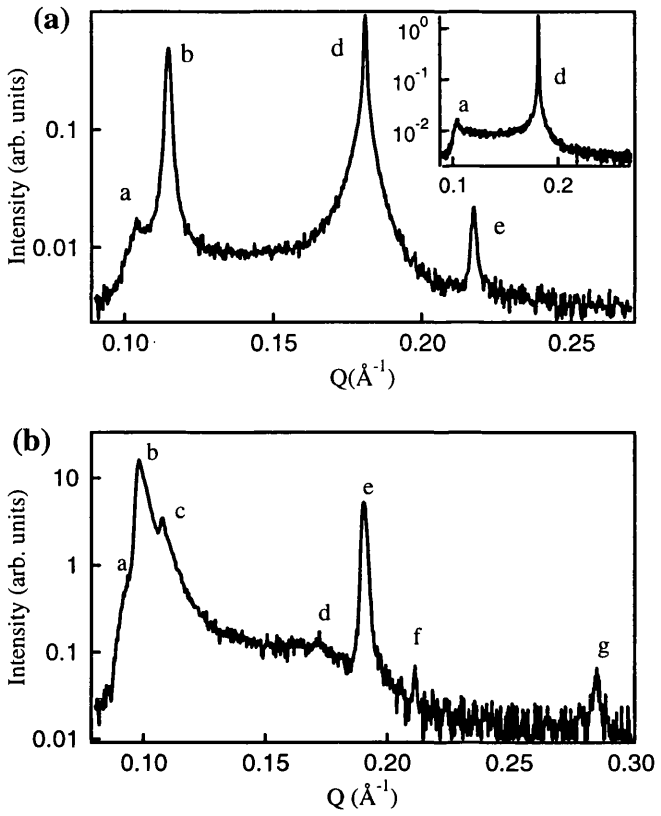

Figure 5.3. **(a)** Off specular profile for TMOS/ $C_{16}EO_8$ = 3.5 and **(b)** TMOS/ $C_{16}EO_8$ = 7.1 molar ratio both collected at the same time after peaks first appeared (352 and 332 minutes after TMOS addition respectively). The peaks are defined as: Yoneda wing (a); first diffraction peak (b); first diffraction peak shoulder (c); specular reflectivity peak (d); second diffraction peak (e) and new diffraction peaks (f and g). The inset graph in **(a)** shows the clean solution surface during the induction period with the presence of the Yoneda wing and the specular reflectivity peak.

Table 5.2. *Q* values gave in Å^{-1} of the peaks corresponding to Figure 2a and 2b.

TMOS/ $C_{16}EO_8$	Yoneda	1st diff. Peak	Specular Peak	2nd diff. Peak	Additional Peaks
3.5	0.1	0.11 Å^{-1} (57.12 Å)	0.18 Å^{-1}	0.22 Å^{-1} (28.56 Å)	—
7.1	Hidden by 1st diff peak	0.10 Å^{-1} (62.83 Å)	0.18 Å^{-1}	0.20 Å^{-1} (31.41 Å)	c: 0.12 Å^{-1} (52.36 Å) f: 0.22 Å^{-1} (28.56 Å) g: 0.29 Å^{-1} (21.66Å)
10.8	0.096	0.10 Å^{-1} (62.83 Å)	0.18 Å^{-1}	0.20 Å^{-1} (31.41 Å)	—

There is no evidence of additional peaks at TMOS/ $C_{16}EO_8$ = 3.5 and 10.8 ratios as seen at the 7.1 molar ratio.

The diffraction peaks in Figure 5.3a show the mesostructural definition of the thin film, which forms a 2D hexagonal or lamellar structure. However the presence of

overlapping and additional peaks in Figure 5.3b could suggest that a different structure is formed. GIXD measures the structures of these thin films more accurately (see GIXD results below).[35]

Plotting time to appearance of 1st order diffraction peak against TMOS/ $C_{16}EO_8$ ratio, as shown in Figure 5.4, a faster film formation is observed as the TMOS/ $C_{16}EO_8$ molar ratio increases. This result agrees with the previous BAM results shown in Figure 5.2).

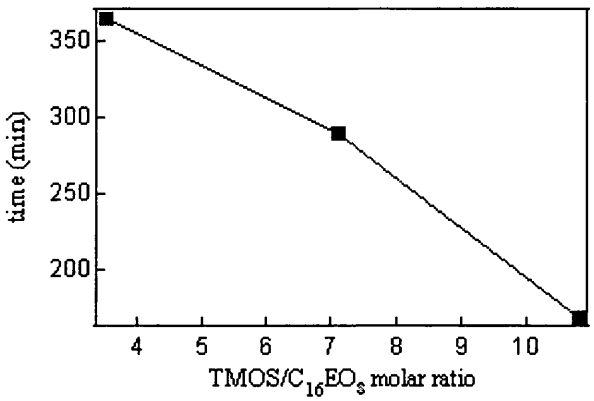

Figure 5.4. Film formation time for TMOS/ $C_{16}EO_8$ molar ratio obtained from off specular X-ray reflectivity and BAM measurements.

However different film formation times measured by BAM and by off specular reflectivity have been observed (see Table 5.3). The temperature and humidity during BAM experiments were ~27°C and RH < 50%, however during off specular measurements T ~ 25°C and RH = 50%. Faster film formation occurred for 7.1 and 10.8 TMOS/ $C_{16}EO_8$ molar ratios when obtained by off specular reflectivity since increasing the humidity and decreasing the temperature slows down the thin film formation, as discussed in chapter 4.

Table 5.3. Formation times for two TMOS/ $C_{16}EO_8$ molar ratios obtained from BAM and off specular reflectivity measurements.

TMOS/ $C_{16}EO_8$	BAM (min)	Off-spec. (min)
7.1	215	290
10.8	140	168

To understand the mechanisms of the thin film formation the variation of the full width half-maximum (FWHM) for the first diffraction peak with time is studied (see

Figure 5.5). The three TMOS/ $C_{16}EO_8$ molar ratios studied showed different peak-width behaviours. The peak-width is characteristic of ordering since it is inversely proportional to the number of repeat units as described by the Scherrer equation (see chapter 3).[38, 39] For TMOS/ $C_{16}EO_8$ = 3.5 the peak starts broad and becomes narrower with time. In this case the mesoscale ordering starts with small domain sizes increasing with time on the surface. For TMOS/ $C_{16}EO_8$ = 10.8 molar ratio the peak-width behaves oppositely to the 3.5 molar ratio one suggesting a change in the mechanism of the film growth. Initially micelles aggregate in solution and become larger ordered domains before reaching the interface. For the ratio TMOS/ $C_{16}EO_8$ = 7.1 a random peak-width behaviour from 290 to 316 minutes is observed due the presence of two peaks overlapping at the first diffraction position shown in Figure 5.3 (peaks b & c). It is therefore not possible to draw any conclusions about the formation mechanism of the film at this ratio from the off specular diffraction alone.

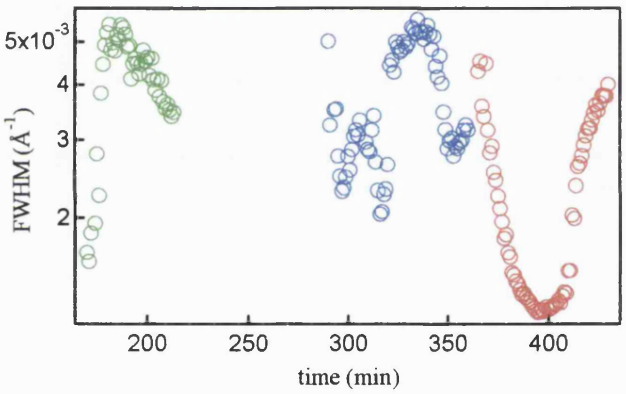

Figure 5.5. Peak width (FWHM) variation of the first diffraction peak from the off specular reflectivity patterns against time at three different TMOS/ $C_{16}EO_8$ molar ratios: ○ TMOS/ $C_{16}EO_8$ = 3.5; ○ TMOS/ $C_{16}EO_8$ = 7.1; ○ TMOS/ $C_{16}EO_8$ =10.8.

5.3.3 GIXD studies

Grazing incident X-ray diffraction was carried out with an incident angle at 0.13° and a second angle (0.74° or 0.82°), which corresponds to the position in degrees of the 1st diffraction peak measured during the specular reflectivity. These patterns shown in Figure 5.6, 5.7 and 5.8 were recorded at the higher angles, which allow obtaining measurements from lower sections of the film. They were obtained from the same films as were used for the off specular X-ray reflectivity analysis.

In the TMOS/ $C_{16}EO_8$ = 7.1 and 10.8 patterns (Figure 5.7 & 5.8) we measured the specular reflectivity curve after the off-specular measurements and after that we measured the GIXD, hence these films had time to finish forming and had reached stable structures. For the TMOS/ $C_{16}EO_8$ = 3.5 pattern, the film appears to have continued to develop during the GIXD measurement. It has been indexed to a 2D rectangular or distorted 2D hexagonal structure as predicted by the off specular pattern, shown in Figure 2a. However the position of [11] and [31] peaks in this pattern belong to a slightly larger unit cell, which was contracting during the measurement. Since there are ~ 30 min between measurements of these peaks, those at higher angles, the film had time to continue to evolve before these peaks were measured. In the TMOS/ $C_{16}EO_8$ = 7.1 the diffraction spots indicate a cubic phase $Pm\bar{3}n$ with a cubic cell spacing of a = 132.5 Å. This 7.1 pattern seems to have two crystals one slightly offset in angle. The GIXD pattern for the TMOS/ $C_{16}EO_8$ = 10.8 suggest that the structure of the film is a micellar body-centred cubic ($Im\bar{3}m$) mesophase with a = 85.6 Å.

Consequently the structure changes from 2D hexagonal to cubic as TMOS/ $C_{16}EO_8$ molar ratio increases. Increasing silica concentration increases the area occupied by EO and SiO_2 in the shell and so as expected a micellar transition from cylinders to spheres occurs, changing the structure from 2D hexagonal to cubic.

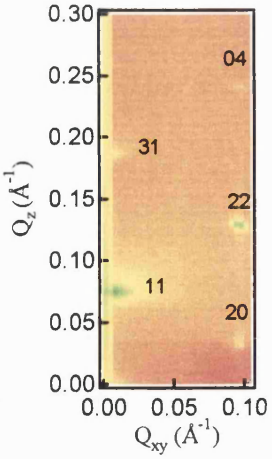

Figure 5.6. Two-dimensional GIXD plot for a TMOS/ $C_{16}EO_8$ = 3.5 molar ratio after 8.5 h. Incident angle 0.82°.

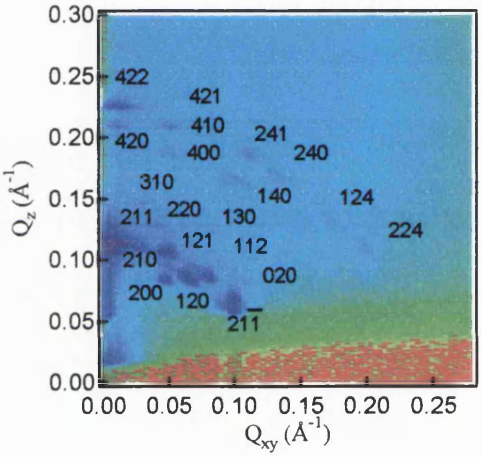

Figure 5.7. Two-dimensional GIXD plot for a TMOS/ $C_{16}EO_8$ = 7.1 molar ratio after 9.25 h. Incident angle of 0.74° in (b).

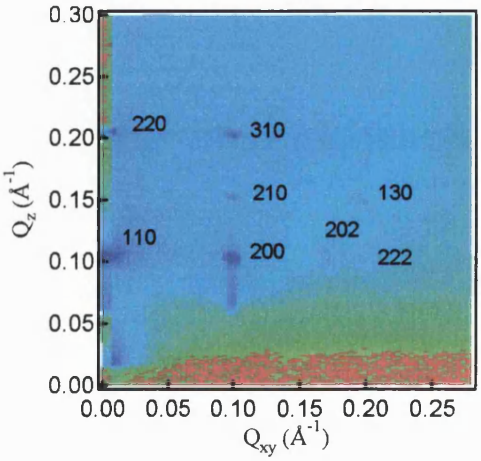

Figure 5.8. Two-dimensional GIXD plot for a TMOS/ $C_{16}EO_8$ = 10.8 molar ratio after 3.75 h with an incident angle of 0.82°.

5.3.4 *SANS studies*

SANS records the *in situ* evolution of the micelles in the bulk solution at three D_2O/ H_2O contrasts as a function of time. Figure 5.9 shows this bulk evolution for patterns taken until a precipitate appears in the cell, forming a large-scale structure. The growth of the peak (Q = 0.107 $Å^{-1}$) characterises a well-ordered mesophase structure related to the presence of the precipitate as well as to the formation of the thin film at the air-liquid interface.

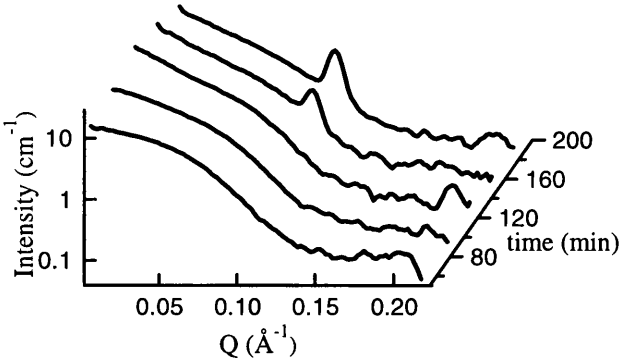

Figure 5.9. SANS profile for TMOS/ $C_{16}EO_8$ = 7.1 molar ratio showing the evolution of structure in the bulk solution with time for 100% D_2O contrast.

From Figure 5.9 the mesostructure formation time was defined according to the appearance of the peak (~163 min.). This point was designated "100% film formation", since the appearance of the film at the surface occurs at the same time as formation of precipitate in the bulk solution. Also the *d* spacing of the peak is the same as the spacing of the 1st order peak in the films.

In the initial stages of the reaction the micelles undergo a gradual change in shape from (pseudo) spherical or ellipsoidal to cylindrical with time. The period between induction and film development described by BAM studies was assigned to 40% and 60% formation in the SANS patterns. During this time the micelles could be fitted to core/shell ellipsoidal shapes, as illustrated in Figure 5.10.

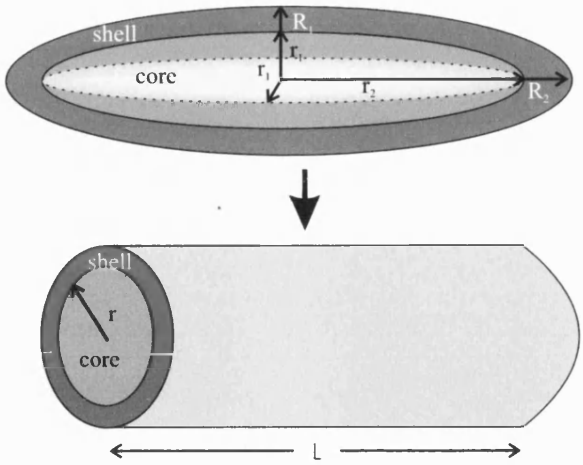

Figure 5.10. The top schematic drawing corresponds with the prolate-ellipsoidal shape for a hybrid micelle object where R is the micelle radius and r is the core radius (subscripts 1 and 2 refers to the minor and major radius respectively). The bottom corresponds with the core-shell cylinder model where r is the cylinder core radius and L is the cylinder length.

The 80% formation pattern was attributed to the mesostructure development period and 100% formation to the final mesostructure formation. For 40 and 60% formation SANS patterns were fitted using a monodisperse prolate ellipsoid particle model (see Figure 5.11a & b) and for 80 and 100% formation the patterns were fitted following the cylindrical particle model (see Figure 5.11c & d) since at this stage fits to an ellipsoidal shape were no longer satisfactory. Both models use a core/shell form factor ($P(Q)$) in combination with a hard-sphere interparticle structure factor ($S(Q)$). In prior surfactant templated silica film studies using cetyltrimethylammonium bromide (CTAB) as cationic surfactant and TMOS as silica precursor the Hayter Penfold MSA[40, 41] was used as the structure factor, which allows the interparticle interference effects due to the coulomb repulsion between the positive charged CTAB micelles in solution.[35] Since the surfactant involved in this system is non-ionic ($C_{16}EO_8$) and therefore, considering that the interaction between the two species (surfactant-silica) is due in greater part to hydrogen bonding, rather than electrostatic interactions, the hard-sphere structure factor was chosen.

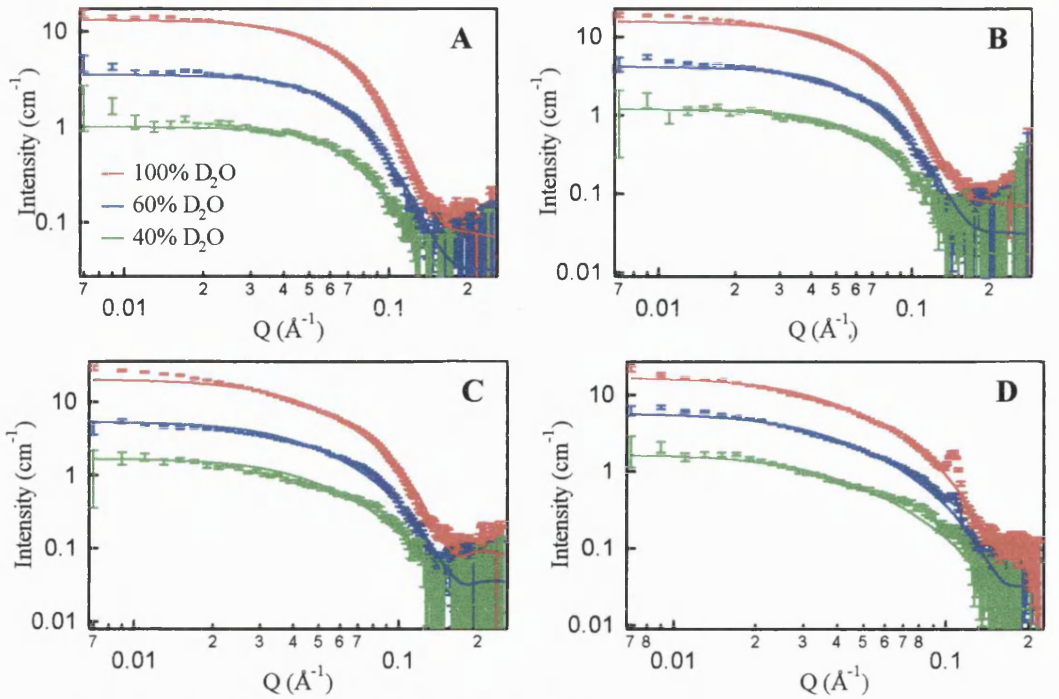

Figure 5.11. SANS fitting profile for 3 D_2O/ H_2O contrast for A) 40%, B) 60%, C) 80% and D) 100% formation.

The self-assembly in this system involves both surfactant reorganization within the micelles and the hydrolysis and condensation of TMOS in an acidic media (pH< 2) generating silica oligomers[42] which polymerise with time. Silica reacts with the surfactant micelles affecting their shape and composition. It suggested that in the micelles the hydrophobic alkyl chains form the core whereas the shell is thought to consist of an assembly of hydrophilic ethylene glycol chains with silica and a small quantity of solution. Micelles are surrounded by a solution consisting mainly of water and/or D_2O with HCl and methanol that has been generated by the silica hydrolysis.

During the fitting the $P(Q)$ contributes to the single scattering particle amplitude obtaining the scattering length densities (ρ) of the core, shell and solvent. The $S(Q)$ is characterized by the volume fraction which deceases with time since after formation the particles are prone to precipitate. The ρ_{core} was fixed at -3.51×10^{-7} Å^{-2} over all the different scattering patterns and the ρ_{shell} and $\rho_{solvent}$ values, which depend on the variation in the D_2O/H_2O contrast were allowed to have some degree of freedom. The fitted $\rho_{solvent}$ agrees with the theoretical values at the three D_2O/H_2O contrasts being $\sim 6.0 \times 10^{-6}$ Å^{-2} for 100% D_2O, $\sim 3.5 \times 10^{-6}$ Å^{-2} for 60% D_2O and $\sim 1.9 \times 10^{-6}$ Å^{-2} for 40%

D_2O. The ρ_{shell} values depend on the amount of hydration in the shell as well as the silica density as it condenses.

Results obtained from the fitting in Figure 5.11 are shown in Table 5.4. As time increases the micelles rearrange forming highly elongated ellipses as the major radius core (r_2) shows, which lengthen along the X-axis while remaining fixed in width along the Y-axis (r_1). Shell thickness decreases with time since as silica hydrolyses and condenses the shell shrinks. During the core-shell cylinder fitting the cylinder length (L) elongates from 80% to 100% formation. In both models the shell thickness (t) is considered to be uniform over the entire surface of the core.

Table 5.5 shows the shell scattering length density decreases with time at the three D_2O/H_2O contrasts since there is a reduction in the amount of solvent present in the shell. Likewise there is a decrease in the solution values of the scattering length density possibly due to silica migration to the shell and also precipitation of silica in disordered material found in the bottom of the cell.

Table 5.4. Values of structural parameters obtained from Prolate-HS and Core-shell Cylinder-HS models at four different time formations.

	Time	t(Å)	r_1	r_2	L(Å)
Prolate-HS	40%	12	20	57	—
	60%	11	20	68	—
Core-shell Cylinder-HS	80%	8	20	—	142
	100%	8	20	—	162

Time is the time of formation considering 100% to be when the first diffraction peak grows; t is the shell thickness; r_1 is the minor and r_2 is the major core radius; L is the cylinder core length; r is the core cylinder radius. The error in the fit parameters was ± 1 Å except for L, which is ± 5 Å.

Table 5.5. Values of scattering length densities (ρ) obtained from Prolate-HS and Core-shell Cylinder-HS models at four different time formations.

		ρ_{shell} ($\times 10^{10}$cm^{-2}) in "X" %D_2O			$\rho_{solution}$($\times 10^{10}$cm^{-2}) in "X" %D_2O		
	Time	**100**	**60**	**40**	**100**	**60**	**40**
Prolate-HS	40%	3.8	2.75	1.9	6.03	3.58	2.14
	60%	3.7	2.72	1.89	6.03	3.58	2.14
Core-shell Cylinder-HS	80%	3.68	2.65	1.85	6.03	3.43	2.05
	100%	3.67	2.65	1.84	5.74	3.55	2.04

The standard deviation errors are close to ± 0.005×10^{10}.

5.4 Discussion

Off-specular X-ray reflectivity shows how silica concentration affects the film time formation as well as suggesting the growth mechanism. Time resolved measurements show a faster film formation as TMOS/$C_{16}EO_8$ molar ratio increases (see Figure 5.2 and 5.4) unlike TMOS/CTAB system, which follows a "horse-shoe" time dependence.[38, 43]

A study of the peak-width behaviour of the growing first order diffraction peak provides information about the growth mechanism distinguishing two possibilities, the bulk-driven and surface-driven mechanisms. Combining SANS and off-specular results suggests that at 10.8 and 7.1 TMOS/ $C_{16}EO_8$ molar ratios a possible bulk-driven mechanism occurs, corresponding with the shortest film formation times. During this formation regime the majority of the micelles aggregate into a large ordered domains in the bulk before they diffuse to the interface.[38] In the case of 7.1 TMOS/ $C_{16}EO_8$ molar ratio sample the appearance of the FWHM could suggest development close to a bulk driven mechanism although it is hard to say due to the existence of overlapping peaks in the same Q area as the first diffraction peak. The appearance of a peak in the SANS for 7.1 molar ratio, as shown in Figure 5.9, suggests development of an ordered mesophase in solution. This together with the behaviour of the 1st order peak FWHM corroborate the possible bulk-driven mechanism for the 7.1 molar ratio sample. At the lowest TMOS/ $C_{16}EO_8$ molar ratio the FWHM behaviour suggests this film develops via a surface-driven mechanism where the accumulation of silica-coated micelles take place at the surface, producing broad peaks due to an initially small domain size which increases in size with time. Hence the film in this mechanism nucleates at the air-water interface and grows downward into the solution with time. At the end of the film formation the three TMOS/ $C_{16}EO_8$ molar ratios show very similar peak-width range (see the red circles in Figure 5.5) suggesting similar final domain sizes and corresponding with the surface-consolidation stage. Previous investigations on CTAB-templated silica mesoporous thin films using off-specular X-ray reflectivity show a different TMOS/ surfactant molar ratio effect upon the formation mechanisms. It was found that for 7.2 TMOS/ CTAB molar ratio the film formation mechanism appears to be bulk-driven. However unlike TMOS/ $C_{16}EO_8$ system the lowest and highest TMOS/ CTAB molar ratios, which correspond with longer development period (horse-shoe shape), follows a surface-driven mechanism.[38] In the case of these acidic solutions when

silica polymerizes it acts as a branched polyelectrolyte, which interacts with the charged surfactant micelles. During the bulk-driven mechanism a liquid-liquid phase separation, called coacervation,[44] permits particles to aggregate in the bulk solution due to charge neutralization over a narrow range of concentrations.

Charge neutralisation does not occur at low or high concentrations of polyelectrolyte, which is relatively alike to the TMOS/ CTAB system since the interaction between a similar TMOS-CTAB charge is mediated by the bromide counterion.[38, 44, 45] So similarly at high and low TMOS/ CTAB ratios particle formation does not occur and all film growth is surface driven. For TMOS/ $C_{16}EO_8$ system the main interaction between silica and non-ionic surfactant is not electrostatic but hydrogen bonding or hydrophobic interaction; hence the formation mechanism at high TMOS/ $C_{16}EO_8$ molar ratio does not correspond to the low TMOS/ $C_{16}EO_8$ molar ratio one. In the case of $C_{16}EO_8$ the micelles are stabilized not by electrostatic repulsion but by steric hindrance of the EO chains protruding from the micelle surface. Thus in this case, once enough silica is present to coat the micelles they alter from repulsive interactions to "sticky" attractive forces between the coated particles. Hence there are no over charging effects to prevent coacervation at high SiO_2 concentrations as occurs in the case of ionic micelles. Thus in the TMOS/ $C_{16}EO_8$ system a bulk driven mechanism is observed for all concentrations above that where the micelles are completely coated, and the reaction speeds up with increasing SiO_2 content since the micelles simply become coated faster. Possibly coacervation is not observed at low TMOS concentrations since it cannot form polymers with high enough molecular weight to cause coacervation before film formation occurs.

Focusing on SANS measurements, initially there is no long range ordering of the micelles either in the solution or at the surface (Figure 5.9). As time increases the micelles rearrange forming highly elongated ellipses in solution, which lengthen along the X-axis while remaining fixed in width along the Y-axis (Figure 5.10) and become cylinders. Similar SANS studies were carried out based on TMOS/ CTAB = 7.2 molar ratio system by Brennan *et al.*[46] The micellar evolution is very alike to this current work, however due to the positively charged CTAB head group, which is smaller than the PEO head group, the shell thickness is smaller.[46] The presence of the diffraction peak observed in SANS indicates that micelles first assemble into particles in the solution, diffusing to the surface to form the film. Scattering length densities, radii and

shell thicknesses allow us to calculate the molar concentration distribution of every species, which confine the core and shell of the micelle as well as the solution.

Firstly we calculated the ellipsoid-core volume occupied by the hydrophobic tail in 2.5cm^3 for 40% formation (the values are practically the same values for 60% formation).

Table 5.6. Main parameters of $C_{16}EO_8$ split into the hydrophilic head group (EO = octaethylene glycol) and the hydrophobic tail (C_{16} = hexadecane).

	$C_{16}EO_8$	EO	C_{16}
MW (g/mol)	594	369	225
d (g/cm^3)	—	1.13	0.773
ratio	—	0.62	0.38

Since the prolate-ellipsoid is the result of the short axis rotation giving two equal-dimensioned minor radius and one major radius (see Figure 5.10), the formula for the volume of the ellipsoid-core is

$$V_{ellipsoid-core} = \frac{4}{3}\pi r_1^2 r_2 \qquad 5\text{-}1$$

Therefore the volume occupied by a micelle core using the minor and major core radius given in Table 2 is 9.4×10^{-20} cm^3. To prepare a 2.5cm^3 silica-surfactant solution 1.68×10^{-4} moles of $C_{16}EO_8$ were added corresponding to 3.78×10^{-2} g of tail (C_{16}) (using Table 5.6), which occupies 4.88×10^{-2} cm^3 in the whole solution. With these two volume results the total number of micelles in the sample is easily calculated in the next equation:

$$\frac{V_{all\ cores\ in\ solution}}{V_{ellipsoid-core}} = 5.2 \times 10^{17} \qquad 5\text{-}2$$

Secondly the hybrid silica-surfactant micelle volume is calculated by equation 5-3 is 2.8×10^{-19}cm^3 bearing in mind the shell thickness.

$$V_{hybrid\ micelle} = \frac{4}{3}\pi (r_1 + t)^2 (r_2 + t) \qquad 5\text{-}3$$

Thus, the volume of the shell in the micelle is given by

$$V_{hybrid\ micelle} - V_{ellipsoid-core} = 1.9 \times 10^{-19}\,\text{cm}^3 \qquad 5\text{-}4$$

Multiplying the shell volume by the number of micelles we work out the volume occupied by the shell in 2.5 cm^3, which is 9.8×10^{-2} cm^3. And following the same procedure for the hybrid micelle we get a volume of 0.15 cm^3. Subtracting this last value from 2.5 cm^3 we can find the volume of the solution to be 2.35 cm^3.

Silica, D2O and the hydrophilic ethylene oxide groups constitute the shell. Hence the shell volume can also be written as

$$V_{shell} \times No.micelles = V_{SiO_2} + V_{EO} + V_{D_2O} = 9.8 \times 10^{-2} \text{cm}^3 \qquad 5\text{-}5$$

A density study for $C_{12}E_j$ non-ionic micellar solutions was carried out by Maccarini *et al* [47] which provides the molar volume per EO units for $C_{12}E_8$ (same number of EO units as $C_{16}EO_8$) at 28°C being 38.8 cm^3/mol. Therefore the volume occupied by eight octa-ethylene glycol groups (EO) is 5.15×10^{-22} cm^3 and to work out the volume the 8EO groups occupied in the shell of one micelle it is necessary to know how many surfactant molecules are in one micelle. Since we know the volume of the core ($9.4 \times 10^{-20} cm^3$) the tail volume in the core is easily calculated bearing in mind the molecular weight and density, shown in Table 5.6, being 4.83×10^{-22} cm^3.

$$Surfactant\ molecules\ in\ a\ micelle = \frac{V_{core}}{V_{tail}} = 194$$

Then, the V_{EO} in the shell of one micelle is $194 \times 5.15 \times 10^{-22} = 1.0 \times 10^{-19}$ cm^3. Multiplying this result by the number of micelle there are in the sample (5.2×10^{17}) the total V_{EO} is 0.052 cm^3.

Working out equation 5-5, silica volume is expressed as function of D_2O

$$V_{SiO_2} = 4.6 \times 10^{-2} - V_{D_2O} \qquad 5\text{-}6$$

The same procedure for volume calculations is followed for 60% formation, but at 80 and 100% formation the species develop towards cylinders, therefore the volume is the one occupied by cylinders.

$$V_{hybrid\ cylinder} = \pi(r+t)^2 \times L \qquad 5\text{-}7$$

$$V_{cylinder-core} = \pi(r)^2 \times L \qquad 5\text{-}8$$

The difference between equation 5-7 and 5-8 would give the volume occupied by the shell-cylinder:

$$V_{cylinder-shell} \times No.micelles = V_{SiO_2} + V_{EO} + V_{D_2O} \qquad 5\text{-}9$$

At 80% formation the shell volume is 0.086 cm^3 and at 100% formation is 0.096 cm^3.

The same volume expression as equation 5-5 gives the solvent volume, which is made up by D_2O, HCl, CH_3OH as a silica hydrolysis product, and part of the SiO_2.

$$V_{solvent} = V_{D_2O} + V_{HCl} + V_{CH_3OH} + V_{SiO_2} = 2.39\ cm^3 \qquad 5\text{-}10$$

The scattering length density for the core, shell and solvent are:

$$\rho_{core} = \frac{1}{m}[m\ \rho_{HEX}] \qquad 5\text{-}11$$

$$\rho_{shell} = \frac{1}{a+b+c}[a\ \rho_{SiO_2} + b\ \rho_{D_2O} + c\ \rho_{EO}] \qquad 5\text{-}12$$

$$\rho_{solvent} = \frac{1}{w+x+y+z}[w\ \rho_{D_2O} + x\ \rho_{HCl} + y\ \rho_{CH_3OH} + z\ \rho_{SiO_2}] \qquad 5\text{-}13$$

where m is the number of moles of the hydrophobic tail (HEX) in the core; a, b, and c correspond with the moles there are in the shell for SiO_2, D_2O, and the hydrophilic part (EO), respectively; and the moles of solvent are w, x, y, and z corresponding with the species D_2O, HCl, CH_3OH, and SiO_2, respectively.

Table 5.7. Calculated scattering length densities for every species

ρ(cm^{-2})					
C_{16}	EO	SiO_2	D_2O	HCl	CH_3OH
-3.51×10^9	5.61×10^9	3.49×10^{10}	6.37×10^{10}	1.16×10^{10}	-3.73×10^9

Assuming that the core is formed just by the surfactant hydrophobic part m = 1 and thereby $\rho_{core} = \rho_{C_{16}} = -3.51\times 10^9\ cm^{-2}$ (see Table 5.7).

Once we know each species volume the number of moles can be worked out through the density:

$$a = \frac{d_{SiO_2} \times V_{SiO_2}}{MW_{SiO_2}} \qquad 5\text{-}14$$

In the case of molar concentrations in the solvent we have to consider that the silica and methanol are stoichiometrically-related by the TMOS hydrolysis:

$$Si(OCH_3)_4 + H_2O \rightarrow SiO_2 + 4CH_3OH$$

Consequently four times total silica in the system is the amount of methanol in the solution: $y = 4(a + z)$. The moles of HCl are taken as the initial number of moles added in the sample preparation (4.48×10^{-4}).

Once the scattering length densities, radii and shell thickness have been obtained for every formation time, molar concentration distribution in the micellar system showed in Table 5.8 is calculated by equation 5-12 and 5-13, using the scattering length densities from Table 5.5 and 5.7. These molar concentration values shape the core, shell and solution and suggest how the molar distribution varies as the formation time increases.

Table 5.8. Molar concentration of every species in the shell and in the solution at the four formation times recorded in SANS.

Time	Shell			Solution			
	SiO_2	D_2O	EO	D_2O	HCl	CH_3OH	SiO_2
	a($\times10^{-3}$)	**b($\times10^{-4}$)**	**c($\times10^{-4}$)**	**w($\times10^{-1}$)**	**x($\times10^{-4}$)**	**y($\times10^{-3}$)**	**z($\times10^{-4}$)**
40%	1.31	3.59	1.59	1.18	4.48	5.86	1.57
60%	1.35	2.94	1.59	1.18	4.48	5.86	1.57
80%	1.36	2.81	1.59	1.18	4.48	5.86	1.57
100%	1.37	2.74	1.59	1.06	4.48	7.85	6.55

The neutral surfactant silica self-assembly in water occurs preferentially in the shell of the micelles where the process is catalysed via acidic media. The water or deuterated water molecules, which were bonded previously with the oxygen atoms of the ethylene oxide head-group, interact with the alkoxysilane precursor carrying out the hydrolysis. In this acidic solution (pH = 2) the hydrolysis gives the coexistence of two species, the neutral $[Si(OH)_4]^0$ and the positively charged $[Si(OH)_3(OH_2)]^+$. The interactions with the non-ionic surfactant could be expressed as $S^0[Si(OH)_4]^0$ by hydrogen or hydrophobic bonding and a possible electrostatic forces $S^0(OH)^-[Si(OH)_3(OH_2)]^+$.[48]

As the synthesis of $C_{16}EO_8$ templated mesoporous silica develops in time the silica concentration remains quite constant in the shell with a sudden increase at 100%

formation in the solution possibly due to the accelerated formation of SiO_2 during the final stages of coacervation (see the moles of SiO_2 in Table 5.8).

A formation mechanism for the siliceous mesoporous material, SBA-1, using cationic surfactant under acidic conditions, was investigated by Egger *et al.*,[49, 50] in which a reorganization of the precipitated phase results in a cubic phase final structure. In this system silica rearrangement during coacervation from the initial soft, poorly condensed phase to the final hard form resulted in the final arrangement of spherical and prolate ellipsoidal micelles in a cubic phase. Thus here once the micelles are incorporated in the film the increased silica density surrounding them may prompt a similar shape change from cylindrical micelles to ellipsoidal or spherical producing the finally observed cubic structure. An increase in SiO_2 around the micelle is suggested by the "shell SiO_2 concentration" value in the final SANS measurement and we assume that the incorporation of further SiO_2 around the micelles continues once the film starts to form.

It is also noticeable that D_2O concentration decreases in the shell due to a possible migration to the solution. The methanol obtained from the silica hydrolysis also increases in concentration with time.

Summarizing, different models were applied to fit SANS profiles covering a wide mesostructure formation time range. Thus prolate-ellipsoidal micelle model was used to fit the 40 and 60% formation times and the cylinder model for 80 and 100% formation times, both models with a core-shell form factor. From the SANS fitting, scattering length densities, radii and shell thickness were calculated for every formation time. These parameters allow us to study how the molar distribution in the different micellar parts varies with time. Some outstanding results are the loss of D_2O in the shell and the increase of silica in the solution due to the silica condensation and the solution evaporation as we mentioned above.

5.5 Conclusions

The self-assembly behaviour of non-ionic surfactant-silica films growing at the air-liquid interface in acidic solution has been studied using complementary surface and bulk techniques. Off-specular X-ray reflectivity results revealed how varying the silica concentration can affect the film formation times as well as the growth mechanisms. Thus, increasing silica concentration was found to produce a faster film formation. The growth mechanisms, which explain how the polymerized silica interacts with the surfactant micelles, were studied looking at the first diffraction peak-width profiles at 3.5, 7.1 and 10.8 TMOS/ $C_{16}EO_8$ molar ratios. For The 10.8 and 7.1 TMOS/ $C_{16}EO_8$ molar ratio samples a bulk-driven mechanism was suggested while a surface-driven mechanism was assigned for the 3.5 TMOS/ $C_{16}EO_8$ molar ratio one. The final thin film structures were determined by GIXD. A well-defined mesostructure was obtained observing a cubic phase $Pm\bar{3}n$ for 7.1 and a body-centred cubic phase ($Im\bar{3}m$) for 10.8 TMOS/ $C_{16}EO_8$ molar ratio films. However for the smallest molar ratio film the final structure was not well defined since the film needed more time to self-organize. The *in situ* evolution of the micelles in the bulk solution was also studied by SANS for the 7.1 TMOS/ $C_{16}EO_8$ molar ratio at three different D_2O/H_2O contrast variations. A gradual micellar evolution from (pseudo) spherical or ellipsoidal to cylindrical was observed applying a prolate-ellipsoidal with core-shell form factor fitting model. Molar concentrations values for every species distributed throughout the different parts of the micelles have been calculated form the experimental fitting parameters (scattering length densities, radii and shell thicknesses). This has allowed us to observe how the concentration changes in the core, shell and solution with time. Consequently, in the core, the concentration of the hydrophobic part of the surfactant remains constant. In the shell, the D_2O concentration decreases migrating to the solution, while the silica and the hydrophilic part of the surfactant concentrations remain practically constant. And finally the most significant increase with time occurs to the SiO_2 at the point of coacervation and the loss of methanol generated from the silica hydrolysis into solution as the hydrolysis and condensation reactions proceed.

5.6 References

(1) Beck, J. S.; Vartuli, J. C.; Roth, W. J.; Leonowicz, M. E.; Kresge, C. T.; Schmitt, K. D.; Chu, C. T. W.; Olson, D. H.; Sheppard, E. W.; McCullen, S. B.; Higgins, J. B.; Schlenker, J. L. *Journal of the American Chemical Society* **1992**, *114*, 10834-10843.

(2) Attard, G. S.; Glyde, J. C.; Goltner, C. G. *Nature* **1995**, *378*, 366-368.

(3) Tanev, P. T.; Pinnavaia, T. J. *Science* **1995**, *267*, 865-867.

(4) Tanev, P. T.; Pinnavaia, T. J. *Chemistry of Materials* **1996**, *8*, 2068-2079.

(5) Bagshaw, S. A.; Prouzet, E.; Pinnavaia, T. J. *Science* **1995**, *269*, 1242-1244.

(6) Attard, G. S.; Edgar, M.; Goltner, C. G. *Acta Materialia* **1998**, *46*, 751-758.

(7) Attard, G. S.; Bartlett, P. N.; Coleman, N. R. B.; Elliott, J. M.; Owen, J. R.; Wang, J. H. *Science* **1997**, *278*, 838-840.

(8) Gollas, B.; Elliott, J. M.; Bartlett, P. N. *Electrochimica Acta* **2000**, *45*, 3711-3724.

(9) Elliott, J. M.; Attard, G. S.; Bartlett, P. N.; Coleman, N. R. B.; Merckel, D. A. S.; Owen, J. R. *Chemistry of Materials* **1999**, *11*, 3602-3609.

(10) Coleman, N. R. B.; Attard, G. S. *Microporous and Mesoporous Materials* **2001**, *44*, 73-80.

(11) Hayward, R. C.; Alberius, P. C. A.; Kramer, E. J.; Chmelka, B. F. *Langmuir* **2004**, *20*, 5998-6004.

(12) Zhao, D. Y.; Huo, Q. S.; Feng, J. L.; Chmelka, B. F.; Stucky, G. D. *Journal of the American Chemical Society* **1998**, *120*, 6024-6036.

(13) Arleth, L.; Bergstrom, M.; Pedersen, J. S. *Langmuir* **2002**, *18*, 5343-5353.

(14) Derici, L.; Ledger, S.; Mai, S. M.; Booth, C.; Hamley, I. W.; Pedersen, J. S. *Physical Chemistry Chemical Physics* **1999**, *1*, 2773-2785.

(15) Mortensen, K.; Pedersen, J. S. *Macromolecules* **1993**, *26*, 805-812.

(16) Pedersen, J. S.; Hamley, I. W.; Ryu, C. Y.; Lodge, T. P. *Macromolecules* **2000**, *33*, 542-550.

(17) Pedersen, J. S.; Svaneborg, C.; Almdal, K.; Hamley, I. W.; Young, R. N. *Macromolecules* **2003**, *36*, 416-433.

(18) Bergstrom, M.; Pedersen, J. S. *Langmuir* **1998**, *14*, 3754-3761.

(19) Bergstrom, M.; Pedersen, J. S. *Journal of Physical Chemistry B* **1999**, *103*, 8502-8513.

(20) Bergstrom, M.; Pedersen, J. S. *Physical Chemistry Chemical Physics* **1999**, *1*, 4437-4446.

(21) Bergstrom, M.; Pedersen, J. S.; Schurtenberger, P.; Egelhaaf, S. U. *Journal of Physical Chemistry B* **1999**, *103*, 9888-9897.

(22) Bergstrom, M.; Pedersen, J. S. *Journal of Physical Chemistry B* **2000**, *104*, 4155-4163.

(23) Bergstrom, M.; Kjellin, U. R. M.; Claesson, P. M.; Pedersen, J. S.; Nielsen, M. M. *Journal of Physical Chemistry B* **2002**, *106*, 11412-11419.

(24) Hamley, I. W.; Pedersen, J. S.; Booth, C.; Nace, V. M. *Langmuir* **2001**, *17*, 6386-6388.

(25) Boissiere, C.; Larbot, A.; Bourgaux, C.; Prouzet, E.; Bunton, C. A. *Chemistry of Materials* **2001**, *13*, 3580-3586.

(26) Smarsly, B.; Gibaud, A.; Ruland, W.; Sturmayr, D.; Brinker, C. J. *Langmuir* **2005**, *21*, 3858-3866.

(27) Flodstrom, K.; Teixeira, C. V.; Amenitsch, H.; Alfredsson, V.; Linden, M. *Langmuir* **2004**, *20*, 4885-4891.
(28) Kipkemboi, P.; Fogden, A.; Alfredsson, V.; Flodstrom, K. *Langmuir* **2001**, *17*, 5398-5402.
(29) Flodstrom, K.; Alfredsson, V. *Microporous and Mesoporous Materials* **2003**, *59*, 167-176.
(30) Edler, K. J.; Goldar, A.; Hughes, A. V.; Roser, S. J.; Mann, S. *Microporous and Mesoporous Materials* **2001**, *44*, 661-670.
(31) Edler, K. J.; Roser, S. J.; Mann, S. *Chemical Communications* **2000**, 773-774.
(32) Klotz, M.; Albouy, P. A.; Ayral, A.; Menager, C.; Grosso, D.; Van der Lee, A.; Cabuil, V.; Babonneau, F.; Guizard, C. *Chemistry of Materials* **2000**, *12*, 1721-1728.
(33) Chao, K.-j.; Liu, P.-h.; Huang, K.-y. *Comptes Rendus Chimie* **2005**, *8*, 727-739.
(34) Holt, S. A.; Foran, G. J.; White, J. W. *Langmuir* **1999**, *15*, 2540-2542.
(35) Brennan, T.; Roser, S. J.; Mann, S.; Edler, K. J. *Langmuir* **2003**, *19*, 2639-2642.
(36) Heenan, R. K.; King, S. M. *ISIS User Guide* **1992**.
(37) Heenan, R. K.; Penfold, J.; King, S. M. *Journal of Applied Crystallography* **1997**, *30*, 1140-1147.
(38) Brennan, T.; Hughes, A. V.; Roser, S. J.; Mann, S.; Edler, K. J. *Langmuir* **2002**, *18*, 9838-9844.
(39) Warren, B. E. *X-ray Diffraction*, Dover Publication: New York 1990.
(40) Hayter, J. B.; Penfold, J. *Molecular Physics* **1981**, *42*, 109-118.
(41) Hansen, J. P.; Hayter, J. B. *Molecular Physics* **1982**, *46*, 651-656.
(42) Brinker, C. J. *Journal of Non-Crystalline Solids* **1988**, *100*, 31-50.
(43) Edler, K. J.; Brennan, T.; Roser, S. J.; Mann, S.; Richardson, R. M. *Microporous and Mesoporous Materials* **2003**, *62*, 165-175.
(44) Wang, Y. L.; Kimura, K.; Dubin, P. L.; Jaeger, W. *Macromolecules* **2000**, *33*, 3324-3331.
(45) Huo, Q. S.; Margolese, D. I.; Ciesla, U.; Demuth, D. G.; Feng, P. Y.; Gier, T. E.; Sieger, P.; Firouzi, A.; Chmelka, B. F.; Schuth, F.; Stucky, G. D. *Chemistry of Materials* **1994**, *6*, 1176-1191.
(46) Brennan, T.; Roser, S. J.; Mann, S.; Edler, K. J. *Chemistry of Materials* **2002**, *14*, 4292-4299.
(47) Maccarini, M.; Briganti, G. *J. Phys. Chem. A* **2000**, *104*, 11451 - 11458.
(48) Herrier, G.; Blin, J. L.; Su, B. L. *Langmuir* **2001**, *17*, 4422-4430.
(49) Anderson, M. W.; Egger, C. C.; Tiddy, G. J. T.; Casci, J. L.; Brakke, K. A. *Angewandte Chemie-International Edition* **2005**, *44*, 3243-3248.
(50) Egger, C. C.; Anderson, M. W.; Tiddy, G. J. T.; Casci, J. L. *Physical Chemistry Chemical Physics* **2005**, *7*, 1845-1855.

Chapter 6 Non ionic-Cationic Mixed Surfactant Templated Mesoporous Silica Films

6.1 Introduction

A number of studies on solutions of cationic/ non-ionic mixed surfactants; in particular on cetyl trimethylammonium bromide (CTAB) with mono-disperse alkyl polyethylene glycol (C_xEO_y),[1-6] or CTAB with poly-disperse Brij-type surfactants (similar to C_xEO_y surfactants)[7, 8] have been reported. Although the mixed surfactant system studied in this chapter is CTAB/$C_{16}EO_8$ no studies in the literature have been found. However we recently studied surfactant-templated polymer films prepared from polyethylene imine (PEI) with the addition of the CTAB/$C_{16}EO_8$ mixture growing at the air-liquid interface.[9] This system was analysed using neutron reflectivity, which gives structural information at the interface, SANS to measure the size of the micelles in the solution, BAM, and surface tension measurements. In this study the effect of the non-ionic surfactant concentration in the system was examined finding strong interaction between both surfactants and no interaction between $C_{16}EO_8$ and PEI. The mixed micelles were non-ideal at low surfactant concentrations but at the concentrations used for silica film preparations the micelles were ideally mixed. Thus the composition of the micelles can be assumed to be the same as that of the whole solution.

One of the earliest studies based on cationic/ non-ionic mixed surfactants was published in 1992 by Cummins *et al*, who studied the micellar structure under the influence of shear using SANS.[1] Pendfold *et al* have reported several studies on the cationic/ non-ionic mixture (CTAB/ $C_{12}EO_6$) at the solid-liquid interface using neutron reflectivity. They discussed the structure and composition of the bilayers formed at the interface and the affinity of the two surfactants for the surface by changing the pH of the solution.[2, 4] They described the system as a three-layer model with three different thicknesses. First layer is described to be adjacent to the solid surface containing head groups, the second layer containing hydrocarbon chains overlapping from both bilayer sides and a third layer which is adjacent to the fluid phase containing head groups. They also reported the same cationic/ non-ionic mixture system but absorbed at the air-water interface and discussed the interactions between both surfactants.[3] Recent studies on the effect of EO chain length when added to the cationic surfactant aqueous system have

been published revealing that shortening the EO chain induces the formation of the worm-like solutions, the concentration of which decreases with the EO chain length.[6] The effect of non-ionic head group on the formation of worm-like micelles is not completely clarified.

Most of the studies, which analyse the interaction between the surfactant molecules within the mixed micelles, were explained by a simple approach given by Rubingh.[10] By assuming a regular solution approximation, Rubingh calculated an interaction parameter, β, for particular surfactant mixtures. Some of the mixed surfactant systems, in particular cationic/ non-ionic surfactant mixtures, in which the interaction behaviour was studied using this approximation: CTAB/$C_{12}EO_4$ [5]; CTAB/$C_{12}EO_8$ [11]; CTAB/Brij35 (poly-disperse $C_{10}EO_{23}$)[8]; and CTAB/Brij93 (poly-disperse $C_{18}EO_{10}$)[7], had negative β values indicating a significant interaction between the non-ionic and cationic surfactants. Similarly O'Driscoll *et al.*[12] also found a negative β parameter value for mixed CTAB/ $C_{16}EO_8$ micelles, system studied in this chapter.

6.2 Experimental procedure

6.2.1 Sample preparation

The mixed surfactant templated silica thin films synthesis consist of a mixture of two kinds of surfactants, octa-ethylene glycol mono n-hexadecyl ether ($C_{16}EO_8$) (BC-8SY, Nikko Chemicals, Japan) as the non-ionic surfactant and cetyltrimethylammonium bromide (CTAB, Sigma 99 %) as the cationic surfactant with the final addition of tetramethoxysilane (TMOS, Acros 98 %) as the silica precursor in acidic media (0.2 M HCl).

The solution was prepared varying both surfactants (X) and silica precursor (Y) concentrations following these molar ratios:

$\frac{X}{Y}\frac{C_{16}EO_8}{CTAB}$ (see Table 6.1): 3.6×10^{-3} HCl: 1 water: Z TMOS (see Table 6.2).

Solutions were poured into a Teflon trough to form a raised meniscus and grown at the air-liquid interface.

Table 6.1. $C_{16}EO_8$/ CTAB molar ratios and the percentage of $C_{16}EO_8$ in the micelle.

% $C_{16}EO_8$	X /Y
23	0.34: 1.15 ($\times 10^{-3}$)
28	0.43: 1.07($\times 10^{-3}$)
33	0.5: 1.0 ($\times 10^{-3}$)

Table 6.2. TMOS molar ratios.

TMOS/Surfactant	Z
3.6	5.37×10^{-3}
7.3	1.07×10^{-2}
11.0	1.64×10^{-2}

Fast time-resolved *in situ* off specular X-ray reflectivity and GIXD measurements were carried out using the intensity available at the ESRF.

6.2.2 Scattering techniques

Off specular X-ray reflectivity was used to follow the nucleation and growth processes in films templated with mixed micelles of non-ionic and cationic surfactants. In chapter 4 and 5 non-ionic and cationic systems are explained separately and have suggested an important role of the silica: surfactant ratio and charge on the micelle in formation of the films templated with cationic and non-ionic surfactants.

To investigate in more detail the structure of these silica-surfactant films grown with mixed micelles GIXD technique was used. The incident angle was 0.82 ° for total reflection and the linear detector recorded the scattering in Q_{xy} space scanning up to 5°.[13] Measurements were carried out using two different angles as done in chapter 5. Both, off specular X-ray reflectivity and GIXD were carried out using an energy of 8.07 keV (λ= 1.537 Å).

The *in situ* evolution of the micelles in the bulk solution was also studied and followed by SANS studying three different $C_{12}EO_8$/ CTAB concentrations over the following molar ratios:

$\frac{X}{Y}\frac{C_{16}EO_8}{CTAB}$ (see Table 6.1): 3.6×10^{-3} HCl: 1 solvent: 1.1×10^{-2} TMOS.

As solvent three D_2O/ H_2O contrast variations were used: 100% D_2O, 60% D_2O 40% H_2O, and 40% D_2O 60% H_2O. The solutions were run at 28°C. The cells were left open to allow evaporation to occur to mimic the same conditions as when the thin film grows at the air-liquid interface. For 0.23 $C_{12}EO_8$/ 0.76CTAB and 0.33 $C_{12}EO_8$/0.66

60% D_2O contrasts and 20 min patterns were measured for 40% D_2O for contrast until precipitate was formed. For 0.28 $C_{12}EO_8$/ 0.72CTAB molar ratios sample the three D_2O/ H_2O contrasts were collected every 20 min.

6.3 Results

6.3.1 BAM studies

The film formation of these mixed surfactant templated mesoporous silica films was followed in real time by Brewster angle microscopy. Different formation stages were recorded allowing observing the *in situ* evolution. The measurements were carried out for three $C_{16}EO_8$/ CTAB molar ratios keeping TMOS and HCl concentrations constant.

Figure 6.1 shows the BAM images. The first pictures, collected around 90 minutes after TMOS addition, are during the induction period, characterised by weakly contrasting domains. This is the longest period taking approximately, in this case, four hours. During the advanced induction period non-uniformly bright regions can be observed, as samples B & C show, indicating particle nucleation and hence a surface which is close to film formation. Therefore it is difficult to predict accurately when the thin film grows. Once the film grows at the interface the image texture changes as a consequence of an increase in roughness and thickness. Further development of the film (see last column in Figure 6.1) shows parallel interference fringes as occurs for non-ionic surfactant-silica films (Chapter 5). However previous studies in silica thin films using CTAB only as cationic surfactant show a coarsened texture of the surface becoming a dense coverage. In this case the film is not as smooth and uniform in thickness as the mixed surfactant templated film and therefore interference fringes are not observed (see Figure 6.2).[13]

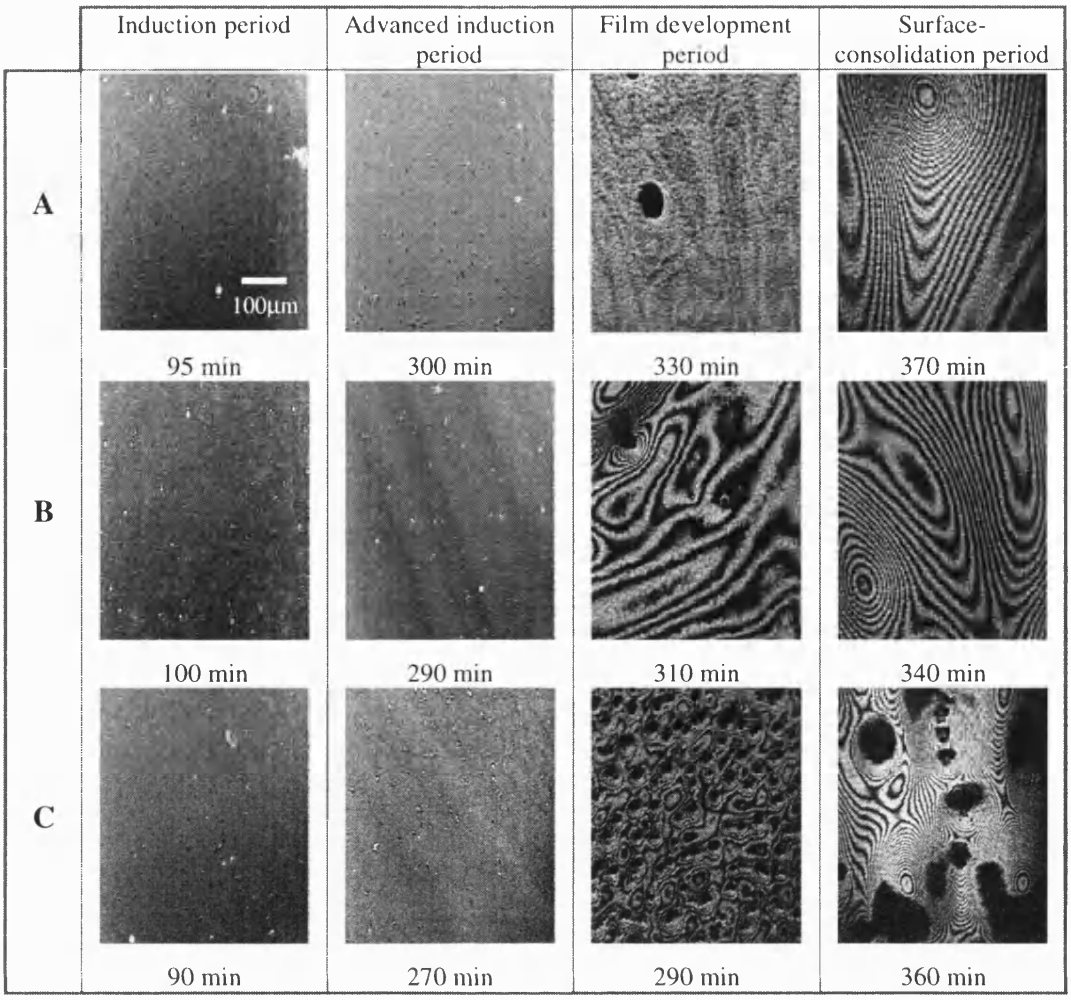

Figure 6.1. BAM images for the samples: (A) 0.23 $C_{16}EO_8$/ 0.76 CTAB, (B) 0.28 $C_{16}EO_8$/ 0.72 CTAB and (C) 0.33 $C_{16}EO_8$/ 0.66 CTAB collected at various formation times after mixing of the reagents.

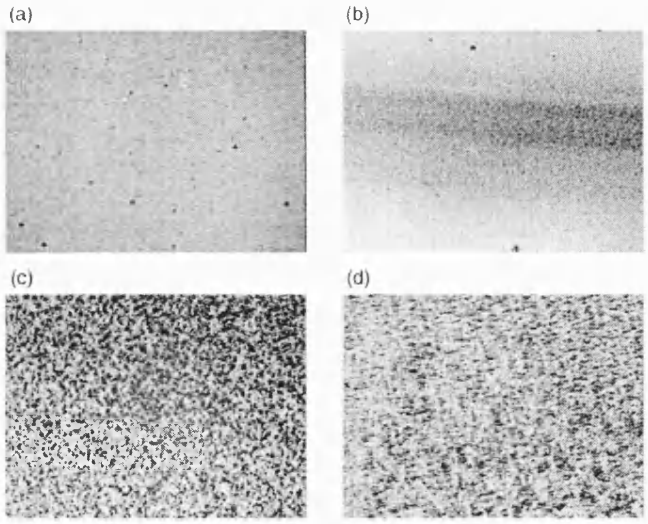

Figure 6.2. BAM images following the evolution of CTAB-TMOS mesoporous thin film at the air water interface during: (a) induction period, (b) 331 min after mixing the reagents (c) 350 min and (d) 407 min after mixing corresponding with the film development period, showing coarsening of the film at the interface. The horizontal edge of each image corresponds to 430 microns.[14]

A faster film formation of about 30 minutes was observed for each sample comparing with the formation times obtained from the off-specular reflectivity measurements. This is mainly caused by an environmental increase in temperature and decrease in humidity during BAM measurements as mentioned in chapter 4.

6.3.2 Off specular X-ray reflectivity studies

Off specular X-ray reflectivity measurements show that the rate of growth of the thin films is highly dependant on surfactant and silica precursor concentration. The effect of silica concentration on the film formation time was studied using 23, 28 and 33% of $C_{16}EO_8$ in $C_{16}EO_8$/ CTAB mixture (see Figure 6.3). For 23% $C_{16}EO_8$ the film formation slows down with increasing TMOS concentration, while for 28% $C_{16}EO_8$ the film grows faster. In the case of 33% $C_{16}EO_8$ at 3.6 TMOS/ Surfactant ratio the formation is very slow taking 430 minutes. Unlike 23 and 28% $C_{16}EO_8$ the fastest system is not the highest TMOS/ Surfactant ratio but the 7.3 one. This behaviour is similar to the TMOS/ CTAB system, which follows a "horse-shoe" shape of the time dependence profile. The TMOS/ CTAB system shows a faster film formation until the inflection point from which the system becomes slower, possibly due to a change in the

formation mechanism.[14, 15] On the other hand 28% $C_{16}EO_8$ sample has linear time dependence similar to the TMOS/ $C_{16}EO_8$ system, becoming faster with increasing TMOS concentration (see Figure 6.3).

The difference in formation time for the two first $C_{16}EO_8$/ CTAB molar ratios profiles suggests a possible dependence on the interaction between the two surfactants and their concentrations.

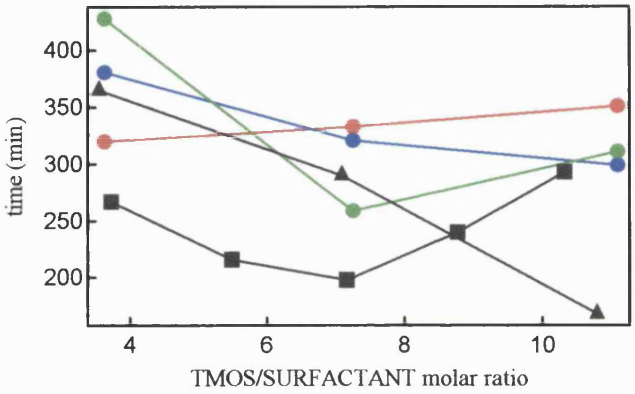

Figure 6.3. Time results for first diffraction peaks during off specular measurements comparing the three $C_{16}EO_8$/ CTAB molar ratios with the CTAB and $C_{16}EO_8$ by their own varying TMOS concentration. Each plot corresponds with: ● 0.23 $C_{16}EO_8$/0.76 CTAB, ● 0.28 $C_{16}EO_8$/0.72 CTAB, ● 0.33 $C_{16}EO_8$/0.66 CTAB, ▲ $C_{16}EO_8$, and ■ CTAB.

The study of the full width half-maximum (FWHM) of the diffraction peak in off specular reflectivity measurements allows us to suggest the formation mechanism for every thin film growth. Figure 6.4 displays this variation for the three different mixed surfactant molar ratios while varying silica precursor concentration.

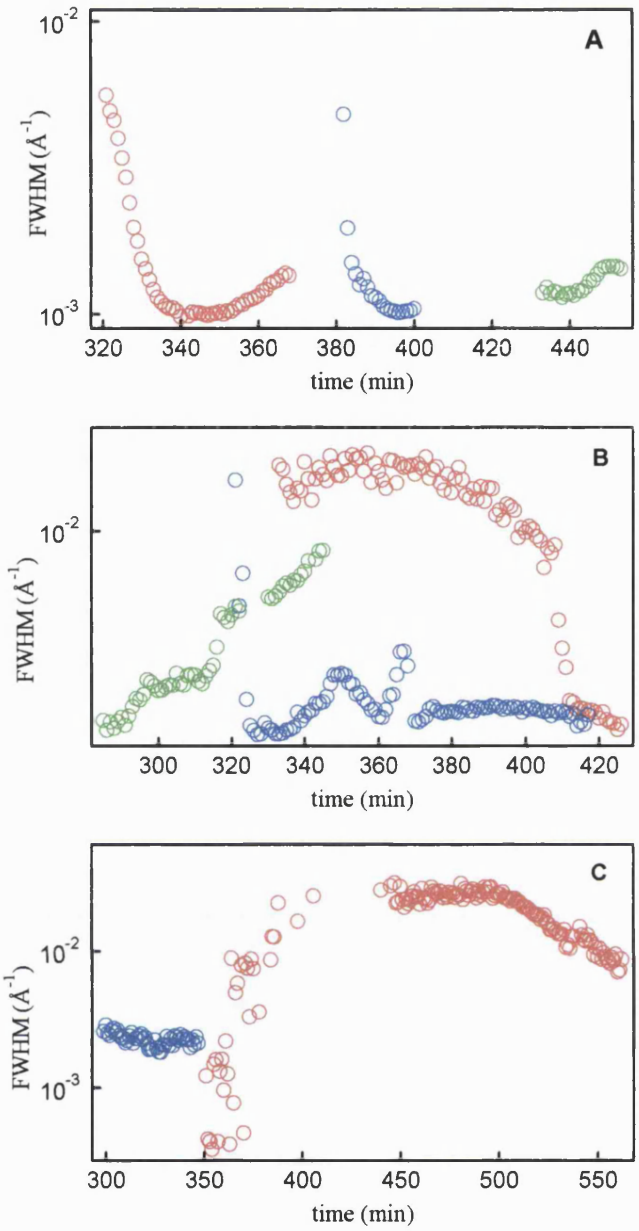

Figure 6.4. Peak width (FWHM) variation of the first diffraction peak from the off specular reflectivity patterns against time at: A) 3.6, B) 7.3, C) 11.0 TMOS/ Surfactant ratios. ○ 0.23 $C_{16}EO_8$/0.76 CTAB; ○ 0.28 $C_{16}EO_8$/0.72 CTAB; ○ 0.33 $C_{16}EO_8$/0.66 molar ratios.

Bearing in mind the Scherrer formula (equation 3-17, Chapter 3), when the first order diffraction peak first appears as a narrow peak with a certain FWHM, broadening with time, large domains are present at the solution surface from the earliest point of film formation. The film formation must therefore occur through aggregation of micelles initially in solution followed by diffusion of the aggregates to the surface. The off specular reflectivity, which measures structural development at the surface, thus

suggests that the film formation has followed a bulk-driven mechanism. On the other hand when the diffraction peak is initially broad, domain sizes at the surface are initially small suggesting that the individual micelles aggregate at the air-liquid interface. Then the peak-width becomes narrower with time and the final film develops downward into the solution. On this occasion the thin film growth follows a surface-driven mechanism. Consequently applying this theory to the FWHM results (Figure 6.4) different mechanisms are suggested and shown in Table 6.3.

Table 6.3. Non ionic-cationic mixed surfactant templated silica thin film mechanisms looking at six mixed surfactant-TMOS combinations.

TMOS/ Surfactant ratios	**3.6**	**7.3**	**11.0**
0.23 $C_{16}EO_8$/0.76 CTAB	Surface	Surface	Bulk
0.28 $C_{16}EO_8$/0.72 CTAB	Surface	Surface	Bulk
0.33 $C_{16}EO_8$/0.66 CTAB	Bulk	Bulk	—

The FWHM profile of 0.33 $C_{16}EO_8$/0.66 CTAB with 1.5 times TMOS normal concentration was not interpreted since the height of sample was too low to see the first order diffraction peak development as a consequence of solution evaporation during the induction period while off specular X-ray reflectivity measurements were collected.

6.3.3 GIXD studies

Grazing incident X-ray diffraction measurements were carried out setting the incident angle in 0.82° for 0.23 $C_{16}EO_8$/0.76 CTAB, 0.28 $C_{16}EO_8$/0.72 CTAB, and 0.33 $C_{16}EO_8$/0.66 CTAB for the same 1 time normal TMOS concentration. This incident angle was chosen since this is the position in degrees of the 1st diffraction peak measured in the off specular reflectivity.

The GIXD patterns for 0.23 $C_{16}EO_8$/0.76 CTAB (Figure 6.5) and 0.28 $C_{16}EO_8$/0.72 CTAB (Figure 6.6) have been indexed to a centred rectangular (*c2m*) structure with lattice parameters of a = 108 Å and b = 88 Å for the first sample, and a = 112 Å and b = 88.8 Å for the second sample. In the 0.33 $C_{16}EO_8$/0.66 CTAB molar ratio sample the diffraction spots, shown in Figure 6.7, indicate a body-centred cubic phase ($Im\bar{3}m$) with a cubic cell spacing of a = 80.2 Å.

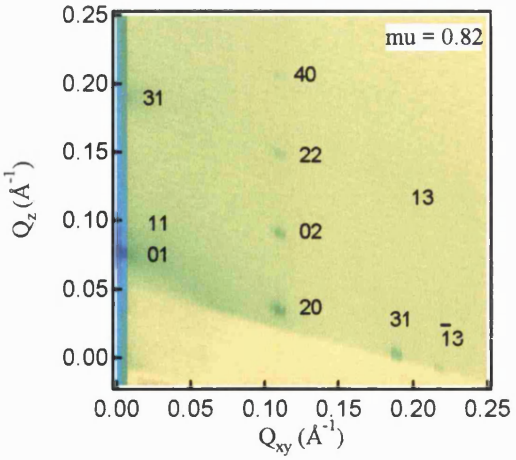

Figure 6.5. GIXD plot for a 0.23 $C_{16}EO_8$/0.76 CTAB after 9h 20 min. Incident angle 0.82°.

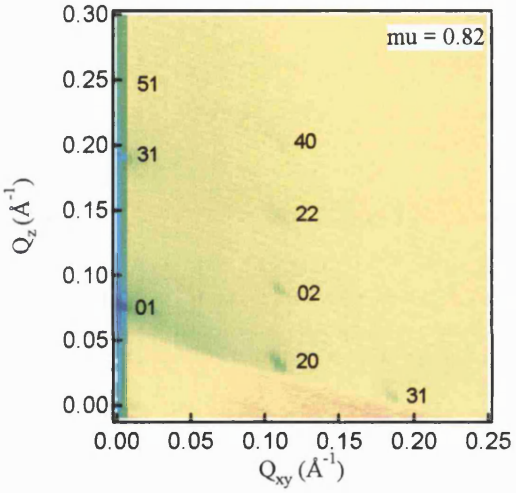

Figure 6.6. GIXD plot for a 0.28 $C_{16}EO_8$/0.72 CTAB after 8h 25 min. Incident angle 0.82°.

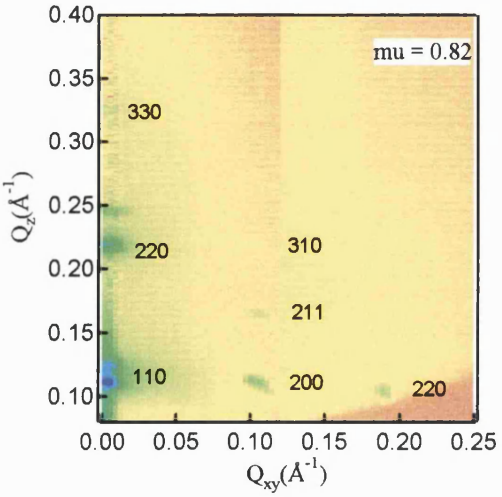

Figure 6.7. GIXD plot for a 0.33 $C_{16}EO_8$/0.66 CTAB after 7 h. Incident angle 0.82°.

6.3.4 SANS studies

SANS provides information about the evolution of the micelles in the bulk solution with time. Patterns are obtained using the D_2O/ H_2O contrast method, which due to their difference in the scattering length density allows collection of scattering from different parts of the silica-surfactant assembly.

Unlike the 7.1 TMOS/ $C_{16}EO_8$ molar ratio system, described in chapter 5, the bulk evolution patterns for the three $C_{16}EO_8$/CTAB molar ratios are characterized by the lack of a diffraction peak. In this case a weak bump is observed for the three $C_{16}EO_8$/CTAB molar ratios SANS profiles, suggesting a poorly ordered mesostructure in the bulk (see Figure 6.8).

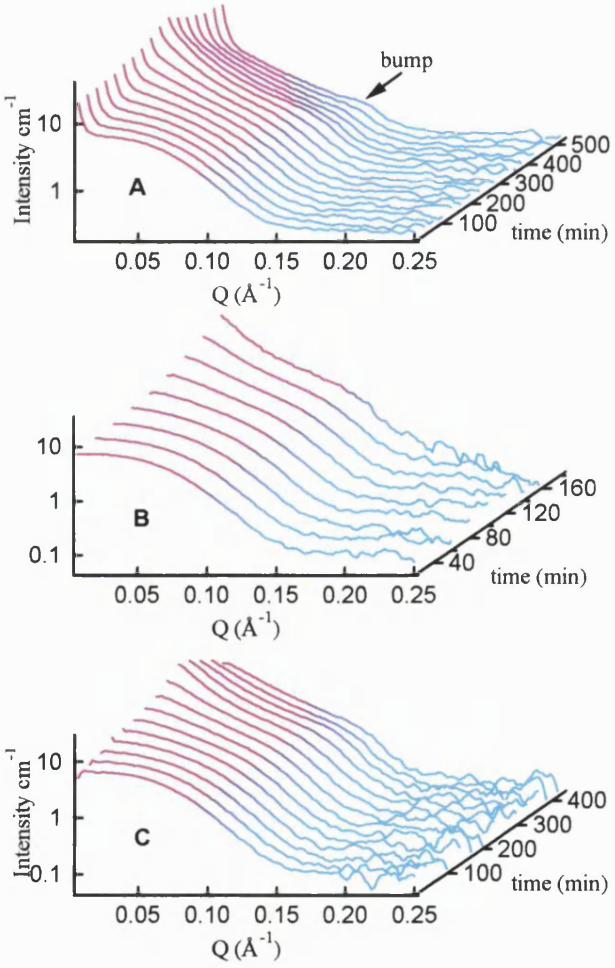

Figure 6.8. SANS profile for A) 0.23 $C_{16}EO_8$/0.76 CTAB; B) 0.28 $C_{16}EO_8$/0.72 CTAB; C) 0.33 $C_{16}EO_8$/0.66 CTAB molar ratio showing the evolution of structure in the bulk solution with time for 100% D_2O contrast.

The profiles obtained from these measurements were fitted at three D_2O/ H_2O contrasts at different times. These times were assigned according with 100% formation, which corresponds with the appearance of precipitate in the solution (see Figure 6.9). At early formation stages, 25 and 40%, the SANS patterns were fitted using a monodisperse prolate ellipsoid particle model with a core/shell structure. A transition in the shape of the micelles occurs and hence 60, 80 and 100% formation patterns were fitted with a cylindrical particle model. Both models use a core/shell form factor ($P(Q)$) in combination with a interparticle structure factor ($S(Q)$). Previous SANS studies based on charged surfactant templated silica films suggest the Hayter Penfold mean spherical approximation (MSA)[17, 18] as the structure factor, which consider Coulomb repulsion between charged particles.[19] Consequently the Hayter Penfold MSA was used in this mixed surfactant system since a cationic surfactant (CTAB) is involved in the formation of the silica film. This structure factor defines the next parameters in the SANS fitting:

- Charge. Depending on the charged surfactant concentration the charge value varies as follows:
  - 20 using only CTAB
  - 15.2 for 0.23 $C_{16}EO_8$/0.76 CTAB molar ratio
  - 14.4 for 0.28 $C_{16}EO_8$/0.72 CTAB molar ratio
  - 13.2 for 0.33 $C_{16}EO_8$/0.66 CTAB molar ratio
- Temperature (K): 298
- Monovalent salt or counterion concentration (M), which estimates the ionic strength of the solution: 0.2 (i.e. concentration of HCl used in synthesis)
- Dielectric constant of solvent: 71.1

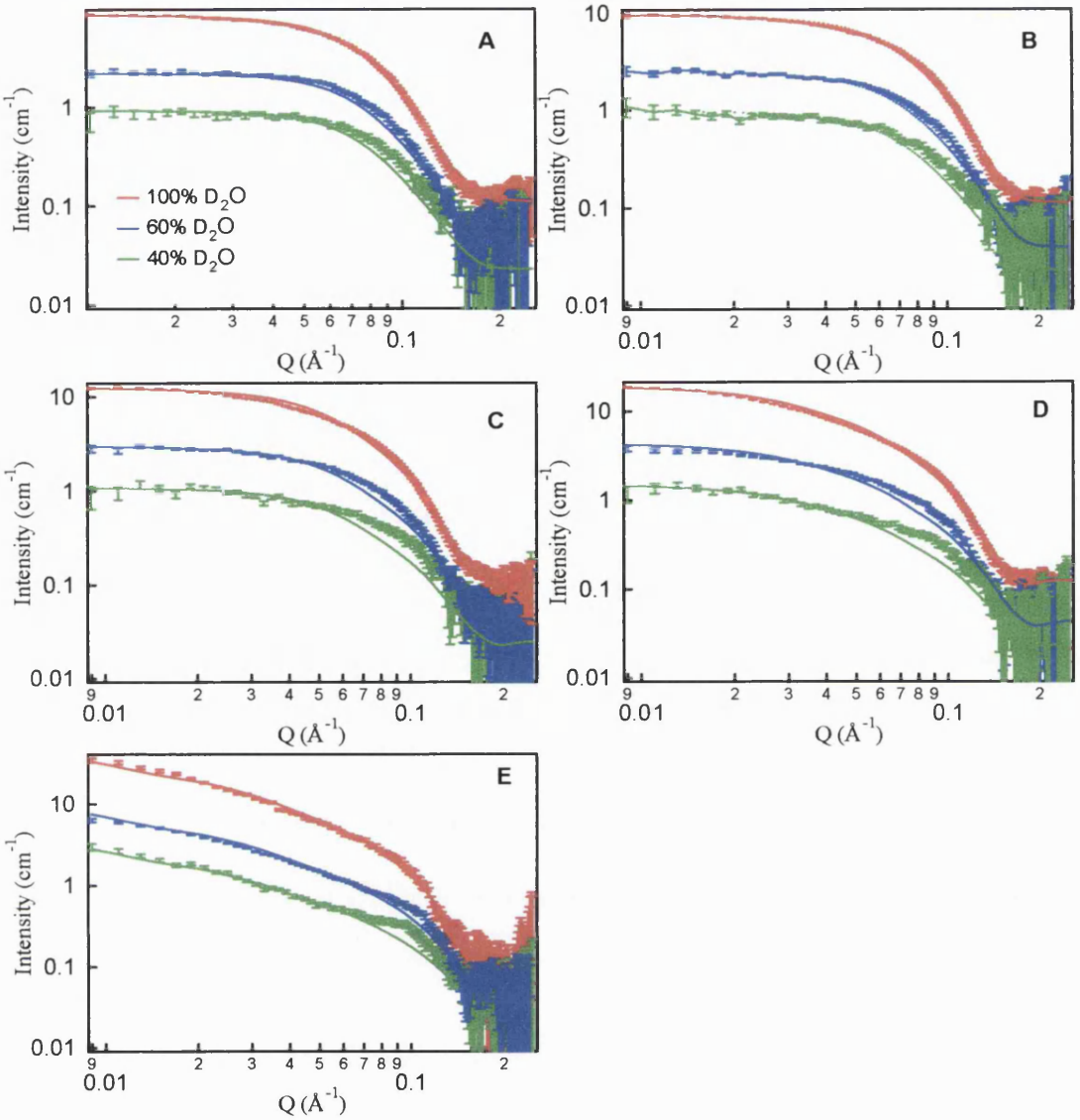

Figure 6.9. SANS fitting profile for three D_2O/ H_2O contrasts for the 0.28 $C_{16}EO_8$/0.72 CTAB molar ratio being A) 25%, B) 40%, C) 60%, D) 80%, and E) 100% of formation time.

In this mixed surfactant system it is considered that the cationic surfactant not only interacts with silica but also with non-ionic surfactant. Apart from the mentioned electrostatic interparticle effects, non-ionic surfactant-silica interactions take place, mainly by hydrogen bonding.

The form factor obtained by combining the core/shell with the prolate ellipsoid or cylinder shapes, assumes the micelle is monodisperse. The ellipsoidal micelle, shown in Figure 6.10 and 5.10, has an ellipsoid core defined by a major and minor radius, which rotates about the minor axis, surrounded by a shell. The model presented in this study

suggest a core formed by the hydrophobic hexadecyl chains from the $C_{16}EO_8$ and CTAB while the shell is thought to be formed by an assembly of hydrophilic ethylene glycol chains from $C_{16}EO_8$ and trimethylammonium groups from CTAB with silica and a small quantity of solution. Micelles are surrounded by a solution consisting mainly of water and/or D_2O with HCl and methanol that has been generated by the silica hydrolysis.

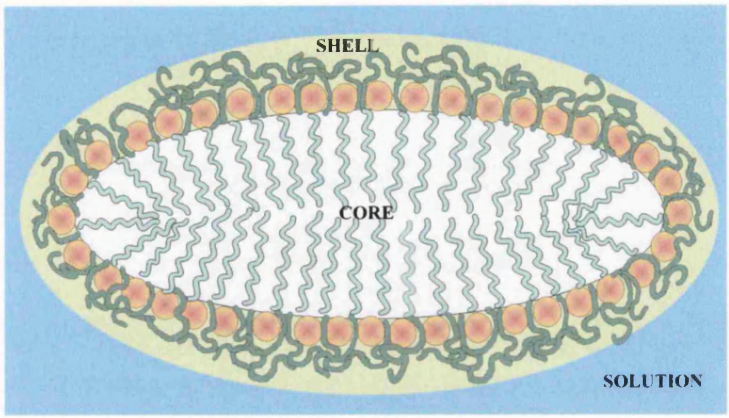

Figure 6.10. Drawing of a micelle formed in the bulk solution by the $C_{16}EO_8$/ CTAB mixed surfactant silica system.

The same fitting procedure as in the $C_{16}EO_8$/TMOS system (chapter 5) was carried out, fixing the ρ_{core} at -3.51×10^{-7} Å^{-2} and permitting some degrees of freedom for the ρ_{shell} and $\rho_{solution}$. Scattering length density values were obtained for every molar ratio sample at the three D_2O/ H_2O contrasts using the same calculations described in detail previously (see Table 6.4). Increasing in D_2O percentage causes faster formation of precipitate in the bulk. However increasing the amount of H_2O in the solution, specifically at 40% D_2O, produces larger error bars in the data due to an increase in the incoherent scattering. Brennan *et al.* suggested that the solutions with different D_2O/ H_2O ratios have different contrasts that highlight different parts of the developing micelles. [18] The appearance of a "shoulder" at high Q values in patterns taken at 40% D_2O/ H_2O, in Figure 6.9c, d and e, is therefore likely to be due to the developing silica shell around the micelles, which is not fit very well by the models used. Models consisting of "hairy micelles" have been developed to describe the scattering from micelles formed from similar non-ionic surfactants. Such models however contain many more variables than the models currently used and the current data sets will not support use of more complex models.

Results of the structural parameters of micelles are shown in Table 6.4. Micelles elongate along the X-axis while remaining constant in Y-axis and the shell becomes narrower with time for the three mixed surfactant molar ratios. In the early stages of the self-assembly process, part of the solution and methanol obtained from the TMOS hydrolysis is included in the shell structure.

Table 6.4. Values of structural parameters obtained from Prolate-CS and Cylinder-CS models at five different time formations.

		Time	t(Å)	r_1 (Å)	r_2 (Å)	L(Å)
0.23 $C_{16}EO_8$/ 0.76 CTAB	Prolate-CS	25%	9.6	19.4	46	—
		40%	9.4	19.4	52	—
	Cylinder-CS	60%	6.1	19.4	—	91
		80%	6.0	19.4	—	188
		100%	5.9	19.4	—	524
0.28 $C_{16}EO_8$/ 0.72 CTAB	Prolate-CS	25%	9.9	19.4	45	—
		40%	9.6	19.4	52	—
	Cylinder-CS	60%	7.0	19.4	—	102
		80%	6.7	19.4	—	168
		100%	6.7	19.4	—	526
0.33 $C_{16}EO_8$/ 0.66 CTAB	Prolate-CS	25%	10.3	19.4	37	—
		40%	10.1	19.4	53	—
	Cylinder-CS	60%	8.5	19.4	—	114
		80%	8.2	19.4	—	165
		100%	8.2	19.4	—	384

Time is the time of formation considering 100% to be when the solution precipitates; **t** is the shell thickness; $\mathbf{r_1}$ is the minor prolate core and cylinder core radius and $\mathbf{r_2}$ is the major core radius; **L** is the cylinder core length. The error in the fit parameters was ± 0.1 Å except for L, which is ± 2 Å.

As a result of the D_2O and/or H_2O, HCl, and MeOH concentration in the shell a slight increase in the ρ_{shell} is observed during the reaction as silica accumulates in the shell region. The $\rho_{solution}$ also decreases slightly, which could also be due to silica migration to the shell and the precipitation of silica in disordered material found in the bottom of the cell (see Table 6.5).

Furthermore with decreasing the CTAB and increasing the $C_{16}EO_8$ concentration the shell thickness increases. This could be mainly caused by the increase in the ethylene glycol chains, which have a larger volume than trimethylammonium groups producing a thicker shell.

Table 6.5. Values of scattering length densities (ρ) obtained from Prolate-HS and Core-shell Cylinder-HS models at four different formation times.

			ρ_{shell} ($\times10^{10}$cm^{-2}) in "X" %D_2O			$\rho_{solution}$($\times10^{10}$cm^{-2}) in "X" %D_2O		
		Time	**100**	**60**	**40**	**100**	**60**	**40**
0.23 $C_{16}EO_8$/ 0.76 CTAB	Prolate-CS	25%	4.05	2.74	1.80	6.07	3.41	2.08
		40%	4.03	2.73	1.82	6.07	3.41	2.08
	Cylinder-CS	60%	4.10	2.75	1.82	6.06	3.28	1.98
		80%	4.10	3.25	2.47	6.06	3.28	1.98
		100%	4.50	3.30	2.49	5.97	3.24	1.94
0.28 $C_{16}EO_8$/ 0.72 CTAB	Prolate-CS	25%	4.05	2.67	1.64	6.07	3.41	2.10
		40%	4.06	2.69	1.67	6.06	3.41	2.08
	Cylinder-CS	60%	4.06	2.87	1.89	6.06	3.34	2.03
		80%	4.29	3.05	2.10	6.04	3.28	2.00
		100%	4.74	3.25	2.26	5.98	3.19	1.99
0.33 $C_{16}EO_8$/ 0.66 CTAB	Prolate-CS	25%	3.95	2.57	1.60	6.07	3.41	2.08
		40%	4.15	2.73	1.75	6.07	3.39	2.01
	Cylinder-CS	60%	4.59	3.07	1.98	5.97	3.26	1.91
		80%	4.79	3.13	1.99	5.99	3.19	1.90
		100%	4.86	3.23	2.07	5.97	3.15	1.89

The standard deviation errors are close to $\pm 0.005\times10^{10}$.

In Figure 6.11 the ρ distributions versus the distance, measured from the centre of the micelle along the X-axis, are represented for the three $C_{16}EO_8$/CTAB molar ratios. The distances correspond with the minor and major core ratio and the cylinder length. Results show an equal variation in the ρ distributions for 25 and 40% formation time for each $C_{16}EO_8$/CTAB molar ratio where $\rho_{core} < \rho_{shell} < \rho_{solution}$ since there is no noticeable changes in the particles nor in their concentration in different parts of the structure at early times. This sequence agrees with the theoretical values.

From 60% up to 100% formation time the difference between ρ_{shell} and $\rho_{solution}$ becomes closer as the solution is being pushed out of the condensing silica network in the shell. For 80% and 100% formation time at 60% D_2O contrast the ρ_{shell} appear to be closer or practically the same as the $\rho_{solution}$, resulting the scattering be less sensitive to the shell. For the 40% D_2O contrast the ρ_{shell} is slightly higher than the $\rho_{solution}$, for the three $C_{16}EO_8$/CTAB molar ratios, due to the increasing density of the polymerising silica. The value is lower than ρ for the pure SiO_2 suggesting there is still water in the shell but since ρ_{shell} increases with time the amount of water in the shell is decreasing.

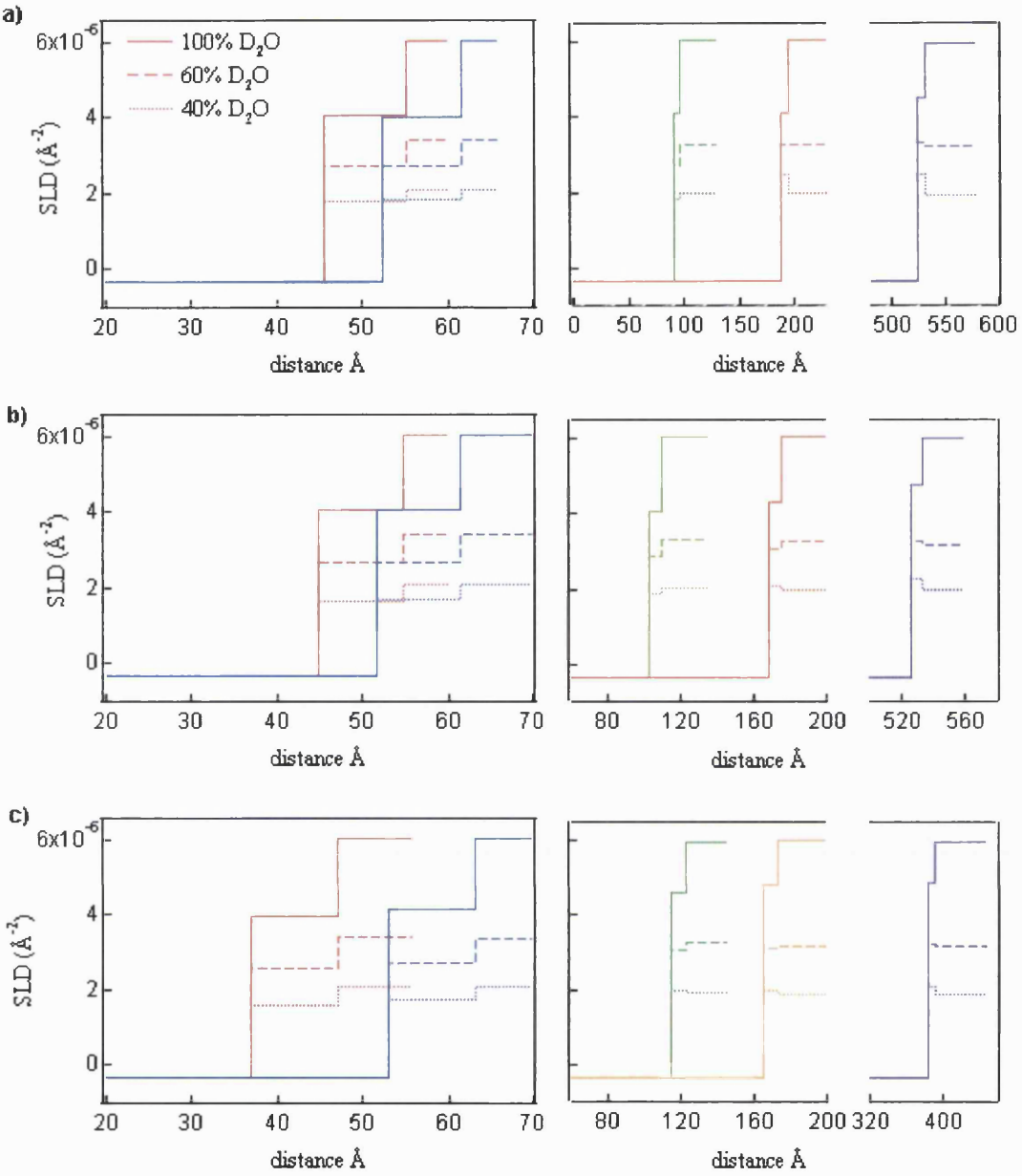

Figure 6.11. Scattering length density distributions for a) 0.23 $C_{16}EO_8$/0.76 CTAB, b) 0.28 $C_{16}EO_8$/0.72 CTAB and c) 0.33 $C_{16}EO_8$/0.66 CTAB molar ratios and for different formation times: 25% (—); 40% (—); 60% (—); 80% (—); 100% (—).

6.4 Discussion

A significant change in the time film formation rate is observed using off specular X-ray reflectivity measurements, for the three mixed surfactants molar ratios at varying silica precursor concentrations. The understanding of the different behaviours in the growth rate in this complex system is not obvious to explain. The dependence of film formation time with TMOS and mixed surfactant concentration rely on the balance between the hydrophobicity, length and charge density of the silica polymer and the availability of micelles to interact with the silica.[15] Unlike micelle-silica interactions in the cationic surfactant-silica system, which occurs via surfactant counterions, in this mixed surfactant system is thought to occur not only via cationic surfactant counterions but also via H-bonding from the hydrophilic part of the non-ionic surfactant.

The rate of film formation time in the 28% $C_{16}EO_8$ solution follows a linear decreasing dependence on silica concentration similar to that of the $C_{16}EO_8$-silica system and the 33% $C_{16}EO_8$ shows a similar profile to that with only CTAB (horse-shoe shape[15]). However for 23% $C_{16}EO_8$ solution different behaviour is shown, being slightly slower formation (around 40 min) as TMOS concentration increases. On the other hand, for a fixed TMOS concentration, film formation time also depends on the $C_{16}EO_8$/CTAB concentration ratios and their interactions. At low TMOS concentration the film forms faster for the 23% $C_{16}EO_8$ solution where CTAB is the largest component of the micelle and therefore it could be suggested that the film formation depends more on the CTAB-silica electrostatic interactions. However for intermediate and high TMOS concentration the 23% $C_{16}EO_8$ solution seems to be the slower one probably due to the insufficient charge balance between silica and CTAB counterions.

Studies on the first diffraction peak-width have shown similar formation mechanisms for both 23% and 28% $C_{16}EO_8$ solutions. But unlike the previous molar ratios 33% $C_{16}EO_8$ case seems to follow a bulk-driven mechanism for 3.6 and 7.3 TMOS/ Surfactant molar ratio. The presence of a small broad peak shown in the time-resolved SANS backs up this suggested mechanism although the particles formed in this system are much less well ordered than in the pure surfactant/ TMOS solutions.

In the case of $C_{16}EO_8$ surfactant only -silica system for 7.1 TMOS/ $C_{16}EO_8$ molar ratio, studied in chapter 5, the presence of a diffraction peak in SANS profiles suggests a development of an ordered mesophase in solution before reaching the interface.

Consequently the self-assembly templating mechanism for the 0.33 $C_{16}EO_8$/0.66 CTAB sample could follow an intermediate mesophase evolution.

BAM results show an interesting difference in surface texture, once the film is formed, comparing to the CTAB- TMOS mesoporous thin film and the $C_{16}EO_8$/CTAB mixed surfactant silica system. The presence of the interference fringes in the mixed surfactant system indicates a smoother and more uniform film than the CTAB only system.

GIXD results have suggested that a change in the structure from 2D centred rectangular to cubic occurs with the increase in $C_{16}EO_8$/ CTAB molar ratio. In the case of 33% $C_{16}EO_8$ sample, the increase of $C_{16}EO_8$ concentration produces an increase in the area occupied by the ethylene glycol groups (EO) in the shell, as SANS results demonstrate, and therefore the molecular packing parameter (*v/al*) will decrease (see section 1.2.2, chapter 1). This could suggest that the micelles self-organize looking for a minimum in energy causing a possible micellar shape transition from rodlike to spherical as extra SiO_2 is packed around them, changing, consequently, the structure from rectangular to cubic.

SANS fitting result show a shell thickness (*t*) in the micelles for the CTAB-TMOS system of between 3 and 4 Å,[19] while for the mixed surfactant this value is approximately 10 Å. The shell thickness in the mixed surfactant system increases since the $C_{16}EO_8$ head group is longer than the CTAB head group, producing a decrease in the total number of micelles density. It is interesting observing also how *t* varies comparing the mixed surfactant-silica system with the non-ionic-silica one. In every system containing non-ionic surfactant the shell thickness decreases with time. However as the $C_{16}EO_8$ molar ratio increases in the mixed surfactant case, *t* becomes thicker for a specific time (e.g. at 40 % formation time *t* changes from 9.4, 9.6 to 10.1 Å). A significant similarity in *t* is seen for the $C_{16}EO_8$ only-TMOS and the 33% $C_{16}EO_8$-TMOS samples which have values of 12 and 10 Å in the prolate-ellipsoidal micelle model and 8 Å in both cases for the cylinder model.

6.5 Conclusions

Factors such as the species concentration and their corresponding interactions are responsible in both growth time and mechanisms of formation in mixed surfactant templated silica films. Off-specular X-ray reflectivity was employed to study the formation time of the mesoporous silica films as a function of the mixed-surfactant and silica precursor concentration. At the lowest TMOS concentration the film takes more time to grow as the $C_{16}EO_8$/ CTAB molar ratios increases. However as the TMOS concentration increases the measurements show a reverse order in film formation time being the sample with the smallest $C_{16}EO_8$/ CTAB molar ratio the slowest one. This variable behaviour is due to diverse type of attractions (electrostatic, H-bonding), between the silica and the mixed surfactants, which are dependent on all of the reactant concentrations. The film growth mechanisms were also studied by off-specular method looking at the first diffraction peak-width profiles for the three $C_{16}EO_8$/ CTAB molar ratios at three TMOS concentration. For 23% and 28% $C_{16}EO_8$ samples at 3.6 and 7.3 TMOS/ Surfactant molar ratios the evolution of the peak-width implies that small domains grows down into the solution with time, following the called surface-driven mechanism. However a bulk-driven mechanism has been suggested at the 1.5 times TMOS normal concentration where well-ordered aggregates formed in the bulk solution diffuses to the surface.

In contrast, for 0.33 $C_{16}EO_8$/0.66 CTAB molar ratio at 3.6 and 7.3 TMOS/ Surfactant molar ratios has been thought to be described by a bulk-driven mechanism.

Well-ordered final thin film mesostructures were obtained by GIXD, observing a centred rectangular (*c2m*) structure for the smallest and intermediate $C_{16}EO_8$/ CTAB molar ratios and body-centred cubic phase ($Im\bar{3}m$) for the highest one. This significant change in the structure is the result of the increase in the non-ionic surfactant concentration and the self-organization and arrangement of the $C_{16}EO_8$ head groups in the shell.

The *in situ* evolution of the micelles in the bulk solution was studied by SANS for the three $C_{16}EO_8$/ CTAB molar ratios with the normal TMOS concentration at three different D_2O/H_2O contrast variations. A gradual micellar evolution from ellipsoidal, which elongates with time, to cylindrical was observed. A monodisperse prolate ellipsoid particle model with a core/shell structure has been employed to quantify the size and shape or the structure formed in solution. A general increase in the shell

thickness has been observed with the increase of the $C_{16}EO_8$/ CTAB molar ratios as a consequently increase of the voluminous head group of $C_{16}EO_8$. A spectacular increase in the length of the rod like aggregate with time is also shown. These rod-like aggregates rearrange with time and the increased silica concentration coat the micelles producing a change in the micellar shape from rod-like to spherical, which will form the final cubic phase.

6.6 References

(1) Cummins, P. G.; Penfold, J.; Staples, E. *Langmuir* **1992**, *8*, 31-35.
(2) Penfold, J.; Staples, E. J.; Tucker, I.; Thompson, L. J.; Thomas, R. K. *Physica B-Condensed Matter* **1998**, *248*, 223-228.
(3) Penfold, J.; Staples, E. J.; Tucker, I.; Thomas, R. K. *Colloids and Surfaces a-Physicochemical and Engineering Aspects* **1999**, *155*, 11-26.
(4) Penfold, J.; Staples, E. J.; Tucker, I.; Thompson, L. J.; Thomas, R. K. *International Journal of Thermophysics* **1999**, *20*, 19-34.
(5) Rodenas, E.; Valiente, M.; Villafruela, M. D. *Journal of Physical Chemistry B* **1999**, *103*, 4549-4554.
(6) Rodriguez, C.; Acharya, D. P.; Maestro, A.; Hattori, K.; Aramaki, K.; Kunieda, H. *Journal of Chemical Engineering of Japan* **2004**, *37*, 622-629.
(7) Zakharova, L.; Valeeva, F.; Zakharov, A.; Ibragimova, A.; Kudryavtseva, L.; Harlampidi, H. *Journal of Colloid and Interface Science* **2003**, *263*, 597-605.
(8) Gao, H. C.; Zhu, R. X.; Yang, X. Y.; Mao, S. Z.; Zhao, S.; Yu, J. Y.; Du, Y. R. *Journal of Colloid and Interface Science* **2004**, *273*, 626-631.
(9) O'Driscoll, B. M. D.; Fernandez-Martin, C.; Wilson, R. D.; Roser, S. J.; Edler, K. J. *Journal of Physical Chemistry B* **2006**, *110*, 5330-5336.
(10) Rubingh, D. N. *Mixed Micelle Solutions. In Solution Chemistry of Surfactants*; Mittal, K. L., Plenum: New York, 1979.
(11) Ruiz, C. C.; Aguiar, J. *Colloids and Surfaces a-Physicochemical and Engineering Aspects* **2003**, *224*, 221-230.
(12) Brennan, T.; Roser, S. J.; Mann, S.; Edler, K. J. *Langmuir* **2003**, *19*, 2639-2642.
(13) Edler, K. J.; Roser, S. J.; Mann, S. *Chemical Communications* **2000**, 773-774.
(14) Brennan, T.; Hughes, A. V.; Roser, S. J.; Mann, S.; Edler, K. J. *Langmuir* **2002**, *18*, 9838-9844.
(15) Edler, K. J.; Brennan, T.; Roser, S. J.; Mann, S.; Richardson, R. M. *Microporous and Mesoporous Materials* **2003**, *62*, 165-175.
(16) Hayter, J. B.; Penfold, J. *Molecular Physics* **1981**, *42*, 109-118.
(17) Hansen, J. P.; Hayter, J. B. *Molecular Physics* **1982**, *46*, 651-656.
(18) Brennan, T.; Roser, S. J.; Mann, S.; Edler, K. J. *Chemistry of Materials* **2002**, *14*, 4292-4299.

Chapter 7 Mesoporous Titania Thin Films

7.1 Introduction

The synthesis of mesoporous silica is nowadays widespread, however the mesoporous transition metal (TM) oxides materials have been less explored. The TMs present higher reactivity toward hydrolysis and condensation and different oxidation states and coordination than Si making it much more difficult to obtain stable mesostructured materials.[1, 2] One of the most interesting TM oxides is titanium dioxide, due to its potential applications in areas such as (photo)catalysis,[3, 4] photovoltaics,[5, 6]chemical sensors, and membranes.[7] Transition metal alkoxides (or halogenides) are mostly used as precursors. Due to the high reactivity of Ti(IV) most of the investigations rely on controlling its fast hydrolysis and condensation, which generate poorly structured materials. It is necessary, hence, to slow down the hydrolysis rate by addition of stabilizing agents. The hydrophilic head-group of surfactant molecules, such as poly(ethylene oxide)-based surfactants, [1, 8-11] acts as both as a structure directing agent and as a coordinating ligand to the titanium precursor. Moreover, acetylacetonate[12] and complexing agents such as alkanediols,[13] glycolate,[14] have also been used as bidentate ligands to coordinate the reactive titanium species. Apart from that, peroxides in basic media,[2, 15] and protons in acid media coming from sulphuric acid and titanium oxosulfates[16] also inhibit the rapid hydrolysis-condensation.

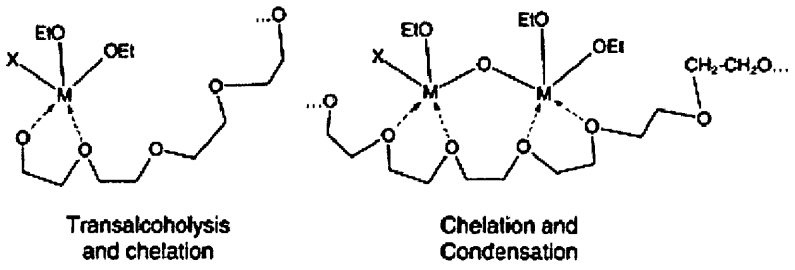

Figure 7.1. Schematic of the metal-poly(ethylene oxide)-based surfactants interactions.[9]

Most of the reported mesoporous titania methods produce bulk materials, in the form of powders[17] or xerogels[18] (also called xerogel films). On the other hand the majority of the studies based on titania thin films are mainly obtained by spin coating [19, 20] and dip coating [1, 11, 21, 22] evaporation assisted methods (see chapter 1).

In the synthesis of mesoporous silica cationic surfactants are often used as templates. However titania is more positively charged than silica in solution at pH ~ 0 since the titania isoelectric point is ca. pH 6, while that of silica is ca. pH 2. Therefore to produce mesostructured titania films in acidic media an anionic surfactant such as sodium dodecylsulphate (SDS) is considered to work more effectively, following electrostatic templating pathways.[23] The neutral templating route has been also considered using non-ionic surfactants as templates. Grosso *et al*[1] reported for the first time the synthesis, by dip-coating method, of mesoporous titania thin films with a high order in the pore mesostructure. They reported a 2D hexagonal structure using poly(ethylene oxide)-based surfactants as structure directing agents and titanium tetrachloride as precursor in acidic solution. Subsequently Alberius *et al*[22] reported the synthesis of highly organized mesoporous titania thin films very similar method to that proposed by Grosso and Soler Illia *et al.*[1, 2, 9]They used highly acidic conditions in the prehydrolysis solution (pH ≈ –1), with a HCl: Ti ratio of 6 while Grosso *et al* set this ratio between 0 and 4, preventing immediate TiO_2 precipitation.[22]

Recently and more related with this thesis, mesoporous titania thin films grown spontaneously at the air-water interface have been reported by Henderson *et al.*[24, 25] In this study the synthesis of mesoporous titania thin films was achieved via alkaline (pH ≈ 10) and acidic (pH < 1) solutions. The alkaline route was prepared using a cationic surfactant as template while an anionic surfactant, in particular SDS, was used for the acidic route. Titanium (IV) tetrabutoxide ($Ti(OBu^n)_4$) was chosen for both solutions as titania precursor and triethanolamine (TEA) as stabilizing agent to prevent immediate precipitation of titania. For TiO_2-SDS films time-resolved studies showed a possible lamellar structure.

In this chapter the method of mesoporous TiO_2 thin films at the air-water interface is studied using the method of Henderson *et al* for acidic media. However to compare with the synthesis of mesosporous silica films no stabilizing agents were used. Therefore TiO_2 thin films were prepared using anionic and non-ionic surfactant as structure directing agents and $Ti(OBu^n)_4$ as titania precursor in acidic media. The study is focused on:

a) the effect of acid concentration upon the growth speed of the anionic and non-ionic surfactant templated titania thin films.
b) the differences between electrostatic and neutral templating routes using anionic and non-ionic surfactant respectively.
c) the effect of titania: surfactant molar ratio on the growth mechanism and on the final mesostructure in the films, which is similar to the work done on silica-surfactant films.[2, 4]

7.2 Experimental procedure

7.2.1 Sample preparation

Mesoporous titania thin films were prepared using two different surfactants as templates, anionic and non-ionic surfactants. The first system consists of a solution using sodium dodecylsulphate (SDS) as the anionic surfactant, titanium (IV) tetrabutoxide ($Ti(OBu^n)_4$) as the titania precursor in acidic media using HCl. Solutions were prepared by varying HCl and SDS concentrations.

X SDS: Y HCl: 1 water: 1.7×10^{-3} $Ti(OBu^n)_4$, defining X and Y in Table 7.1

Table 7.1. SDS (X) and HCl (Y) molar ratios and their respective concentration fractions.

X Fraction	X (mol/l)	X	Y Fraction	Y (mol/l)	Y
1/2	0.7×10^{-2}	1.4×10^{-4}	1/10	0.14	2.8×10^{-3}
3/4	1.1×10^{-2}	2.1×10^{-4}	1/4	0.36	7.0×10^{-3}
1*	1.4×10^{-2}	2.8×10^{-4}	1/2	0.73	1.4×10^{-2}
5/4	1.8×10^{-2}	3.4×10^{-4}	3/4	1.09	2.1×10^{-2}
3/2	2.1×10^{-2}	4.1×10^{-4}	1*	1.46	2.8×10^{-2}

* the value of 1 correspond to "normal" concentrations.

In the second system the polyoxyethylene 10 cetyl ether (Brij56®) was used as non-ionic surfactant, $Ti(OBu^n)_4$ as the titania precursor in acidic media. Solutions were prepared:

a) varying Brij56® for two different HCl concentrations and keeping constant the titania precursor at the following molar ratios:

X Brij56®: 2.1×10^{-2} HCl: 1 water: 1.7×10^{-3} $Ti(OBu^n)_4$

X Brij56®: 2.8×10^{-2} HCl: 1 water: 1.7×10^{-3} $Ti(OBu^n)_4$ (see Table 7.2).

b) varying HCl keeping constant Brij56® and the titania precursor at the following molar ratios:

2.7×10^{-4}Brij56®: Y HCl: 1 water: 1.7×10^{-3} $Ti(OBu^n)_4$ (see Table 7.2).

c) varying $Ti(OBu^n)_4$ keeping constant the surfactant and HCl concentration at the following molar ratios:

2.7×10^{-4} Brij56®: 2.8×10^{-2} HCl: 1 water: Z $Ti(OBu^n)_4$ (see Table 7.2).

Table 7.2. Brij56® (X), HCl (Y), and $Ti(OBu^n)_4$ (Z) molar ratios and their respective concentration fractions.

X Fract.	Brij56® (mol/l)	X	Y Fract.	HCl (mol/l)	Y	Z Fract.	$Ti(OBu^n)_4$ (mol/l)	Z
1/2	0.7×10^{-2}	1.4×10^{-4}	1/2	0.73	1.4×10^{-2}	1/2	4.3×10^{-2}	8.3×10^{-4}
1	1.4×10^{-2}	2.7×10^{-4}	3/4	1.09	2.1×10^{-2}	3/4	6.5×10^{-2}	1.2×10^{-3}
3/2	2.1×10^{-2}	4.1×10^{-4}	1	1.46	2.8×10^{-2}	1	8.7×10^{-2}	1.7×10^{-3}
2	2.8×10^{-2}	5.5×10^{-4}	—	—	—	3/2	13.0×10^{-2}	2.5×10^{-3}

* the value of 1 correspond to "normal" concentrations.

Solutions were poured into a Teflon trough to form a raised meniscus. The surface area was 63 cm^2 and the solution was around 0.5 mm deep. Films were prepared by first dissolving the surfactant template in water and the $Ti(OBu^n)_4$ in concentrated HCl. These two solutions were mixed and poured into a teflon trough (see chapter 2 for more detail).

7.2.2 Scattering techniques

In the case of SDS templated titania syntheses, film growth is too fast to obtain time-resolved off-specular reflectivity data on the $Ti(OBu^n)_4$-SDS films. Hence specular reflectivity and GIXD measurements were carried out to identify the film structures. However mesoporous Brij56® templated titania thin films grow slow enough to be able to use off specular X-ray reflectivity and monitor the growth process until the films were formed at the air-liquid interface. Specular reflectivity and GIXD were also used for this second system. For all reflectivity and GIXD measurements the trough was mounted on a temperature controlled base, on the beamline. The temperature was maintained at 25°C.

The three measurements were carried out on beamline ID10B (Tröika II) at the ESRF with a beam wavelength of 1.554 Å (E = 7.99 keV). For off specular the incident angle (θ_i) was set at 1.27°. The measured range was Q = 0.06–0.3 $Å^{-1}$. Specular

reflectivity profiles were obtained once the films had grown at the air-liquid interface. The incident beam swept the angular range of 0 °–4°.[26] GIXD measurements were collected, immediately after the specular measurements, at two fixed incident angles, which allow investigating the structures as a function of penetration depth. A linear detector records the scattering in Q_{xy} space scanning up to 4°.[27]

As previous experiments, SANS measurements were carried out in the LOQ instrument. Three different SDS/ $Ti(OBu^n)_4$ concentrations were prepared over the following molar ratios:

X SDS: 1.4×10^{-2} HCl: 1 water: 1.7×10^{-3} $Ti(OBu^n)_4$, where X= 1.4×10^{-4}, 2.7×10^{-4} and 4.1×10^{-4} at different D_2O/ H_2O contrasts (see Table 7.1).

Patterns were collected at 40 μA for every sample at three D_2O/ H_2O contrasts.

7.3 SDS-templated Mesoporous Titania Thin Films

7.3.1 X-ray Reflectivity Results

X-ray specular reflectivity measurements were carried out to investigate how the acid and the surfactant concentration affect the anionic surfactant templated titania thin film structures.

To study the effect of the acid five HCl concentrations were prepared keeping SDS and $Ti(OBu^n)_4$ concentration constant with the following molar ratios:

2.8×10^{-4} SDS: Y HCl: 1 water: 1.7×10^{-3} $Ti(OBu^n)_4$.

The reflectivity patterns, shown in Figure 7.2, exhibit clear evidence on the effect of the acid concentration on the structural organization of the film. The sharp Bragg peaks indicate a well-organized multilayer and for a layered structure with a periodicity normal to the interface the vertical scattering vector corresponds to the specular Bragg peak positions, also given in *d*-spacing as next equation shows:

$$Q_z = \frac{2\pi}{d}$$

Decreasing HCl concentration results in a lack of Bragg peaks, indicating a lower degree of structural organization. For 1/2, 3/4, and 1 times HCl concentration three well-defined Bragg peak are observed that indicates a high degree of ordering. For 1/2 and 3/4 × HCl profiles show highest peak intensities, however broader peaks are observed for 3/4 × HCl indicating smaller domain organization. Therefore the optimum

concentration of HCl in this specific system for the best ordering is around 1/2 × HCl concentration. A shift in the Bragg peak positions is also observed (see Table 7.3).

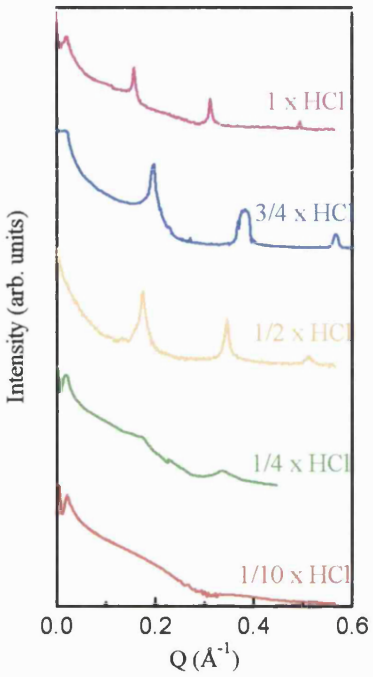

Figure 7.2. Specular reflectivity patterns for different samples varying HCl concentrations following these molar ratios: 2.8×10^{-4} SDS: Y HCl: 1 water: 1.7×10^{-3} $Ti(OBu^n)_4$. (Every reflectivity profile has been equally scaled where Y-axis has been normalized to 1, which corresponds to the critical angle)

Table 7.3. Bragg peaks given in Q ($Å^{-1}$) and *d*-spacing (Å) values for five different HCl concentrations for 2.8×10^{-4} SDS: Y HCl: 1 water: 1.7×10^{-3} $Ti(OBu^n)_4$ molar ratios.

Y	Bragg peaks					
	1st		2nd		3rd	
	$Å^{-1}$	Å	$Å^{-1}$	Å	$Å^{-1}$	Å
1/10	—	—	—	—	—	—
1/4	0.174	36.1	0.336	18.7	—	—
1/2	0.175	35.9	0.346	18.2	0.511	12.3
3/4	0.196	32.1	0.381	16.5	0.567	11.1
1	0.157	40.0	0.310	20.3	0.494	12.7

The errors for the Bragg peaks correspond with values between ± 1 and 2 Å.

A second experiment was performed focusing on the effect of surfactant concentration looking at the three acid concentrations, which gave a good structural definition in the previous experiment. The solutions were prepared following the molar ratios:

i. X SDS: 1.4×10^{-2} HCl: 1 water: 1.7×10^{-3} $Ti(OBu^n)_4$. Here 1/2 of the normal HCl concentration is used.

ii. X SDS: 2.1×10^{-2} HCl: 1 water: 1.7×10^{-3} $Ti(OBu^n)_4$. In this case 3/4 of the normal HCl concentration is used.

iii. X SDS: 2.8×10^{-2} HCl: 1 water: 1.7×10^{-3} $Ti(OBu^n)_4$. The HCl concentration used here is the one called " normal or standard concentration".

In Figure 7.3 specular reflectivity profiles show different behaviours for these three experiment sets. For 1/2 × HCl show a good structural definition however at the smallest SDS concentration it appears that only a very thin film is formed since the Bragg peaks get broader suggesting only a few repeat units at surface. For 3/4 × HCl the 3/4 and 1/2 × SDS profiles seem to have two phases present since they show double peaks.

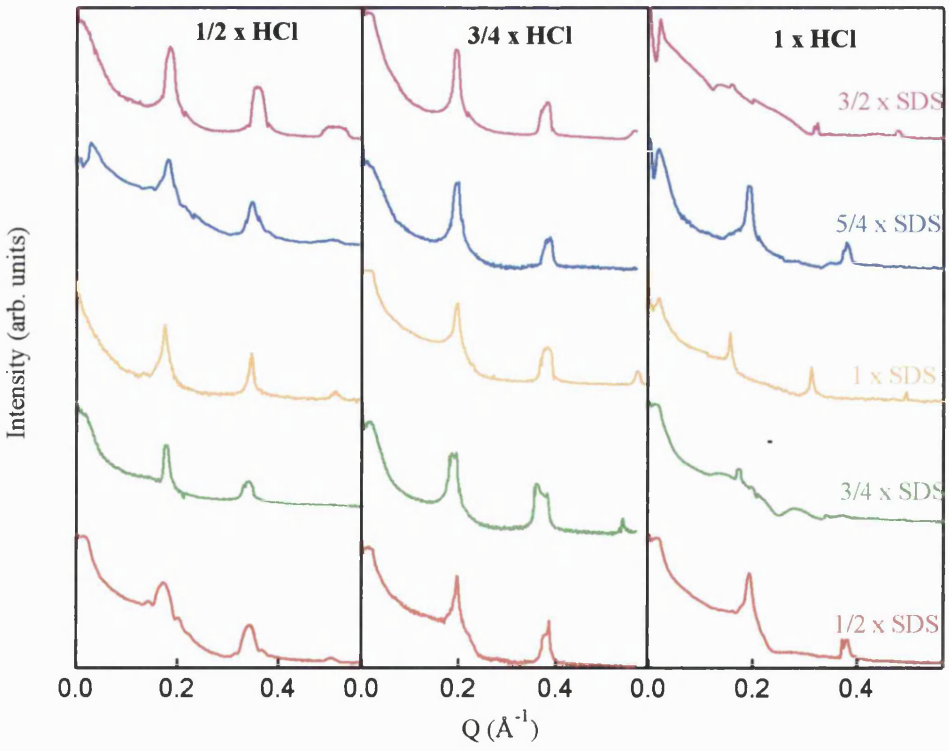

Figure 7.3. Specular reflectivity patterns for different samples varying SDS and HCl concentrations.

Table 7.4 shows a significant difference between *d*-spacing values for the three HCl concentrations. For 1/2 and 3/4 × HCl varying SDS concentration *d*-spacings are quite constant but very random for 1 × HCl. These random *d*-spacing values could be due to the fact that less ordered phases do not pack together very well so average distance between micelles varies.

Table 7.4. Bragg peaks given in Q ($Å^{-1}$) and *d*-spacing (Å) values for five different SDS concentrations at three different HCl concentrations following these molar ratios: X SDS: Y HCl: 1 water: 1.7×10^{-3} $Ti(OBu^n)_4$.

		Bragg peaks					
	X	1st		2nd		3rd	
		$Å^{-1}$	Å	$Å^{-1}$	Å	$Å^{-1}$	Å
1/2 × HCl	1/2	0.174	36.1	0.340	18.5	0.506	12.4
	3/4	0.175	35.9	0.340	18.5	—	—
	1	0.175	35.9	0.346	18.2	0.511	12.3
	5/4	0.179	35.1	0.346	18.2	0.505	12.4
	3/2	0.184	34.1	0.360	17.4	0.513	12.2
3/4 × HCl	1/2	0.196	32.1	0.374 & 0.386	16.8 & 16.3	—	—
	3/4	0.185	33.9	0.360 & 0.380	17.4 & 16.5	0.535	11.7
	1	0.196	32.1	0.381	16.5	0.567	11.1
	5/4	0.195	32.2	0.384	16.4	—	—
	3/2	0.195	32.2	0.381	16.5	~0.56	11.2
1 × HCl	1/2	0.193	32.5	0.380	16.5	—	—
	3/4	~0.175	35.9	~0.28	22.4	~0.36	17.4
	1	~0.157	40.0	0.310	20.3	0.494	12.7
	5/4	0.192	32.7	0.378	16.6	—	—
	3/2	~158	39.7	~0.32	19.6	0.477	13.2

The errors for the Bragg peaks correspond with values between ± 1 and 2 Å.

7.3.2 GIXD Results

In situ GIXD was also used as a depth profiling technique to investigate changes the mesostructures in SDS-templated mesoporous titania thin films varying the surfactant concentration. A first incident angle was set at 0.13° and a second measurement was performed at higher angle (1.22, 1.25, 1.28 and 1.3°), corresponding with the angle of the first diffraction peak, to compare the film surface-air interface with the film-bulk solution interface (see Figure 7.4). GIXD is the only technique that will allow us to probe the structure of the bulk film *in situ*.

GIXD patterns for both incident angles show powder-like diffraction rings appearing at the same Q position for every SDS-titania film. For the 1/2 and 3/4 × SDS films the second diffraction ring is difficult to see suggesting a worse mesostructural ordering than in the case of 1, 5/4, and 3/2 × SDS films. This discussion could agree with the X-ray reflectivity results, shown in the 1/2 × HCl column in Figure 7.3, in which the Bragg peaks for 1/2 and 3/4 × SDS films guest that these films are less ordered and thinner than the rest.

Consequently, these films are found to self-assemble into a lamellar mesophase with d spacing of ~36 Å due to the 100 reflection (see Table 7.4). Henderson *et al.*[25] reported similar d spacing (35 Å) for a lamellar mesophase of a titania thin film, templated also by SDS. Smaller d spacing of 33.5 Å for a lamellar TiO2 sample, using dodecyl phosphate as surfactant, was earlier reported by Putnam *et al.*, [28]which has been also found for other of our samples (see Table 7.4). Patterns taken at 0.13°, which probe only the first 100 Å at the top of the film shows similar ordering at the film surface compared to that of the bulk film measured at higher incident angles.

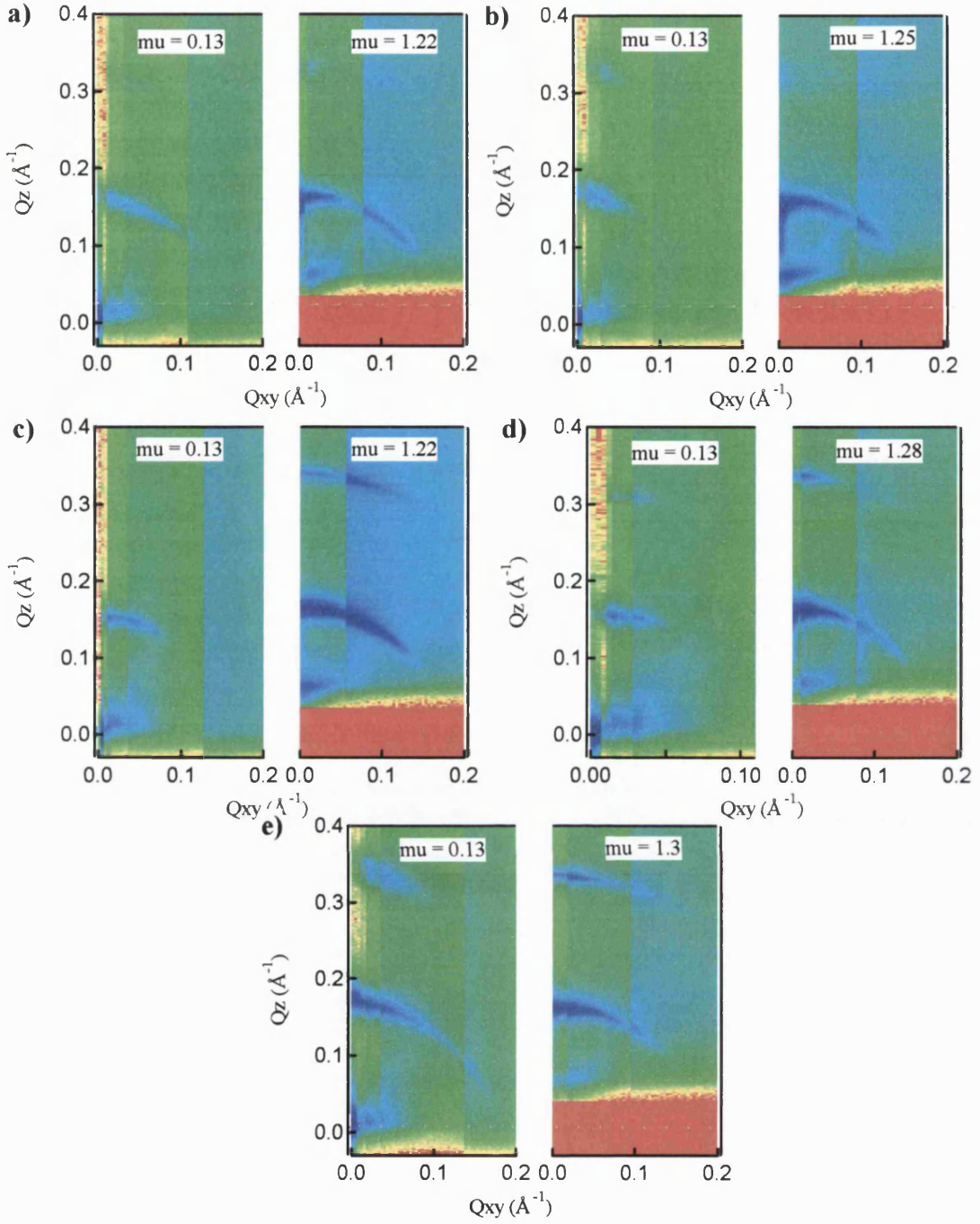

Figure 7.4. Two-dimensional GIXD plots for a) 1/2; b) 3/4; c) 1; d) 5/4; and e) 3/2 × SDS following these solution molar ratios: X SDS: 1.4×10^{-2} HCl: 1 water: 1.7×10^{-3} $Ti(OBu^n)_4$. (see Table 7.1).

7.3.3 SANS Results

A series of SANS experiments were carried out to investigate the formation of mesophase structures in titania-SDS solutions. The polymerisation of titania precursors in aqueous solutions with anionic surfactants (e.g. SDS) occurs faster than that of silica, and therefore time-resolved experiments could not be performed. The study was focused on the precipitate, which remains in solution as a suspended solid. Very weak scattering at very small angles was observed at several D_2O/ H_2O contrasts suggesting no mesophase ordering in the precipitate (see Figure 7.5 and 7.6). It was not possible to fit these patterns with models as done for SiO_2 in previous chapters. However same measurements taken from surfactant solution without the titania precursor produce a strong solution scattering from the micellar solution (see Figure 7.7). Butanol generated from hydrolysis of the $Ti(OBu^n)_4$ may affect the micelles in solution and therefore patterns from solutions with butanol added were measured. However scattering was also achieved in acidic SDS solution with the addition of butanol, indicating that the butanol does not prevent micelle formation. Therefore when $Ti(OBu^n)_4$ is added to the surfactant solution nanoscale ordering occurs only at the surface of the solution while the bulk precipitation contains no ordered structures. However the addition of titania precursor is very effective at removing SDS micelles from solution so the formed particles are likely to be SDS-TiO_2 composites, just not ordered composites. Possibly a surfactant with a longer tail is required to get ordered mesostructured particles forming in the subphase as well as at the interface, since a longer hydrophobic tail will promote mesostructural ordering when the SDS-TiO_2 composite particles form. C_{12} surfactants in general form less well ordered mesostructures than surfactants with longer hydrophobic tails.

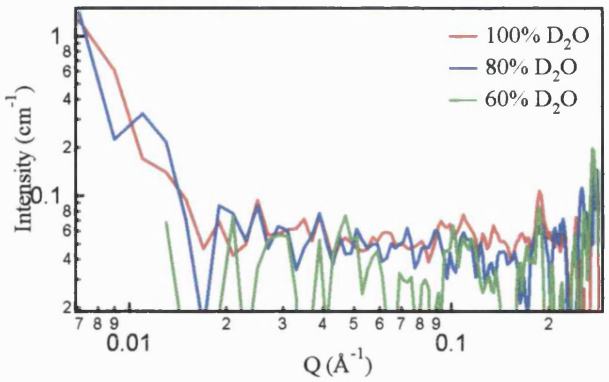

Figure 7.5. SANS patterns from 1/2 x SDS: 1/2 x HCl: 1 x $Ti(OBu^n)_4$ solutions for 100, 80 and 60% D_2O/ H_2O contrasts.

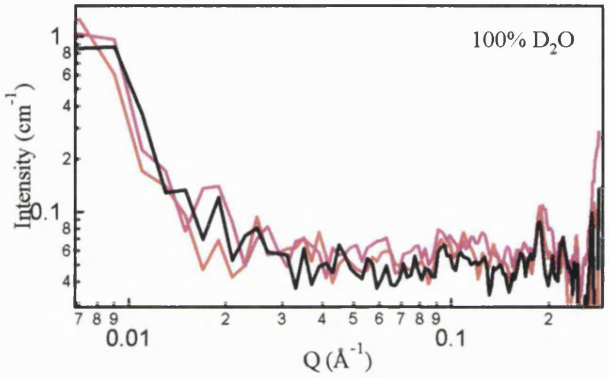

Figure 7.6. SANS patterns from (—) 1/2 x SDS: 1/2 x HCl: 1 x $Ti(OBu^n)_4$; (—) 1 x SDS: 1/2 x HCl: 1 x $Ti(OBu^n)_4$; and (—) 1/2 x SDS: 1/2 x HCl: 1 x $Ti(OBu^n)_4$ solutions for 100 D_2O/ H_2O contrast.

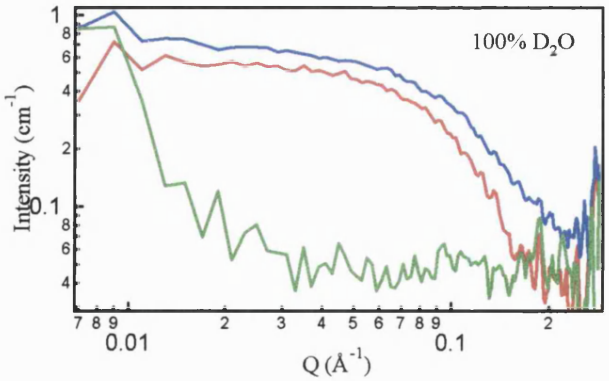

Figure 7.7. SANS patterns1 x SDS: 1 x HCl solutions with no additives (—), butanol (—), and TBOT (—) for 100 D_2O/ H_2O contrast.

7.4 Brij56-Templated Mesoporous Titania Thin Films

7.4.1 Off specular X-ray Reflectivity Results

Similar to the work on silica-non-ionic surfactant films[26, 29] we followed in real time the film formation using titania. This study is focused on the effect of the acid, surfactant, and titania precursor concentration on both the development of the mesostructure with time, and the final film structure.

Figure 7.8 shows off specular X-ray reflectivity waterfall profiles in which mesoporous Brij56® templated titania thin films are followed in real time. Four Brij56® molar ratios were compared for HCl and $Ti(OBu^n)_4$ at normal concentrations.

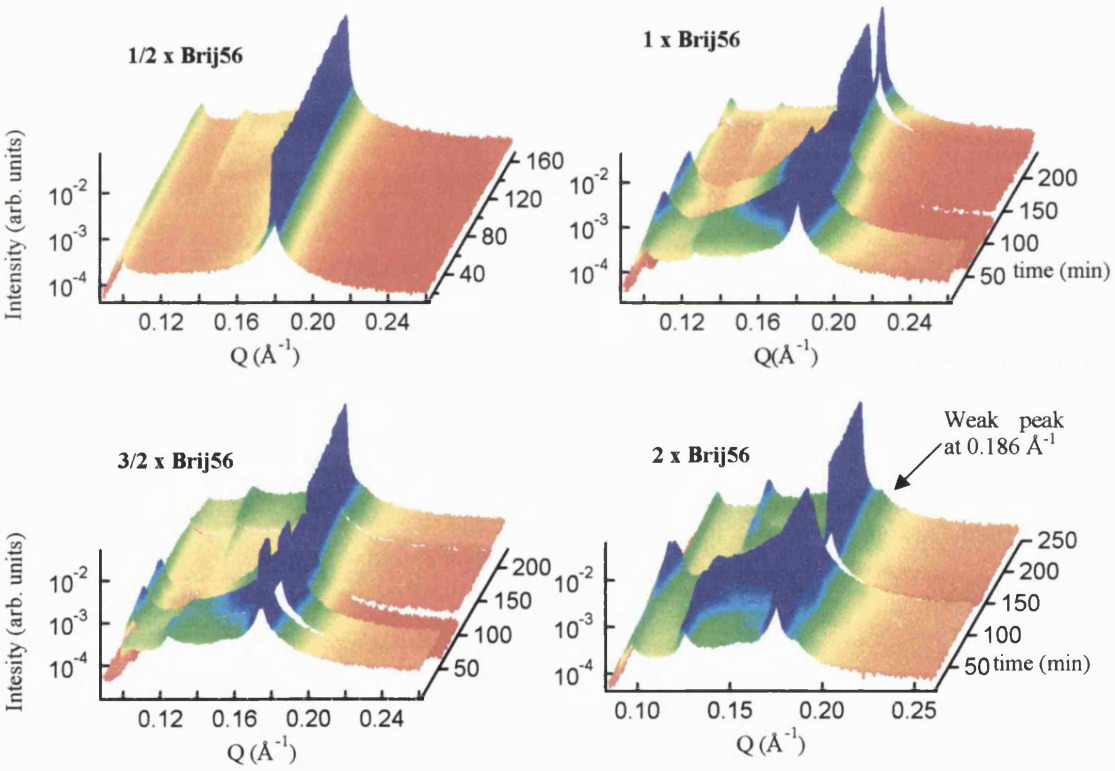

Figure 7.8. Off specular profile[§] against time for ½, 1, 3/2, and 2 times Brij56® normal concentration following the molar ratio of X Brij56®: 2.8 × 10^{-2} HCl: 1 water: 1.7 × 10^{-3} $Ti(OBu^n)_4$.

[§] Variations in beam intensity cause steps in the off specular reflectivity profiles (see Yoneda peak).

An improvement in the mesophase structure is observed as the surfactant concentration increases. It is also noticeable that the formation rate of the film seems to be slower at low Brij56® concentrations. On the other hand is difficult to predict the formation mechanisms of these films since this study relies on the evolution of the first diffraction peak from the moment it appears. The induction period, time from mixing the surfactant-water solution with the titania-acid to when the first diffraction peak grows, is very short. Therefore when the first off specular measurement is collected the diffraction peak is already present and consequently the earliest stages of the self-assembly process cannot be studied.

7.4.2 Specular X-ray Reflectivity results

The lack of a second diffraction peak and the low intensity of the diffraction peak from the off specular reflectivity results agree with the final specular reflectivity patterns shown next.

Figure 7.9 shows how the acid concentration affects the film mesostructure. An improvement in the specular reflectivity pattern is observed, with the presence of very broad peaks or bumps as the HCl concentration increases. The lack of long range order in these films could be due to the polydipersity of the surfactant head group in the commercial Brij56® surfactants which inhibits formation of highly ordered mesophase.

The non-ionic surfactant concentration also affects the structure, in the case of 1 × HCl concentration in Figure 7.10, the lowest Brij56® concentration loses the broad peaks visible at the other concentrations. On the other hand, a lack of any kind of structure in 3/4 × HCl profiles indicates the important role that the acid concentration performs in the formation process of the film probably due to H^+ increases H-bonding interactions between EO groups a TiO_2.

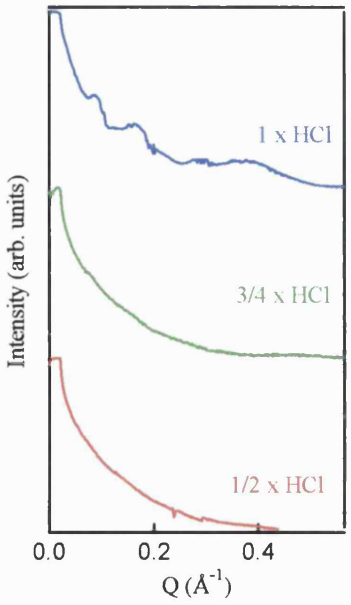

Figure 7.9. Specular reflectivity patterns for different samples varying HCl concentrations in the following solution molar ratios: 2.7×10^{-4}Brij56®: Y HCl: 1 water: 1.7×10^{-3} Ti(OBu^n)$_4$ (Y is defined in Table 7.2).

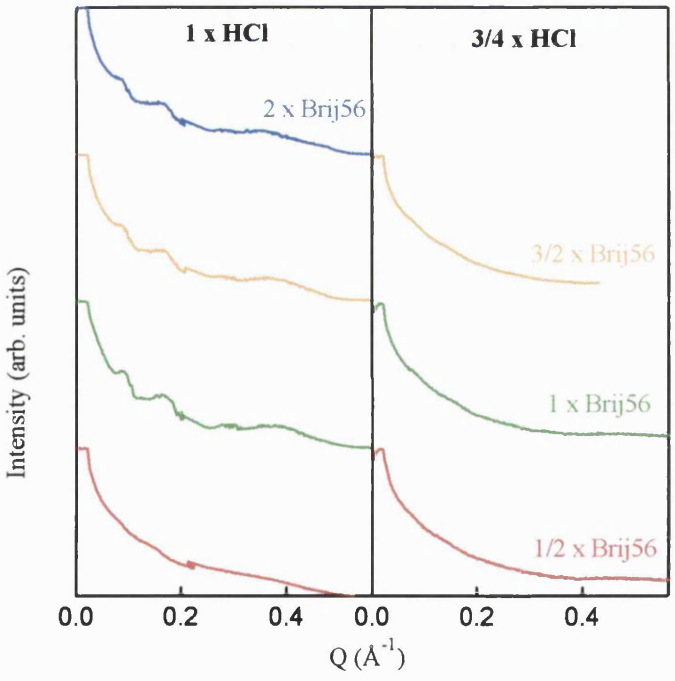

Figure 7.10. Specular reflectivity patterns for two HCl concentrations varying Brij56® surfactant concentrations in the following solution molar ratios: X Brij56®: 2.8×10^{-2} HCl: 1 water: 1.7×10^{-3} Ti(OBu^n)$_4$ and X Brij56®: 2.1×10^{-2} HCl: 1 water: 1.7×10^{-3} Ti(OBu^n)$_4$ (X is defined in Table 7.2)

Table 7.5. Bragg peaks given in Q ($Å^{-1}$) and *d*-spacing (Å) values for four different $Ti(OBu^n)_4$ concentrations for X Brij56®: 2.8×10^{-2} HCl: 1 water: 1.7×10^{-3} $Ti(OBu^n)_4$.

X	Bragg peaks							
	1st		2nd		3rd		4th	
	$Å^{-1}$	Å	$Å^{-1}$	Å	$Å^{-1}$	Å	$Å^{-1}$	Å
1/2	—	—	—	—	—	—	—	—
1	0.087	72.2	0.168	37.4	0.282	22.2	0.387	18.1
3/2	0.087	72.2	0.168	37.4	0.282	22.2	0.387	18.1
2	0.089	70.6	0.166	37.8	—	—	0.361	17.4

The errors for the Bragg peaks correspond with values between ± 1 and 2 Å.

The concentration effect of the titania precursor is also studied in Figure 7.11. The results show that at high and low $Ti(OBu^n)_4$ concentration the film loses the mesostructure. However for intermediates concentration more structure can be seen. The effect of titania concentration does not follow a linear dependence as observed for the effect of altering the acid and the surfactant concentrations.

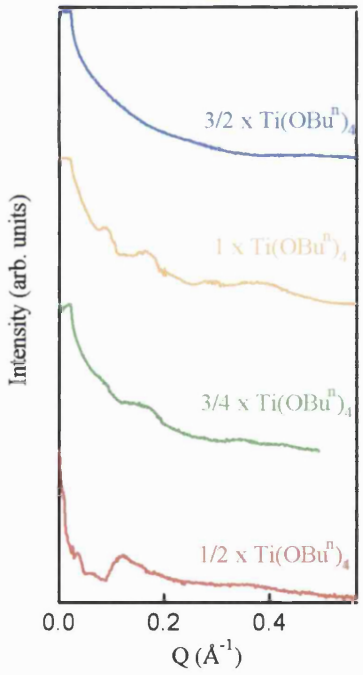

Figure 7.11. Specular reflectivity patterns varying Ti $(OBu^n)_4$ concentrations in the following solution molar ratios: 2.7×10^{-4} Brij56®: 2.8×10^{-2} HCl: 1 water: Z $Ti(OBu^n)_4$ (Z defined in Table 7.2)

Table 7.6. Bragg peaks given in Q ($Å^{-1}$) and *d*-spacing (Å) values for four different $Ti(OBu^n)_4$ concentrations for 2.7×10^{-4} Brij56®: 2.8×10^{-2} HCl: 1 water: Z $Ti(OBu^n)_4$

Z	Bragg peaks							
	1st		2nd		3rd		4th	
	$Å^{-1}$	Å	$Å^{-1}$	Å	$Å^{-1}$	Å	$Å^{-1}$	Å
1/2	0.118	53.2	—	—	—	—	0.378	16.6
3/4	0.087	72.2	0.170	37.0	0.280	22.4	0.348	18.0
1	0.087	72.2	0.168	37.4	0.282	22.2	0.387	18.1
3/2	—	—	—	—	—	—	—	—

The errors for the Bragg peaks correspond with values between ± 1 and 2 Å.

7.4.3 GIXD results

GIXD measurement was also applied to study the mesostructures of the Brij56®-templated titania thin films for five different samples, changing the surfactant concentrations. A first incident angle was set at 0.13°, as in SDS-titania system, and a second higher angle at 0.62 and 0.64° chosen from the positions in degrees of the only diffraction peak obtained from the off-specular reflectivity measurements. Unlike SDS-titania films, the GIXD patterns for the non-ionic titania thin films are characterised by the lack of diffraction rings or Bragg spots suggesting a very poorly ordered mesostructure (see Figure 7.12). This result agrees with the specular and off-specular reflectivity results.

The spot seen in the GIXD at higher angle is due to the reflected beam and also to the intensity associated with the first order diffraction bump. Since we use the angle of the diffraction peak as the angle of the incident beam, the reflection of this beam and the first order peak will occur in the same place.

Most of the more structured Brij56®-titania films shows a lamellar structure with a *d* spacing of ~72 Å, which is twice the *d* spacing of SDS-titania films since the Brij56® carbon chain length is longer and EO head group is larger than the sulphate head group of the SDS.

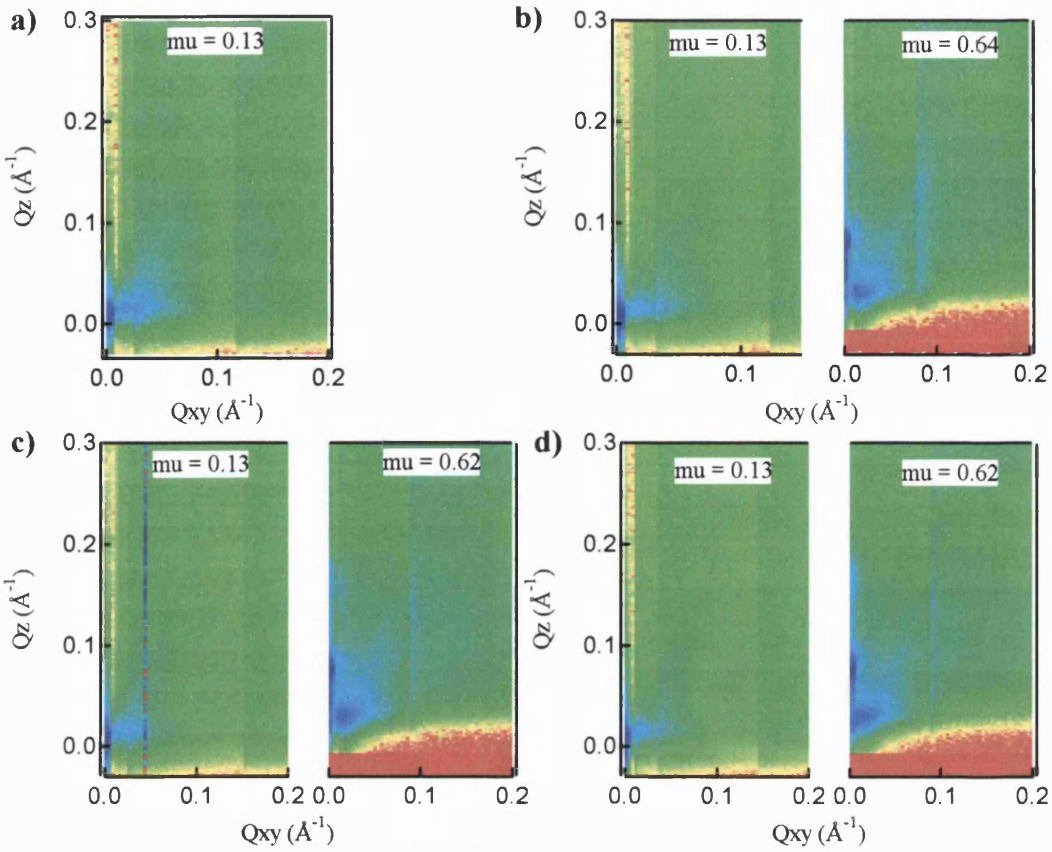

Figure 7.12. Two-dimensional GIXD plots for a) 1/2; b) 1; c) 3/2; and d) 2 × Brij56® following these solution molar ratios: X Brij56®: 2.8 × 10^{-2} HCl: 1 water: 1.7 × 10^{-3} $Ti(OBu^n)_4$ (see Table 7.2).

7.4.4 SANS Results

In the case of titania-Brij56® solutions , like titania-SDS results, micelles form and despite film grows after a short induction period the subphase solution remained clear and no evolution of micelles occurs (see Figure 7.13).

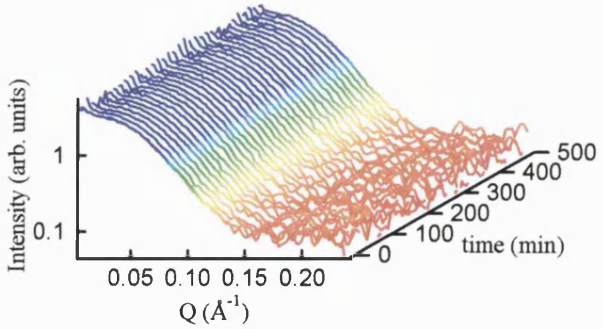

Figure 7.13. Sans profiles against time for 2.7 × 10^{-4} Brij56®: 2.8 × 10^{-2} HCl: 1 water: 1.7 × 10^{-3} $Ti(OBu^n)_4$ molar ratios.

7.5 Discussion

The effect of the acid, surfactant and titania precursor concentration in the formation of surfactant templated titania films have been studied, looking at two systems with two different types of surfactants, anionic (SDS) and non-ionic (Brij56®).

The acid concentration determines the rate of the film growth. Previous studies of mesosporous silica thin films have demonstrated that a low acid concentration (around 0.2 M) increases the formation time of the film making it possible to study the development of the mesostruture with time.[29] In the formation of titania thin films it was not possible to slow growth by reducing the acid concentration. Highly acidic conditions were required to stabilize titanium (IV) and hence to prevent immediate TiO_2 precipitation. The hydrochloric acid is apparently complexed with the titania, slowing down the precipitacion reaction.[22]

Apart from the film formation time the acid concentration also affects the final film structure. Increasing the concentration of HCl for both SDS and Brij56®-titania films caused a better degree of structural organization to be observed. However specular reflectivity measurements have demonstrated that a better ordered film could be achieved using the anionic surfactant than the non-ionic one. Brij56® as a polydisperse surfactant forms different micelle sizes, which makes difficult to pack into ordered structures with the titania species. However the uniform sized SDS micelles promotes the formation of a stable mesophase structure.

It has also been observed that for both systems the surfactant concentration affects the mesostructure, which in general seems to lose structure as the concentration decreases.

The presence of double peaks in the specular reflectivity profiles for SDS-titania films, shown in Figure 7.3, suggests the co-existence of another structure. This could be due to SDS breaking down in acidic conditions to form dodecanol and sulphate.[30] Therefore the dodecanol could form monolayers or crystals giving a second structure with slightly smaller *d* spacing.

The growth of the Brij56® templated titania thin films could be followed by off-specular X-ray reflectivity since it is slower than for the SDS-titania films. The growth slowed down possibly because the Brij56® acted as a coordinating ligand for the titanium tetrabutoxide reducing the reactivity of the metal precursor and likewise slowing down the reaction. Hüsing *et al.*[10, 31] investigated the formation of mixed silica-

titania thin dip coated films synthesized by a ligand-assisted templating (LAT) approach using Brij56® as structure directing agent. NMR results suggested that the poly(ethylene oxide) part of the non-ionic surfactant molecule acts as coordinating ligand for the titanium species (see Figure 7.14). Our SANS results on titania-Brij56® solutions also suggest formation of stable micelle species which do not develop with time, indicating strong coordination between titania species and the EO head group unlike the interaction between silica and EO head group where silica polymerization still occurs.

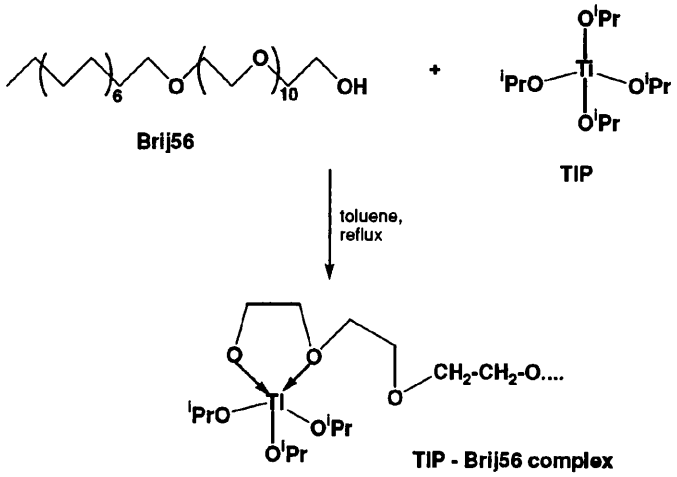

Figure 7.14. Ti-Brij56 (Polyoxiethylene (10) cetylether) complex.[10]

The mesostructure of our titania films was analysed by grazing incidence X-ray diffraction showing a lamellar mesophase in the case of SDS-titania films varying with surfactant concentration. Putnam *et al.*[28] produced surfactant-templated titania powders with lamellar mesostructures using as surfactant dodecyl phosphate, also an anionic surfactant very alike to SDS. The lamellar TiO_2 form was calcined into the related hexagonal phase Ti-TMS1. A later publication reported by Nagamine *et al.*[23] proposed SDS-titania composite in HCl acidic conditions which also formed a lamellar nanostructure. They focused on the effect of the SDS and HCl concentrations on the nanostructure, determining that the ordering of nanostructure improves with increasing concentration.

For Brij56®-titania films the GIXD patterns proved a disordered mesostructure probably due to use of a polydisperse surfactant, as the specular reflectivity techniques have also suggested.

The study of micelles in the subphase of SDS-templated titania film solutions was performed using SANS. The results show a disappearance of micelles in solution

indicating that the precipitate, which is immediatly formed after mixing, is a non-ordered mixture of inorganic and organic species, despite the high degree of order observed in the films. Consequently it is suggested that this self-assembly must occur at the solution surface, probably, by the absorption of alternating layers of titania and surfactant rather than by adding titania coated micelles.

7.6 Conclusion

Two different mesostructured titania thin films have been synthesized using anionic (SDS) and non-ionic (Brij56®) surfactants as structure directing agents. These films grow at the air-liquid interface under acidic condition.

Studies on the formation time and the growth mechanism of these titania thin films could not be achieved due to the short induction period caused by a fast film growth due to the rapid TiO_2 polymerization under the experimental conditions used.

Final film structures have been investigated as a function of the acid and surfactant concentration by specular X-ray reflectivity measurements. Results revealed that the mesostructural order is highly dependent upon the acid concentration for films templated with the anionic surfactant. Furthermore the order of the nanostructure increased with increases in the SDS or Brij56® and HCl concentrations. This is possibly due to the enhanced attraction between the positively charged titania and the anionic polar head of SDS, or the interactions via H-bonding between the titania and the hydrophilic Brij56® groups at high HCl concentrations.

The evolution of the micellar structure in the SDS-titania bulk solution by SANS could not be followed due to the fast precipitation readily formed after mixing solutions. The measurement was performed for the solution with suspended solid observing no indicia of any mesophase ordering. In the Brij56® solutions stable micelles strongly coordinated to titania species were formed. In both cases therefore film formation must be purely interface driven phenomenon.

A lamellar mesophase was found for the SDS-templated titania films as the two-dimensional GIXD patterns shows, which are characterised by the presence of diffraction rings with 100 and 200 reflections. Poor mesostructural order in the Brij56®-templated titania films was determined by specular reflectivity and grazing incident X-ray diffraction measurement results due to the polydispersity of this surfactant.

7.7 References

(1) Grosso, D.; Soler-Illia, G.; Babonneau, F.; Sanchez, C.; Albouy, P. A.; Brunet-Bruneau, A.; Balkenende, A. R. *Advanced Materials* **2001**, *13*, 1085-1090.
(2) Soler-Illia, G.; Louis, A.; Sanchez, C. *Chemistry of Materials* **2002**, *14*, 750-759.
(3) Stathatos, E.; Tsiourvas, D.; Lianos, P. *Colloids and Surfaces a-Physicochemical and Engineering Aspects* **1999**, *149*, 49-56.
(4) Matsumoto, Y.; Ishikawa, Y.; Nishida, M.; Ii, S. *Journal of Physical Chemistry B* **2000**, *104*, 4204-4209.
(5) Hagfeldt, A.; Gratzel, M. *Accounts of Chemical Research* **2000**, *33*, 269-277.
(6) Gao, F. G.; Bard, A. J.; Kispert, L. D. *Journal of Photochemistry and Photobiology a-Chemistry* **2000**, *130*, 49-56.
(7) Vichi, F. M.; Tejedor-Tejedor, M. I.; Anderson, M. A. *Chemistry of Materials* **2000**, *12*, 1762-1770.
(8) Yang, P. D.; Zhao, D. Y.; Margolese, D. I.; Chmelka, B. F.; Stucky, G. D. *Nature* **1998**, *396*, 152-155.
(9) Soler-Illia, G.; Sanchez, C. *New Journal of Chemistry* **2000**, *24*, 493-499.
(10) Husing, N.; Launay, B.; Kickelbick, G.; Hofer, F. *Journal of Sol-Gel Science and Technology* **2003**, *26*, 615-619.
(11) Crepaldi, E. L.; Soler-Illia, G.; Grosso, D.; Cagnol, F.; Ribot, F.; Sanchez, C. *Journal of the American Chemical Society* **2003**, *125*, 9770-9786.
(12) Antonelli, D. M.; Ying, J. Y. *Angewandte Chemie-International Edition in English* **1995**, *34*, 2014-2017.
(13) Froba, M.; Muth, O.; Reller, A. *Solid State Ionics* **1997**, *101*, 249-253.
(14) Khushalani, D.; Ozin, G. A.; Kuperman, A. *Journal of Materials Chemistry* **1999**, *9*, 1491-1500.
(15) On, D. T. *Langmuir* **1999**, *15*, 8561-8564.
(16) Linden, M.; Blanchard, J.; Schacht, S.; Schunk, S. A.; Schuth, F. *Chemistry of Materials* **1999**, *11*, 3002-3008.
(17) Kawai, M.; Miyake, Y. *Kagaku Kogaku Ronbunshu* **2001**, *27*, 724-729.
(18) Yusuf, M. M.; Imai, H.; Hirashima, H. *Journal of Non-Crystalline Solids* **2001**, *285*, 90-95.
(19) Li, X. S.; Fryxell, G. E.; Birnbaum, J. C.; Wang, C. M. *Langmuir* **2004**, *20*, 9095-9102.
(20) Wang, K. X.; Morris, M. A.; Holmes, J. D. *Chemistry of Materials* **2005**, *17*, 1269-1271.
(21) Hwang, Y. K.; Lee, K. C.; Kwon, Y. U. *Chemical Communications* **2001**, 1738-1739.
(22) Alberius, P. C. A.; Frindell, K. L.; Hayward, R. C.; Kramer, E. J.; Stucky, G. D.; Chmelka, B. F. *Chemistry of Materials* **2002**, *14*, 3284-3294.
(23) Nagamine, S.; Sasaoka, E. *Journal of Porous Materials* **2002**, *9*, 167-173.
(24) Henderson, M. J.; King, D.; White, J. W. *Australian Journal of Chemistry* **2003**, *56*, 933-939.
(25) Henderson, M. J.; King, D.; White, J. W. *Langmuir* **2004**, *20*, 2305-2308.
(26) Brennan, T.; Hughes, A. V.; Roser, S. J.; Mann, S.; Edler, K. J. *Langmuir* **2002**, *18*, 9838-9844.
(27) Brennan, T.; Roser, S. J.; Mann, S.; Edler, K. J. *Langmuir* **2003**, *19*, 2639-2642.
(28) Putnam, R. L.; Nakagawa, N.; McGrath, K. M.; Yao, N.; Aksay, I. A.; Gruner, S. M.; Navrotsky, A. *Chemistry of Materials* **1997**, *9*, 2690-2693.

(29) Edler, K. J.; Brennan, T.; Roser, S. J.; Mann, S.; Richardson, R. M. *Microporous and Mesoporous Materials* **2003**, *62*, 165-175.
(30) Penfold, J.; Thomas, R. K.; Simister, E.; Lee, E.; Rennie, A. *Journal of Physics-Condensed Matter* **1990**, *2*, SA411-SA416.
(31) Husing, N.; Launay, B.; Doshi, D.; Kickelbick, G. *Chemistry of Materials* **2002**, *14*, 2429-2432.

Chapter 8 Conclusions

Mesoporous surfactant-templated silica and titania thin films, growing under acidic conditions at the air-liquid interface, have been studied using complementary surface and bulk techniques. Specular and off-specular X-ray reflectivity, grazing incident X-ray diffraction (GIXD), and Brewster angle microscopy (BAM) have been used to obtain information about the film surface features. Small angle neutron scattering (SANS) has been used to characterise the bulk-solution.

Film formation times, growth mechanisms, and final film structures have been studied varying factors such as humidity, temperature, species concentrations, and type of reactants.

Time-resolved measurements have found that a faster silica thin film growth is obtained by decreasing the relative humidity and increasing the temperature allowing evaporation from the surface to occur causing a well-ordered film structure.

In addition changes of silica precursor concentration also affect the film formation time which shows different behaviour depending on the structure-directing agent (or surfactant) used in the synthesis. Film formation time as a function of silica source concentration describes a "horse-shoe" shape in the cationic surfactant-templated silica films. However for non-ionic surfactant-templated silica films a linear dependence is shown in which silica concentration increases results in a faster film growth. In fact, when cationic and non-ionic surfactants are mixed to synthesise silica films, the film formation time appears to be more diverse which depends on the chosen silica precursor and the acid concentration, and the mixed surfactant molar ratios. This is due to different type of attractions between the silica and mixed surfactants as well as between non-ionic and cationic surfactants.

How the polymerised silica interacts with the surfactant micelles and how this process develops along the film formation is explained by the growth mechanisms. Herein two distinguishable mechanism pathways are proposed by studying first peak-width profiles from off-specular reflectivity method. The surface-driven mechanism is described as small domains that grow down into the solution with time whereas the bulk-driven mechanism involves well-ordered aggregates formed in the bulk solution that diffuse to the surface and pack together to from the film. In CTAB-TMOS system an increase in temperature and high and low silica concentrations favours the surface-

driven formation mechanism, while for intermediate concentrations a bulk-driven mechanism takes place. Unlike this charged system the $C_{16}EO_8$-TMOS films present bulk-driven formation for high and intermediate silica concentration and a surface-driven for the lowest one. In the case of mixed surfactant-TMOS system, film formation mechanisms have been studied for three $C_{16}EO_8$/CTAB molar ratios and three TMOS concentrations. The two lowest $C_{16}EO_8$/CTAB molar ratios follow a surface-driven mechanism for the low and intermediate silica concentration and bulk-driven at high silica concentration. However an opposite behaviour has been found for the highest $C_{16}EO_8$/ CTAB molar ratios (0.33/0.66), which seems to follow a bulk-driven formation for the low and intermediate TMOS concentrations. Although the mechanism could not be assigned for 1.5 × TMOS a bulk-driven mechanism could be suggested as described for these concentrations (see schematic below). In general low silica concentrations and highly charged micelles favour the surface driven mechanism while higher silica concentrations and low micelle charge together favour the bulk driven mechanism.

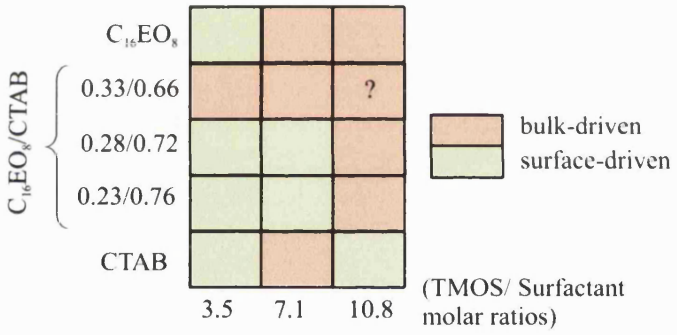

The *in situ* evolution of the micelles in the bulk solution was studied by SANS for $C_{16}EO_8$-TMOS and mixed surfactant-TMOS systems. As a global result a gradual micellar evolution from spherical or ellipsoidal, which elongates with time, to cylindrical was obtained distinguishing three micellar areas: core, shell and solution. The core is formed by the hydrophobic surfactant chain, and the shell is composed by the hydrophilic part of the surfactant and silica, which is surrounded by D2O and/or H2O, ethanol (from silica hydrolysis) and part of the condense silica. In the films however micelle shape evolution must continue to produce the wide range of structures seem in the GIXD patterns.

Well-ordered final film structures were observed by GIXD for the $C_{16}EO_8$-templated silica thin films and $C_{16}EO_8$-CTAB mixed surfactant templated silica films.

Variation on silica concentration causes significant effects on the final film structure upon $C_{16}EO_8$-templated silica thin films, in which the structure changes from 2D hexagonal to cubic as silica concentration increases. In the case of mixed surfactant templated silica films, a change in the structure from centred rectangular to cubic phase occurs as a result of an increase in the $C_{16}EO_8$ concentration.

The last study was focused on the synthesis of anionic (SDS) surfactant-templated and non-ionic (Brij56®) surfactant-templated titania thin films. Since titania presents high reactivity toward hydrolysis producing short induction periods, the study of the film development with time and consequent growth mechanisms could not be achieved. Final film structures have been investigated observing that the mesostructural degree improves with increasing SDS or Brij56® and HCl concentrations, possibly due to the enhanced attraction between titania and hydrophilic surfactant head groups. SDS-templated titania films were found to self-assemble into a lamellar mesophase while Brij56®-templated titania films show a poor lamellar mesostructure.